THESIS
7

MICHIGAN STATE UNIVERSITY LIBRARIES
3 1293 01399 2247

This is to certify that the

thesis entitled
Iron Oxidation Indices for Antarctic Meteorites
with Hypotheses for Associated Weathering Mechanisms

A Study of 19 Weathering Category C Ordinary Chondrites
from Allan Hills and Lewis Cliff
presented by

James Warren Ashley

has been accepted towards fulfillment
of the requirements for

Master of Science degree in Geological Science

Michael Anthony Velbel
Major professor

Date April 4, 1995

O-7639

MSU is an Affirmative Action/Equal Opportunity Institution

LIBRARY
Michigan State
University

PLACE IN RETURN BOX to remove this checkout from your record.
TO AVOID FINES return on or before date due.

DATE DUE	DATE DUE	DATE DUE

MSU is An Affirmative Action/Equal Opportunity Institution
c:\circ\datedue.pm3-p.1

WIT

A STU

IRON OXIDATION INDICES FOR ANTARCTIC METEORITES WITH HYPOTHESES FOR ASSOCIATED WEATHERING MECHANISMS

A STUDY OF 19 WEATHERING CATEGORY C ORDINARY CHONDRITES FROM ALLAN HILLS AND LEWIS CLIFF

by

James Warren Ashley

A THESIS

Submitted to
Michigan State University
in partial fulfillment of the requirements
for the degree of

MASTER OF SCIENCE

Department of Geological Sciences

1995

WIT

A ST

LOI), r

intensit

rock st

mass,

chondr

alterat

of fra

pre-te

the A

reduc

obser

lower

ABSTRACT

IRON OXIDATION INDICES FOR ANTARCTIC METEORITES WITH HYPOTHESES FOR ASSOCIATED WEATHERING MECHANISMS

A STUDY OF 19 WEATHERING CATEGORY C ORDINARY CHONDRITES FROM ALLAN HILLS AND LEWIS CLIFF

By

James Warren Ashley

Preliminary findings show that negative weight loss (weight gain) on ignition (-LOI), may provide a viable alternative to the ABCe system for indexing iron rust intensities among Antarctic meteorites. Further investigation is warranted.

Due to (1) fractures, plus (2) the interplay of secondary product stress versus rock strength, in possible combination with petrologic type and/or recovered sample mass, a heterogeneity in iron oxidation develops in highly weathered Antarctic ordinary chondrites which may also characterize the distribution patterns of other types of alteration products. In addition to weathering intensity, researchers should be mindful of fracture density and recovered sample mass during sample selection for studies of pre-terrestrial properties. H chondrites may be more susceptible to fragmentation in the Antarctic environment than L chondrites due to their higher relative abundance of reduced metal grains. This tendency may help explain the mass frequency distribution observed for the Antarctic ordinary chondrite population, which is skewed toward lower masses for H chondrites relative to L chondrites.

This work is dedicated to my parents:

Leona Rose Ashley

and

Earl Thomas Ashley

in commemoration of their

52nd Wedding Anniversary

(May 15th, 1995)

ACKNOWLEDGMENTS

For their participation in this project, I would like to thank the following individuals and institutions. My advisor and friend Dr. Michael A. Velbel for countless hours of inspiration, brainstorming, support, and good-natured cajoling, Dr. Thomas A. Vogel and Kris Huysken for helping with loss on ignition sample preparation, Dr. Ann Yates for advice on application of the -LOI method for meteorites, Dr. Roy S. Clarke, Jr. and Dr. Eugene Jarosewich of the Smithsonian Institution, Division of Meteorites, for generously allowing me access (on the eve of a national holiday) to the Smithsonian meteorite collection, and the use of their microscope and curatorial facilities, Kurt Zacharias for instruction on use of the scanning electron microscope, Dr. Delbert L. Mokma and Dr. Shawel Haile-Mariam for assistance with the citrate dithionite pre-treatment, Dr. Mounir Saad for assistance with X-ray diffraction procedures, and my friends and colleagues of the Geological Sciences Department at M.S.U. I would like to thank my former employer SSOE, Inc., and work associates Jeff McCormack and David Schroeder for their understanding and composure during my time on this project. I would also like

to expl
provid
weigh
and pr
Peru
and i
aspe

to express my deep gratitude to Dan and Pat Voydanoff for providing my wife and I with a microcomputer system as a wedding gift, as a result of which, this thesis was written and printed at home. Additionally, I wish to recognize Kevin S. Jung, John Foran, Hazel Bremmer, Gary Dannemiller and Dr. Larry Barrows for their assistance with various aspects of the work.

For any first list of acknowledgements, I feel it fitting to include among those directly related to the project, any additional individuals and institutions who are considered instrumental to the author's development as a scientist. Accordingly, I would here like to name Dr. Norman W. Ten Brink for friendly encouragement and guidance during my undergraduate years. Also deserving of his own distinct accolades is Mr. David L. DeBruyn, Chief Curator at the Roger B. Chaffee Planetarium of the Grand Rapids Public Museum where I worked part time for 15 years. I would like to thank Mr. DeBruyn for half a lifetime of patient mentoring and a contagious, and philosophically optimistic enthusiasm for "life, the universe and everything," as it were. I will also mention Mike LeBaron and Jon Truax for having the vision and drive to take on, in the face of political opposition, what came to be known as the James C. Veen Observatory Radio Telescope Project; a six-year, on-going effort carried out in the spirit of research that

ultimately became an accessory to my personal scientific growth.

Most of all, a shining acknowledgment to the object of my affection, my wife Sandy, for superhuman coolness throughout the extended operation of working full time and writing a thesis "on the side," an unfathomable number of home-cooked meals, and an occasional karate kick for motivation.

PREFACE

The weathering of meteorites has been recognized as a stick in the eye of science doubtless since the first find was studied in the laboratory. Cosmically significant interpretations often rely on the precise measurement of subtle patterns in chemical composition and mineralogies. The terrestrial alteration of these primary features is viewed almost as a sacrilegious corruption by many meteoriticists — profaning the stone's innocence like some kind of perverse molestation by disallowing the successful delivery of all those shrouded secrets from our distant past (as the stone had originally intended).

Meteorites are literally windfalls of serendipity — the most exciting rocks on earth fall from the sky. Yet one must be about their swift recovery, or Nature herself will, through weathering, ironically and murderously foil all striving for primordial solar system enlightenment. Its "The Fix," of Mr. Murphy (his zeroth law) — like the bag of gold coins that fades in your hands as you snap out of your dead-of-night influenza fever.

While sharing this sentiment (all humor aside) on a scientific level, I have learned during this research to respect the quiet decay action of the weathering force. There is a noble deliberateness and irreversibility of change for minerals out of equilibrium with their birth-place environment. So it is for all things; and in due time, weathering, or something very like it, will overtake everything and everybody. Like any natural process, weathering (or the increase of entropy) can be thought of simply as an on-going transformation, with effects that can be as beautiful as they are damaging. In the words of Stevenson (1881):

"Right before us, at the southern end we saw the wreck of a ship in the last stages of dilapidation. It had been a great vessel of three masts, but had lain so long exposed to the injuries of the weather, that it was hung about with great webs of dripping seaweed, and on the deck of it shore bushes had taken root, and now flourished thick with flowers."

-Robert Louis Stevenson
Treasure Island

TABLE OF CONTENTS

LIST OF TABLES ____ xi

LIST OF FIGURES ____ xii

KEY TO ABBREVIATIONS AND NOMENCLATURE ____ xvi

1 INTRODUCTION ____ 1

1.1 The Discipline of Meteoritics ____ 1

1.2 Background on Meteorites ____ 2
1.2.1 Chondrite Classification ____ 2
1.2.1.1 Carbonaceous chondrites ____ 5
1.2.1.2 Ordinary Chondrites ____ 6
1.2.1.3 Enstatite Chondrites ____ 7
1.2.2 Petrologic Types ____ 7
1.2.3 Post-accretionary Aqueous Alteration Products ____ 9
1.2.3.1 Carbonaceous Chondrite Matrices ____ 10
1.2.3.2 Ordinary Chondrite Matrices ____ 11
1.2.4 Meteorite Weathering ____ 14
1.2.5 Fusion Crusts and Fractures ____ 15

1.3 Antarctic Meteorites ____ 16
1.3.1 Reconnaissance and Recovery ____ 16
1.3.2 Antarctic Meteorite Weathering ____ 18
1.3.3 Significance of Extraterrestrial Aqueous Alteration for Antarctic Meteorites ____ 21
1.3.4 The Antarctic and non-Antarctic Meteorite Source Controversy ____ 22
1.3.4.1 Age Differences ____ 24
1.3.4.2 Type Differences ____ 25
1.3.4.3 Mass Differences ____ 26
1.3.4.4 Chemical Differences ____ 27
1.3.4.4a Major Elements ____ 27
1.3.4.4b Trace Elements ____ 28

1.4

1.5

2 EX

2.1

2.2

2.3

2.

3 A

3.

3.

3.

3.

4 D

4

4

1.3.4.5 Cause and Implication of Differences 29
1.3.4.5a Terrestrial Causes (Weathering and Contamination) 29
1.3.4.5b Extraterrestrial Causes (Meteoroid Streams) 30

1.4 The Weathering Index 32

1.5 Scope of Experimentation 35

2 EXPERIMENTAL METHODS 37

2.1 Photomicrography 37

2.2 Modal Analysis 37
2.2.1 Difficulties in Modal Analysis 38

2.3 X-ray Diffraction 41
2.3.1 Sample Preparation and General Pretreatment 41
2.3.2 Citrate Dithionite Pretreatment 43

2.4 Negative Loss on Ignition 44

3 ANALYTICAL RESULTS 49

3.1 Petrographic Characterization of Oxides 49
3.1.1 Antarctic Samples 49
3.1.2 Carichic 65

3.2 Modal Analysis 66

3.3 X-ray Diffraction 70

3.4 Negative Loss on Ignition 72

4 DISCUSSION 77

4.1 Graphical Representation of Data 77
4.1.1 Modal Analysis 77
4.1.2 Negative Loss on Ignition 82
4.1.3 Experimental Oxidometer Contrast and Comparison Diagrams 84
4.1.4 Recovered Sample Mass Diagrams 93

4.2 Interpretation of Data 105
4.2.1 Secondary Mineral Identification 105
4.2.1.1 Theoretical Secondary Mineralogy 105
4.2.1.2 X-ray diffraction 107
Carichic 107
ALHA84075,7 108
ALHA77271,27 109
ALHA77182,21 110
4.2.2 Modal Analysis Ternary Diagrams and the OPL-based Index 111
4.2.2.1 Assumptions 111

5 C

AF

AF

C

A

LI

4.2.2.2 ABCe Index Inadequacies 113
4.2.2.3 Residual Metal Grains and Pressure Equilibrium 114
4.2.3 Negative Loss on Ignition and the -LOI Index 122
4.2.4 Experimental Oxidometer Contrast and Comparison 123
4.2.5 Non-index-related Anomalies 125
4.2.5.1 Carichic, Fractures and the FIMAHE 126
4.2.5.2 Associated Weathering Mechanisms 133
A. Sample-specific factors 133
(I) Class and petrologic type weathering 134
(II) Mass-dependent weathering 139
B. Curatorial weathering 141

5 CONCLUSIONS 148

APPENDIX A: PETROGRAPHIC DESCRIPTION OF SAMPLES 151

APPENDIX B: DESCRIPTIVE CATALOGUE OF COLOR TRANSPARENCIES 193

APPENDIX C: X-RAY DIFFRACTION DATA 232

LIST OF REFERENCES 253

Table

2.1

3.1

3.2

3.3a

3.3b

4.1

4.2

4.3

LIST OF TABLES

Table		Page
2.1	Crucible weights before and after cooling	46
3.1	Modal analytical results	67
3.2	Modal opaque mineral percentages	68
3.3a	Negative loss on ignition data for Autumn of 1990	73
3.3b	Negative loss on ignition data for Spring of 1992	74
4.1	Summary of sample-specific information	88
4.2	Calculation of primary and secondary mineral volume percent differences	120
4.3	Determination of delta -LOI means	146

LIST OF FIGURES

Figure		Page
1.1	Barred olivine chondrule	3
1.2	Excentroradial pyroxene chondrule	3
1.3	Granular olivine chondrule	4
1.4	Excentroradial pyroxene chondrule cross section	4
1.5	Sample recovery locations	17
3.1	Iron oxide stain in chondrule	51
3.2	Iron oxide stain in cleavage planes	51
3.3	Iron oxide stain crystallinity; frame #1	52
3.4	Iron oxide stain crystallinity; frame #2	52
3.5	Iron oxide stain crystallinity; frame #3	53
3.6	Opaque-pseudomorphic limonite haloes	53
3.7	Void space partially filled with amorphous oxide and lined by opaque-pseudomorphic limonite	55
3.8	Figure 3.7 view in crossed polarized light	55
3.9	Expanding opaque-pseudomorphic limonite deposit	56
3.10	Figure 3.9 view in crossed polarized light	56

3.11 Expanding opaque-pseudomorphic limonite deposit 57

3.12 Figure 3.11 view in crossed polarized light 57

3.13 Disintegrating opaque grain 59

3.14 Transparent limonite fracture fillings 60

3.15 Figure 3.14 view in crossed polarized light 60

3.16 Botryoidal void space fillings 61

3.17 Sharp contact phase 62

3.18 Figure 3.17 view in crossed polarized light 62

3.19 Sharp contact phase 63

3.20 Figure 3.19 view in crossed polarized light 63

3.21 Carichic 64

3.22 Theoretical opaque metal grain replacement process 70

4.1 Modal analytical data plot in terms of three most basic components 78

4.2 Theoretical distribution of current Antarctic meteorite weathering categories 80

4.3 Redistribution of modal analytical data with non-OPL separated from OPL 81

4.4 Reproducibility of -LOI results 83

4.5 Reproducibility graph with meteorite class and petrologic type indicated 85

4.6 Reproducibility graph with fracture index indicated 86

4.7 Geometrical relationship illustrating false modal value generation for NNL stain 87

4.8 1990 gravimetric and modal index values 90

4.9 1992 gravimetric and modal index values 91

4.10 Plot of both 1990 and 1992 -LOI data 92

4.11 Figure 4.11 showing taxonomic group and petrologic type 94

4.12 Recovered sample mass versus modal index 96

4.13 Recovered sample mass versus gravimetric index 97

4.14 Recovered sample mass versus 1992 gravimetric index 98

4.15 Reproducibility graph illustrating mass distribution 99

4.16 Figure 4.9 with recovered sample mass illustrated 100

4.17 Mass distribution of 1990 -LOI data reillustrated 102

4.18 Difference in -LOI behavior between high and low recovered mass samples 103

4.19 Delta -LOI vectors versus recovered sample mass 104

4.20 Possible scenarios of movement for data points on Figure 4.3 116

4.21 Representation of unweathered ordinary chondrite sample in thin section 128

4.22 Initial stage of weathering 128

4.23 Intermediate stage of weathering 129

4.24 The Carichic sample (advanced stage of weathering) 129

4.25 Example of fracture-induced metal alteration heterogeneity effect 131

4.26 Mass frequency distribution among Antarctic ordinary chondrites 136

4.27 Recovered mass distribution plotted on Figure 4.3 140

KEY TO ABBREVIATIONS AND NOMENCLATURE

ALH	Allan Hills, Antarctica
BFF	Botryoidal fracture fillings
C	Carbonaceous chondrite
CI	Ivuna C group
CM	Murchison C group
CO	Ornans C group
CV	Vigarano C group
CR	Al Rais and Renazzo C group
EOC	Equilibrated ordinary chondrite
FIMAHE	Fracture-induced metal alteration heterogeneity effect
H	High iron ordinary chondrite
L	Low iron ordinary chondrite
LEW	Lewis Cliff, Antarctica
LL	Low total iron, low reduced iron ordinary chondrite
-LOI	Negative loss on ignition
NNL	Neoformed non-pseudomorphic limonite
OI	Oxidation index
OLFF	Opaque limonite fracture and void space fillings
OPL	Opaque-pseudomorphic limonite
PCP	Poorly characterized phase
SCP	Sharp contact phases

SEM	Scanning electron microscope
UOC	Unequilibrated ordinary chondrite
XRD	X-ray diffraction

1 INTRODUCTION

The primary goals of this research are to determine if clay minerals are present in highly weathered Antarctic meteorites, and, more generally, to examine the potential for applicability of an experimental weathering index to the Antarctic meteorite weathering problem.

1.1 The Discipline of Meteoritics

With the exception of Lunar samples recovered by the Luna and Apollo programs, meteorites are the only extraterrestrial rock materials that can be studied in the laboratory. A formidable body of information on some of the earliest inner solar system processes — including nebula condensation and differentiation, planetesimal accretion, and incipient geochemical evolution — is preserved in meteorites. Determined largely through recent studies of oxygen isotope ratios, it is currently accepted that meteorites sample a diverse assemblage of parent bodies, and that their study can therefore lead to a better understanding of a wide variety of geological processes. The most likely parent bodies include as many as 70 or more

of the minor planets (e.g., Dodd, 1986; Lipschutz *et al.* 1989) possibly a small number of comets (e.g., McSween, 1987), the Moon (Lindstrom, 1989), and even the planet Mars (Laul, 1986). Furthermore, because they are preserved remnants of the earliest epochs of nebular solar system history, meteorites may even provide insights into the cosmochemistry of the formation and evolution of other star systems. Meteorites are thus a tangible bridge between the sciences of astronomy and geology, and unite the sub-disciplines of geochemistry and comparative planetology with astrophysics.

1.2 Background on Meteorites

The research reported in this thesis examines the nature of meteorite weathering in the Antarctic environment. Some general background on meteorites is therefore necessary. The following sections constitute a very broad overview at best, and focus on ordinary chondrites for the purpose of preparing the reader for this research.

1.2.1 Chondrite Classification

Meteorites are classified into three main groups; irons, stony-irons and stones, based on iron and silicate fractions. Stones are subdivided into chondrites and



Figure 1.1. Barred olivine chondrule. Photographed in polarized light, this chondrule from ALHA77004,22 displays lamellae of olivine in optical continuity (light brown from iron oxide staining) with dark glassy zones between the lamellae. Frame dimensions are 400 by 600 microns.

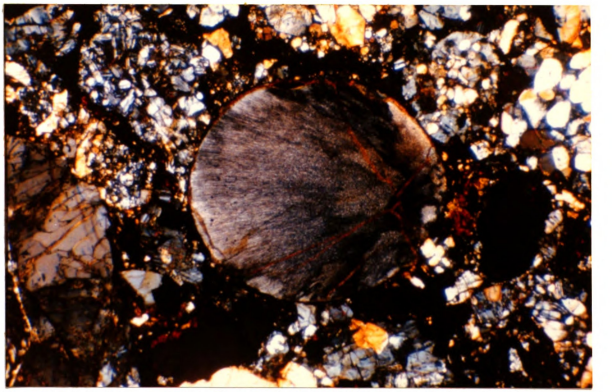
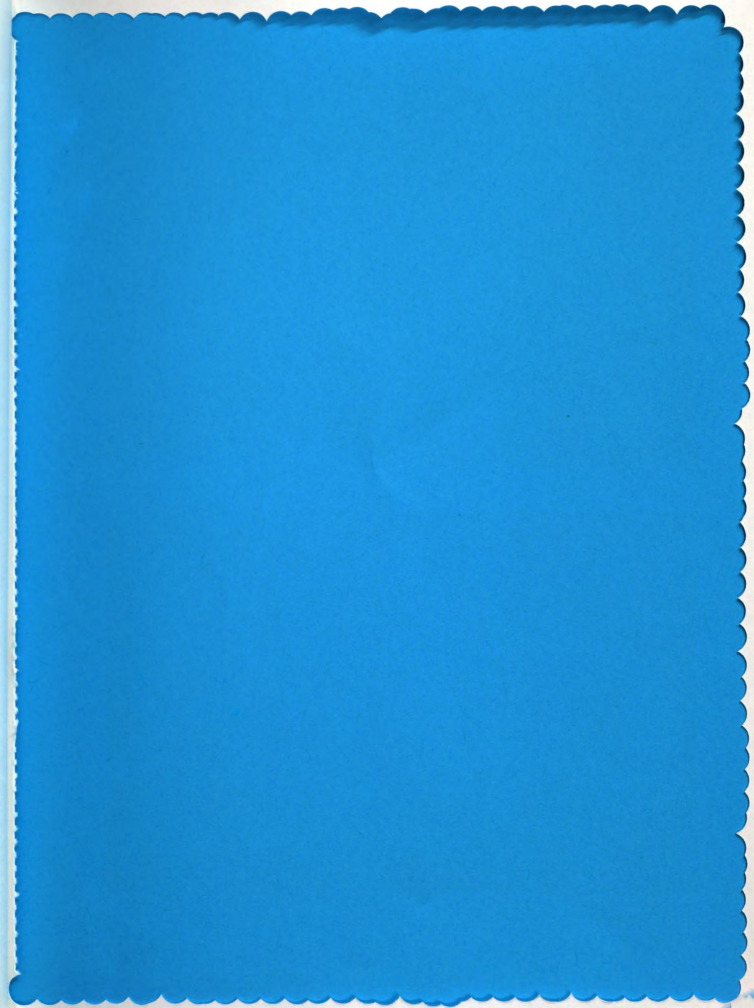
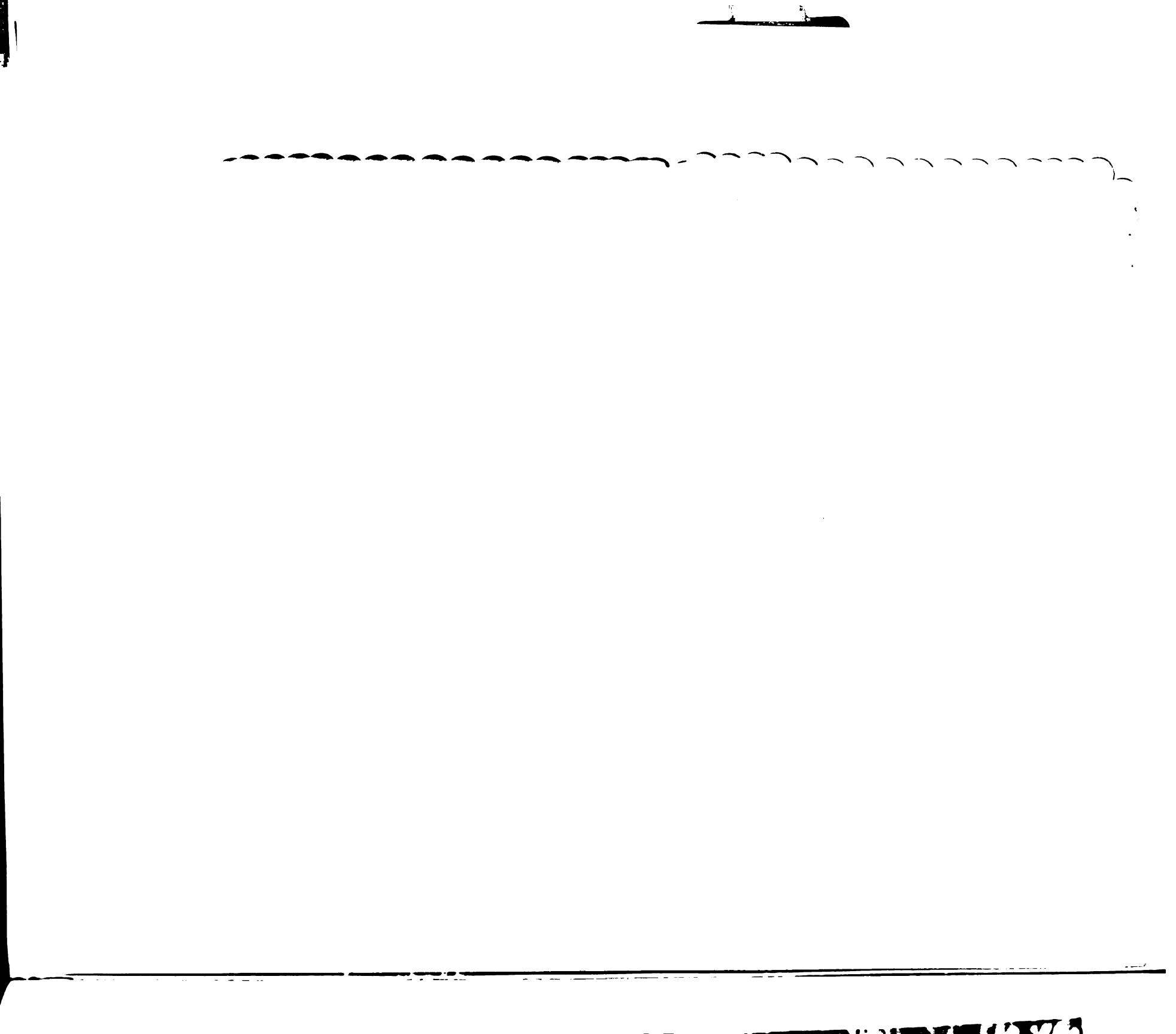


Figure 1.2. Excentroradial pyroxene chondrule. This chondrule in ALHA81031,19 has been formed by the rapid cooling of a droplet of siliceous liquid. Photographed in polarized light, the chondrule is cross-cut by iron oxide stain-filled, shock fractures. Frame dimensions are 1.0 by 1.5 mm.





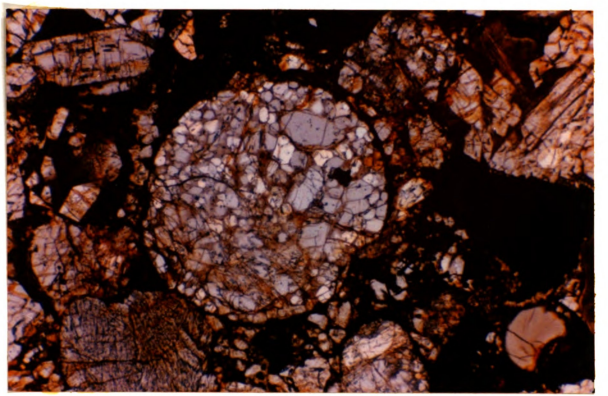


Figure 1.3. Granular olivine chondrule. The granular olivine is one of the clastic accretionary chondrules, as opposed to the barred olivine and excentroradial pyroxene chondrules, which are typically monocrystalline. Photographed in plane transmitted light. The dominant mineral is olivine. This chondrule was identified in ALHA81031, 19. Frame dimensions are 1.0 by 1.5 mm.

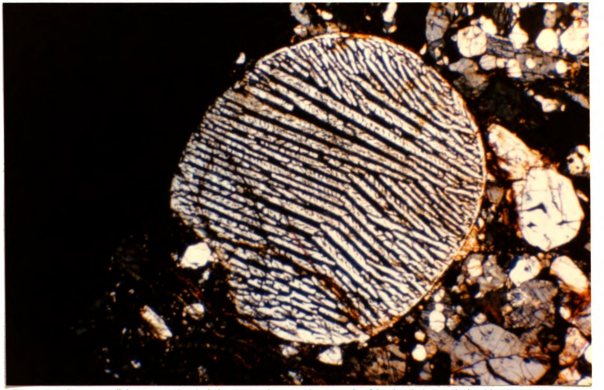


Figure 1.4. Excentroradial pyroxene chondrule in cross section. Another example of the chondrule type depicted in Fig. 1.2., but cut perpendicularly to the plane of crystal growth. Photographed in polarized light. Notice inter-tonguing of pyroxene platelets. Frame dimensions are 1.0 by 1.5 mm.

achondrites, distinguished by the presence in the former of chondrules of various types (millimeter-sized silicate spheroids, Figures 1.1 through 1.4), and other textural and chemical criteria. Chondrites are further subdivided into carbonaceous, ordinary and enstatite categories according to their redox states and refractory lithophile ratios (McSween, 1979). Meteorites are also classified by their mode of recovery. A "fall" is a meteorite whose atmospheric passage was observed and which was recovered shortly thereafter. A "find" is a meteorite that was found at some indeterminate time following its arrival on Earth.

1.2.1.1 Carbonaceous chondrites

Apart from the usual presence of chondrules and sedimentary textures, chondrites are related by their compositions, which are close to that of the solar photosphere, excluding highly volatile elements (Dodd, 1981). Of the chondrites, the carbonaceous (C) chondrites[1] contain nearly perfect solar abundances of major and trace elements and the highest proportions of volatile elements, and so are believed to be the most primitive of this group. As such, they were long thought to represent the starting material from which all subsequent terrestrial planets and their rock types formed and evolved. It is now realized that a great deal of

[1] Carbonaceous chondrites are so named due to their sometimes elevated levels of carbon, though this is not necessarily a diagnostic characteristic (McSween, 1979).

aqueous alteration has taken place within the matrices of C chondrites (see Section 1.3.3), and so at least part of their mineralogies are something less than primary (Dodd, 1981; McSween, 1979).

C chondrites are subdivided into CI, CM, CV, CO and CR classes based on lithophile element ratios. Each class refers to a specific fall and only occasionally have subsequent finds added to the classes. Thus C chondrites are among the least abundant samples in the collections, comprising only some 4.2 percent of all non-Antarctic falls (Sears and Dodd, 1988).

The CIs contain no chondrules and are essentially 100 percent matrix material. CIs and CMs contain the highest abundances of volatile elements and lowest abundances of high temperature minerals of all meteorites.

1.2.1.2 Ordinary Chondrites

Only ordinary chondrites were examined in the present study. Ordinary chondrites comprise some 82 percent of all meteorite samples recovered (Dodd, 1981). The dominant minerals in ordinary chondrites are, in order of decreasing abundance, olivine, pyroxene, plagioclase feldspar, reduced iron-nickel metal (kamacite and taenite), and iron sulfide (troilite); with apatite, chromite, ilmenite, and various

accessory minerals and glass comprising the remaining 1 percent fraction (Dodd, 1981). Texturally, ordinary chondrites are similar to sedimentary rocks, with chondrules, mineral clasts and metal grains set within a matrix of finer material of similar mineralogy. The matrix is a clastic accretion of fine-grained high temperature silicates, and metal and sulfide particles, which together act as a "cement" for the larger grains.

1.2.1.3 Enstatite Chondrites

Enstatite chondrites are the most reduced of the chondrite group of meteorites. Their name is based on their typically high abundance of enstatite (Dodd, 1981). They are mentioned here only for the purposes of completeness. None were examined in the present research. They are relevant to the body of this thesis only in that they have been recovered from Antarctica, and so are in need of proper weathering indexing.

1.2.2 Petrologic Types

Chondrites are assigned a petrologic type number that corresponds to relative intensities of aqueous alteration and thermal metamorphism. Petrologic type numbers range from 1 to 7, and were originally intended to represent a continuous spectrum of metamorphic intensity, measured

according to degrees of textural integration and compositional homogenization for specific mineral phases, from unaffected to highly altered (Van Schmus and Wood, 1967). Petrologic types 1 and 2 (currently known only for carbonaceous chondrites) have been separated from types 3 through 7 for ordinary chondrites (types 3 and 4 also apply to carbonaceous chondrites) because they are now thought to depict stages of hydrothermal processing only and not thermal metamorphism (McSween, 1979). Petrologic types 3 through 7 can be distinguished texturally in thin section.

Metamorphism in meteorites is based on subtle changes in mineral chemistry and texture rather than on empirically derived mineral assemblages, as with terrestrial metamorphic rocks (Best, 1982). Textural and mineralogical characteristics change with increasing metamorphic grade. According to Dodd (1981), olivine compositions vary widely within type 3 chondrites, even within individual chondrules (0 to ≈30 mol% Fa). However, olivines in types 4 through 7 are homogeneous and consistently calcium-poor. Pyroxenes are also inhomogeneous in type 3 chondrites, but this variation persists to type 4 due to the diffusion rates of iron and magnesium. Chemical variations decrease with increasing metamorphic intensity. Hence type 3 chondrites are referred to as unequilibrated ordinary chondrites (UOCs), and those of higher, more chemically homogeneous petrologic types, as equilibrated ordinary chondrites

(EOCs). Also, Fe/Mg ratios increase with petrologic type. Petrologic type 7 is identified based on the presence of calcic orthopyroxene (≥ 1.0% CaO). Quartzofeldspathic glass changes to plagioclase in types 4 through 7. Shock loading can then restructure the plagioclase to form maskelynite. Homogenization occurs through small-scale diffusion processes between the grains and the matrix, which tends to preserve "relict" textures. The primary (pre-accretionary and accretionary), secondary (post-accretionary aqueous and thermal), and tertiary (shock), processes are believed to overlap in space and time.

1.2.3 Post-accretionary Aqueous Alteration Products

As stated above, petrologic types 1 and 2, which belong exclusively to the carbonaceous chondrite group, are no longer considered part of the thermal and shock metamorphic range. Rather, they are thought to be representative of a range in aqueous alteration processing alone, based on variations in secondary mineralogy of the matrix of carbonaceous chondrites (McSween, 1979). These and other pre-terrestrial alteration products (Hutchinson *et al.* 1987) are considered to form under low-temperature hydrothermal conditions. The following is a brief introduction to the aqueous alteration of high temperature meteoritic materials in the extraterrestrial environment.

1.2.3.1 Carbonaceous Chondrite Matrices

It has been known since 1864 that the CI and CM carbonaceous chondrite matrices are composed partly of low temperature phyllosilicate materials (Barber, 1985). This matrix is very fine-grained and consists of magnetite, iron sulfides, gypsum, epsomite, carbonates (dolomite in CIs, calcite and aragonite in CMs), serpentine, chlorite, montmorillonite, and glass fragments (Barber, 1985); with serpentine comprising the dominant matrix phase in CM meteorites (Zolensky and McSween, 1988). Montmorillonites have also been detected in the less primitive CV carbonaceous chondrites and are suspected to exist in the CO carbonaceous chondrites (Tomeoka and Buseck, 1982). CM meteorites are also noted for possessing a poorly characterized greenish and hydrated poorly crystalline silicate known affectionately as "spinach" (Fuchs *et al.* 1973). This material does not lend itself well to examination by conventional methods because of its fine grain size and opacity, the superimposition of X-ray diffraction lines, and the weak intensity of non-basal reflections (Barber, 1985). The material is inferred to be a phyllosilicate and is found in association with olivine grains, which led Olsen and Grossman in 1978 to suggest the spinach to be an alteration product of anhydrous silicates and glass. Two components, one of iron-rich phyllosilicates and a second rich in iron, nickel, sulfur and carbon, comprise this spinach. Gooding

(1985) determined that iron-rich chlorite is the likely phyllosilicate mineral.

Transmission electron microscopy patterns reveal radiating, fern-like fibrous morphologies of the magnesium-rich serpentines in the CI and CM chondrites, as well as disk-shaped growths with circular and spiral patterns of chrysotile (Barber, 1981). Higher resolution images reveal interlayered serpentine and brucite with tubular and sheet-like morphologies (Fuchs *et al.* 1973).

These hydrous phases in the CI and CM carbonaceous chondrites (termed poorly characterized phases, or PCPs by Fuchs *et al.* 1973) are thought to have formed *in situ* by the aqueous alteration of fine-grained high temperature phases and in direct contact with liquid water of uncertain origin (Barber, 1985; Mackinnon and Zolensky, 1984). CM chondrites are similar in texture to hydrothermally altered terrestrial mafic rocks and volcanoclastics, and indicate post-accretionary alteration (e.g., McSween, 1979).

1.2.3.2 Ordinary Chondrite Matrices

Recall that ordinary chondrites differ from carbonaceous chondrites by their lower oxidation states, higher relative abundances of total iron, greater abundances of chondrules, depletion of volatile elements, and lack of low temperature

phases. Recent work by Hutchison *et al.* (1987), and Alexander *et al.* (1989) on the Semarkona and Bishunpur ordinary chondrites (both LL3 UOCs) has revealed phyllosilicate phases in their matrices. Extensive replacement of interchondrule matrix and chondrule rims by iron-rich nontronitic sodium-smectite occurs in Semarkona. This smectite is very fine-grained but occurs locally as a coarse-grained phase with radial growth patterns. As a result of this alteration, very few of the original primary matrix features remain, with the exception of a few inclusions (Barber, 1981), and only the most magnesium-rich mafic minerals are preserved. The Bishunpur ordinary chondrite was found to contain the calcium-smectite saponite, formed from the alteration of amorphous material of feldspathic composition (Hutchison *et al.* 1987). Again, this alteration was confined to the interchondrule matrix. In addition, dissolution features were detected in matrix silicates (olivine and pyroxene), and in association with "maghemite and other poorly described Fe-oxide phases," (Zolensky and McSween, 1988).

Although the equilibrium composition of the volatiles present during these alterations was determined to be dominated by water, it was emphasized by Hutchison *et al.*, (1987) that liquid water need not have been present at the time because grain-boundary fluids could have been sufficient to mobilize elements. These findings moved the

authors to suggest that, due to comparable high temperature mineralogies between carbonaceous and ordinary chondrites, the low temperature phases found in abundance in the carbonaceous chondrites might represent an assemblage toward which ordinary chondrites would evolve given appropriate alteration conditions for an extended time period. Interestingly, the smectite chemistries in both meteorites are similar and uniform throughout the specimens, but have no known terrestrial analogues apart from a similarity to nontronite.

These studies indicate that incipient alteration in unequilibrated ordinary chondrites takes place almost exclusively within the interchondrule matrix and on chondrule rims. Huss *et al.* (1980) examined ordinary chondrite matrices and found there to be two types, (1) a fine-grained, porous, clastic matrix of angular fragments of silica minerals and amorphous interstitial material, and (2) a coarser, less porous, non-clastic matrix. Matrix type 2 was interpreted by the authors to be the recrystallized complement of matrix type 1.

The matrix materials most susceptible to hydrous alteration under terrestrial conditions are the amorphous, glassy phases whose free energies of formation are much less than the well crystallized phases. Tazaki *et al.* (1989) studied incipient clay formation on volcanic, alkalic igneous and synthetic glasses and showed through high resolution

transmission electron microscopic analysis that glass phases contain well-ordered crystalline domains which can trigger clay mineral growth.

Additional examples of extraterrestrial aqueous alteration include the occurrence of iddingsite in nakhlites (Gooding, 1989), one of the associated SNC group of achondrite meteorites suspected to have originated on the planet Mars (Reid and Bunch, 1975); and recent evidence of clay-like minerals on interplanetary dust particles (e.g. Barber, 1985).

1.2.4 Meteorite Weathering

Unfortunately for cosmochemists, meteorites — being dominantly composed of high temperature minerals — weather rapidly in the terrestrial environment where pressure-temperature-concentration (*PTX*) conditions are far from the conditions of formation, and where liquid water and oxygen are abundant[2]. However, while constituting a nuisance to the study of meteorites on Earth, low temperature mineral/water interactions may be a significant extraterrestrial process. It has been suggested that meteoritic weathering scenarios in Antarctica (discussed below) may be analogous to low temperature "hydrocryogenic"

---

[2]Buchwald and Clarke (1989) stated that the "Corrosive processes begin as a meteorite enters the atmosphere and continue until nothing remains that is recognizable."

alteration mechanisms on Mars, asteroid regoliths and interiors, within comets, and within the surfaces of icy moons of the Jovian planetary systems (Gooding, 1986a; Zolensky and McSween, 1988).

1.2.5 Fusion Crusts and Fractures

Fractures in meteorites are present largely due to shock (Dodd, 1981) and provide avenues for the movement of thin films of liquid water, which facilitate the mobilization of chemical constituents (Gooding, 1986b). Due to frictional heating during entry into the Earth's atmosphere, meteorites develop a glassy fusion crust a millimeter or so thick on their exterior surfaces. A fractured fusion crust is far more permeable to air and liquid water than one which remains intact after the fall. It follows that a meteorite with a highly fractured fusion crust will also be more susceptible to weathering than one with a crust still intact. The presence or absence of fractures in a fusion crust may therefore become helpful in determining whether a given alteration product within a specimen is terrestrial or pre-terrestrial in origin (Gooding, 1986a). Secondary products within the interior of meteorites may be pre-terrestrial, whereas alteration products that crosscut or are superimposed upon fusion crusts are terrestrial in origin.

1.3 Antarctic Meteorites

1.3.1 Reconnaissance and Recovery

Since 1969, over 12,000 meteorites have been collected from blue ice sheets in Antarctica by Japanese and American expeditions funded by the National Institute of Polar Research and the National Science Foundation, Division of Polar Programs, respectively (Koeberl and Cassidy, 1991). Meteorites are concentrated at stranding surfaces in ablation zones where ice sheet movement has a substantial vertical component (Delisle and Sievers, 1989; Lipschutz and Cassidy, 1986). The horizontal motion of the ice sheet is usually arrested in these areas by the presence of a mountain range or line of nunataks.

Upon discovery, Antarctic meteorites are photographed and assigned a number according to their location of recovery, field season, year found, and number collected; i.e., ALHA85002, where ALH stands for Allan Hills in this example, A indicates the first field season, '85 is the year, and 002 indicates the meteorite to be the second found during the collecting season at this site. The nineteen Antarctic meteorites used in this project were recovered from either the Allan Hills or Lewis Cliff (LEW) recovery sites (see Figure 1.5).

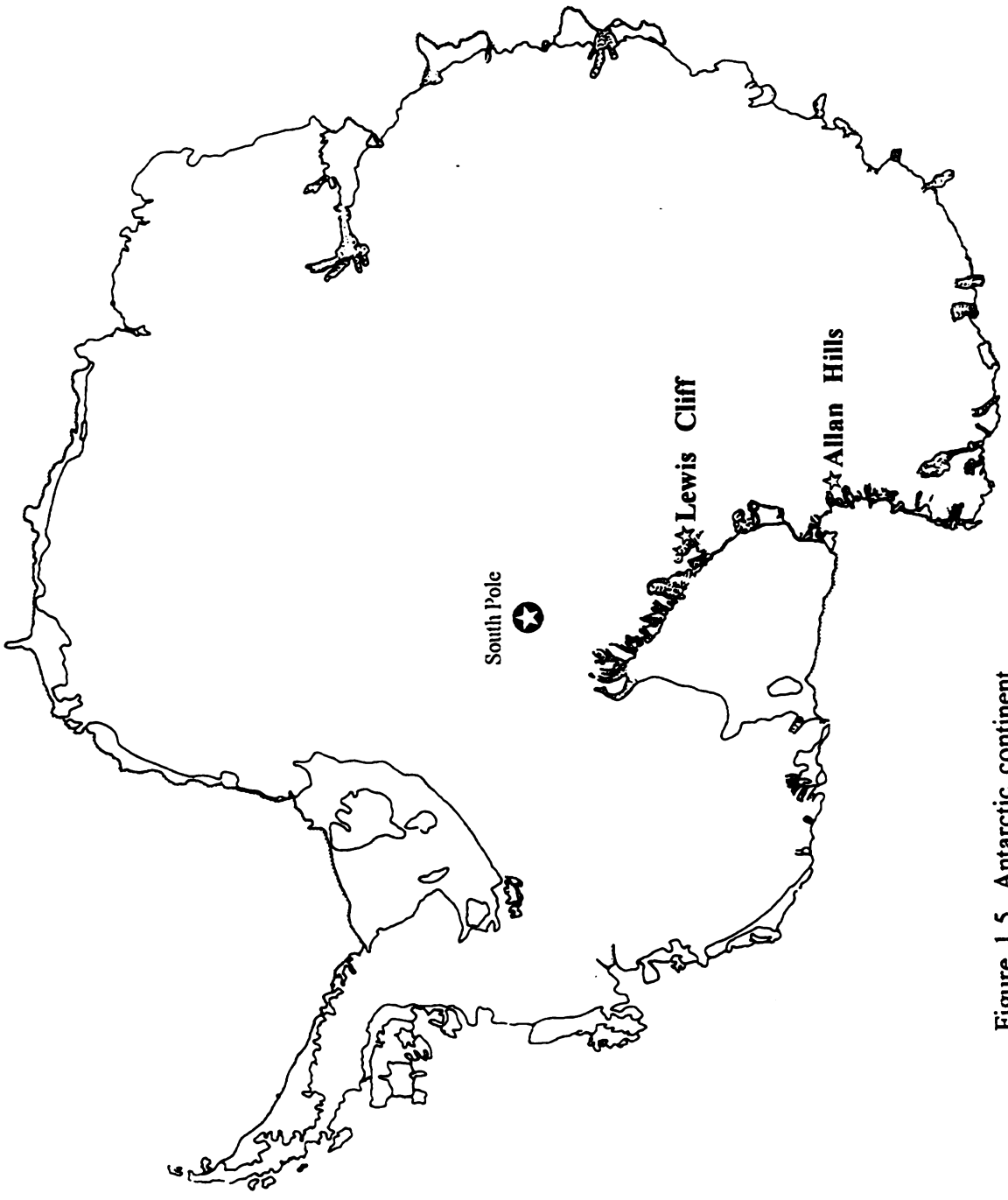


Figure 1.5. Antarctic continent
☆ Sample recovery location

Maximum terrestrial age estimates for Antarctic meteorites range from tens of thousands to one million years (Nishiizumi, 1986; Nishiizumi *et al.*, 1989). As a consequence of so long an exposure to Earth conditions, all Antarctic finds can be presumed to have weathered to some extent. Stony meteorites in temperate climates weather rapidly in as little as two hundred years, with a typical half-life approaching 3600 years (Boeckl, 1972), while those in Antarctica persist much longer due to the low prevailing temperatures. Air temperatures range from -70°C to +20°C annually for the Allan Hills area (Campbell and Claridge, 1987), where most of the study samples were recovered.

1.3.2 Antarctic Meteorite Weathering

Each Antarctic meteorite specimen has clearly undergone chemical weathering to varying degrees as evidenced by iron oxide staining visible in hand specimen (Gooding, 1981). Chemical alterations are a concern to any cosmochemical analysis of Antarctic samples because terrestrial weathering reactions are capable of mobilizing and redistributing major and trace elements in significant amounts. Examples of such elemental redistribution were illustrated in 1988 by Velbel, where it was determined that rubidium, cobalt, iodine, and calcium may be removed from the interiors of Antarctic chondrites to be concentrated at their surfaces during the production of various evaporite minerals, thereafter to be

removed completely by wind erosion. The same was found to be true for carbon (Hartmetz et al., 1989). Depending on the study, the chemical analysis of a weathered meteorite could therefore lead to uncertainties in pre-terrestrial history interpretations.

The most obvious indication of Antarctic meteorite weathering is the presence of iron oxide staining (Gooding, 1981). Preliminary classification of weathering intensities is currently made by the Antarctic Meteoritic Curatorial staff, who assign categories to each specimen recovered on the basis of the degree of rustiness observed in hand specimen (Marvin and Macpherson, 1992), and on the presence or absence of evaporite mineral efflorescences (Velbel, 1988). Category labels range from A (least weathered), through A/B, B, and B/C, to C (most weathered), with a lower case "e" indicating the presence of evaporite efflorescences. This is referred to as the ABCe system, and is defined in the Antarctic Meteorite Newsletter (AMN) and the Smithsonian Contributions to the Earth Sciences (SCES) publications as follows:

> A = minor; metal flakes have inconspicuous rust haloes, oxide stain along cracks is minor.
> B = moderate; metal flecks show large rust haloes, internal cracks show extensive oxide stain.

C = severe; specimen is uniformly stained brown, no metal survives.
e = evaporite deposits visible to the naked eye.

Antarctic meteorite finds are also assigned a fracturing index to aid in the pairing of stones that may have been separated from the original mass. Highly fractured stones are more likely to be fragments of an initial larger mass than stones of high competence. This fracturing index is defined in the AMN and SCES publications as follows:

A = slight; specimen has few or no cracks and none penetrate the entire specimen.
B = moderate; several cracks extend across the specimen, which can be readily broken along the fractures.
C = severe; specimen has many extensive cracks and readily crumbles.

Despite the importance to meteorite research, very little work has focused on the terrestrial weathering of Antarctic meteorites, and the processes remain to be identified and quantified (Gooding, 1989). The recognized secondary products in Antarctic meteorites include hydrous and anhydrous iron oxides (Gooding, 1981), carbonates and sulfates (Marvin, 1980; Jull *et al.*, 1988 and Velbel, 1988), and amorphous mineraloids with smectitic compositions

(Gooding, 1986a,b, 1989). Gooding (1986a) recognized that thin films of liquid water can exist at subzero temperatures that facilitate the elemental migration necessary for typical weathering reactions. In addition, it was empirically determined that Antarctic meteorites exposed to sunlight may have internal temperatures (at depths up to 2.0 cm in some meteorites) that rise as high as 5°C on wind-free days (even when air temperatures remain below 0°C), enabling capillary waters to promote reactions (Schultz, 1986b). Moreover, some oxidation reactions have been found to occur in the solid state at low relative humidities (Buchwald and Clarke, 1989) (see Section 4.2.1.1).

1.3.3 Significance of Extraterrestrial Aqueous Alteration for Antarctic Meteorites

Because of the low prevailing temperatures in Antarctica, meteorite weathering is not expected to have progressed to the degree of aqueous alteration found among the CI and CM carbonaceous chondrites. However, the discovery made in 1986 by Gooding of amorphous clay mineraloids in moderately weathered ordinary chondrites suggests that well crystallized phyllosilicates may yet exist in the most extensively weathered Antarctic samples. If so, they imply by analogy that the alteration processes which occurred in Semarkona and Bishunpur may have taken place at subzero temperatures. The work of Alexander *et al.* (1989) indicates

smectite formation temperatures in these meteorites of less than 260°C, while Barber (1985) cites recent results that suggest alterations of the CI and CM carbonaceous chondrites occurred at temperatures as low as 0°C.

Popular thinking regards CI and CM meteorite low temperature phases as having formed under hydrothermal metamorphic conditions (McSween, 1979). Therefore, if hydrous phyllosilicate minerals of the types found pre-terrestrially in Semarkona, Bishunpur and CI and CM carbonaceous chondrites can also be found as alteration products in weathered Antarctic meteorites, the discovery could have important implications for parent body formation and thermal evolution models.

1.3.4 The Antarctic and non-Antarctic Meteorite Source Controversy

The observation that meteorites found within Antarctic ice sheets differ in many ways from those found elsewhere has been examined extensively in recent years and is used by some to suggest the two populations (Antarctic and non-Antarctic) have different extraterrestrial sources (Dennison, 1986). The variables include terrestrial age, mass, oxygen, mercury and carbon isotopic compositions, type frequency distributions, chemical differences, and petrologic differences (among carbonaceous chondrites; none have been found in ordinary chondrites; e.g., Koeberl and

Cassidy, 1991). Petrographic differences were also observed by Takeda (1991) between Antarctic and non-Antarctic eucrites (one of the achondrites). Opponents to this idea feel the differences can be attributed entirely to terrestrial effects (weathering within or upon the ice sheets). Others feel a combination of terrestrial and extraterrestrial effects account for the observed differences, (e.g., Begemann, 1989). All agree, however, that the differences themselves are real.

The statistical problem of assessing exactly how many individual falls are represented in the Antarctic population is to be found in any discussion of this controversy. The amount of fragmentation or its opposite "pairing" among Antarctic stones directly relates to the level of significance to be placed on any given difference. Of the 12,000 meteorites collected in Antarctica, an estimated 2000 to 4000 distinct falls are represented (Scott, 1984)[3].

The following is a discussion on the nature and importance of these differences.

---

[3] By contrast, the number of non-Antarctic meteorite falls is in the neighborhood of 2500. (e.g., Koeberl and Cassidy, 1991).

1.3.4.1 Age Differences

As stated in Section 1.3.1, Antarctic meteorites are, on average, much older than meteorites found elsewhere on Earth. Terrestrial age dates based on cosmogenic radionuclides are found to range up to 1 million years (Nishiizumi *et al.* 1989), with the majority having terrestrial ages of less than 0.5 million years (e.g., Koeberl and Cassidy, 1991). Terrestrial ages also range noticeably from place to place within the Antarctic environment. For example, meteorites from Allan Hills are typically older than those of the Yamato Mountains. It must be noted, however, that terrestrial age measurements are difficult to obtain and yield values with various margins of uncertainty, depending on the method employed.

By contrast to the Antarctic situation, the half-life of a stony meteorite in more moderate climatic regions of Earth is estimated at 3600 years (Boeckl, 1972). This is a direct result of greater temperatures and greater availability of liquid water. If the Antarctic and non-Antarctic samples of the source regions represent two well-separated time intervals, and the samples differ significantly, it follows the source regions differ significantly. This age difference is therefore elementary to the argument that source regions within the asteroid belt change with time.

Unfortunately, high residence times in any natural terrestrial environment increase the chances for undesirable weathering effects (Gooding, 1986). The importance of establishing the character and measure of each type of terrestrial alteration in each type of Antarctic meteorite thus arises again.

1.3.4.2 Type Differences

Crucial to the problem of pairing is the occurrence among the Antarctic population of uncommon or previously undiscovered meteorites. The apparent meteorite-type frequencies can become severely modified by the fragmentation of a single stone if the total count for its group numbers in the dozens or less (as is the case for many meteorite groups). Such Antarctic finds include previously unencountered varieties of ureilites (shock, or hypervelocity impact-melted slag meteorites), Shergottites (SNC or Martian meteorites), lunar meteorites (never encountered outside Antarctica), rare iron meteorites, and unusual chondrites. On the other hand, the greater proportion of these meteorites may simply be due to the larger total number of Antarctic meteorites.

1.3.4.3 Mass Differences

It has been noticed, nearly since the inception of the Antarctic meteorite recovery program, that Antarctic meteorites are, on average, smaller than non-Antarctic meteorites. The total mass of the non-Antarctic population (falls and finds) is "orders of magnitude larger" than that of the Antarctic population (Koeberl and Cassidy, 1991). This can be explained in part by the bias built into the method of recovery. Nearly every dark-colored rock found on the blue ice sheet will be a meteorite by default, since no mechanism exits to transport terrestrial rocks to these locations. The high color contrast between rock and ice allows much smaller specimens to be found than could be found in non-Arctic and non-Antarctic terrains. Meteorites weighing less than 10 grams are believed to be removed from the ice surface by the strong Antarctic winds (Harvey and Cassidy, 1986).

The preponderance of small meteorites may simply be due to breakage while decelerating upon entry in the atmosphere. This is a common phenomenon, resulting in what has come to be known as a shower fall (e.g., Hutchison, 1983). Such shower falls typically produce strewn fields with thousands of individual stones. A lack of proper pairing to reconstitute the original mass would produce the effect of greater type frequency for a given shower fall type.

An oddly high H/L ratio is observed among the masses of Allan Hills Main ice field ordinary chondrites at a >99 percent confidence level (Huss, 1991). Huss suggests an H5 shower fall took place to explain the nearly five times H5/L ratio in the Allan Hills Main and Near Western ice fields. Dennison *et al.* (1986) observed an H/L ratio three times the value for non-Antarctic falls as for Antarctic finds. This thesis will present the hypothesis of preferential H chondrite fragmentation while within or on the ice sheet as another possible explanation for the observed difference (see Section 4.2.5.2,A,I).

1.3.4.4 Chemical Differences

1.3.4.4a Major Elements

Only one study on major rock-forming elements has been conducted specifically to address the Antarctic/non-Antarctic controversy. Jarosewich (1990) found that non-Antarctic finds are lower in iron, sodium, and sulfur, and higher in water than Antarctic meteorites. He concluded this was due to weathering, since non-Antarctic falls had values somewhat intermediate between the other two populations. He also found the abundance of iron oxide to be highest in Antarctic meteorites.

1.3.4.4b Trace Elements

Volatile and mobile trace elements in ordinary and carbonaceous chondrites, and some achondrites, vary somewhat between Antarctic and non-Antarctic meteorites. The controversy was, in fact, initiated by the identification of statistically significant differences for Antarctic and non-Antarctic H5 chondrites (Dennison *et al.* (1986) and Lipshutz (1986). Specifically, these elements include indium, antimony, selenium, zinc, rubidium, bismuth, thallium, and cadmium in H5 chondrites, with similar differences for H4 and H6 chondrites. Antarctic eucrites were found to have higher abundances of gold, bismuth, cadmium, indium, rubidium, selenium, thallium, and uranium than non-Antarctic eucrites (Paul and Lipschutz, 1987). In 1989, Paul and Lipschutz discovered that C1 and C2 chondrites had different siderophile and mobile element concentrations. Kaczaral *et al.* (1989) found L4-6 Antarctic chondrites to have generally lower mobile trace elements than non-Antarctic chondrites. Lipschutz and Samuels (1991) identified shock-dependent trace element abundances among non-Antarctic L4-6 chondrites, but not for Antarctic meteorites of the same types.

1.3.4.5 Cause and Implication of Differences

The major question concerning these and other differences between Antarctic and non-Antarctic meteorites is whether they are terrestrial or extra-terrestrial in origin. Chief among the variables for confusing this issue is terrestrial residence time. With the effects of weathering in the cryogenic Antarctic environment still unknown, and perhaps, unknowable, only a small number of differences can be assigned an origin with any confidence. Much research remains to be performed to resolve this problem.

1.3.4.5a Terrestrial Causes (Weathering and Contamination)

The effects resulting from differences in terrestrial history are not known in detail for the Antarctic situation. There is a consensus among researchers that the current ABCe system (see Section 1.4 below) of indexing weathering intensity among Antarctic meteorites is not sophisticated enough to handle the broad range of weathering effects, or even to quantify the intensity of oxidation (Sears, 1989)[4]. For example, although Dennison and Lipschutz (1987) report finding leaching of trace elements in weathering category C meteorites, no correlations have been found between weathering category and evaporites (Velbel, 1988), bulk

[4] The only benefit that was acknowledged for the ABC system was that it "...does constitute a reasonable record of the curators' observations based on the hand specimens," from Sears, 1989.

chemistry (Jarosewich, 1989), or thermoluminescence sensitivities (Sears, 1989).

It has already been noted that the degree of fragmentation effects the statistical significance of meteorite type frequencies. Other known terrestrial effects include chemical contamination. Dennison and Lipschutz (1987) note that trace elements are often enriched and not depleted in Antarctic meteorites. However, terrestrial contamination (enrichment) of selenium was found to occur consistently in Antarctic eucrites (Mittlefehldt and Lindstrom, 1991). The source of selenium was most likely volcanic tephra dust (Koeberl, 1989; Mittlefehldt and Lindstrom, 1991). Delisle and Sievers (1989) describe uranium contamination in Antarctic chondrites due to close proximity to terrestrial granites in glacial moraines. Differences in carbon isotopic data for CM chondrites were found to be due to the presence of terrestrial hydrous carbonates in the Antarctic samples (Grady *et al.*, 1991).

1.3.4.5b Extraterrestrial Causes (Meteoroid Streams)

Although it is accepted with very few exceptions that the vast majority of meteorites originate within the asteroid belt, non-terrestrial Antarctic/non-Antarctic differences suggest that Antarctic finds may represent a source region that differs (in location within the asteroid belt) from

that of modern falls. This difference in source regions implies the existence of meteoroid streams, defined as a group of meteoroids with similar orbital elements (e.g., Oberst, 1989). Such meteoroid streams, if real, would necessitate the alteration of dynamic sampling models. The current models assume that the source region had been thoroughly homogenized early in the evolution of the asteroid belt, and should not, therefore, produce compositional alterations in the flux of the meteoroids reaching the earth (Wetherill, 1987 and 1989). Wetherill (1986) found that changes in the source region (collision between two asteroids) on time-scales of < 0.1 million years are necessary to account for the meteoroid stream hypothesis as used to explain the Antarctic/non-Antarctic differences. Cosmic ray exposure ages are greater than 1 million years for most meteorites (Schultz *et al.*, 1991). Therefore, if Wetherill is correct, meteoroid streams should not exist.

However, it was postulated by Oberst (1989) that the high density, high energy cluster of impacts recorded on the Moon between June 20 and 30, 1975 by the Apollo seismic network, represented the encounter of the Earth-Moon system with a meteoroid stream. It was further suggested the Farmington meteorite fall (June 25, 1890) may have originated in the same meteoroid stream, as this L5 chondrite had similar orbital parameters and a very young (25,000 years) exposure age.

1.4 The Weathering Index

Central to the problem of assessing the extent to which alteration has progressed on a per-sample basis is the need for a quantitative weathering index or "weatherometer." Campbell and Claridge stated in 1987 that even among terrestrial rocks, "The effects of chemical weathering processes are immediately apparent to the observer in Antarctica, although it may be difficult to gauge their extent." A reliable weathering index is therefore vital to assessing the magnitude of weathering-induced chemical modifications in Antarctic meteorites. This need for accurate indexing is amplified by the strong tendency for meteorites to weather rapidly, due to their generally mafic to ultramafic compositions.

In 1991, Koeberl and Cassidy stated, "For future investigations it will be important to pay more attention to the weathering status of samples and to develop a more reliable and quantitative weathering index." This assertion was made regarding the current Antarctic and non-Antarctic meteorite source controversy, in which weathering is a principal issue, but could apply to any cosmochemical studies involving Antarctic meteorites. Thus, the popularity of Antarctic meteorites in the research community demands a weathering index based on a reliable analytical method that could be put to immediate use.

The best system for measuring weathering intensity would involve a number of simultaneous weatherometers, each of which would focus on a separate "microparagenesis" of terrestrial secondary phase production within the sample (Velbel *et al.*, 1991). Prepared with this information, investigators could then select the samples best suited chemically for a specific project, depending on which terrestrial alterations are considered significant.

A weathering index is a set of values intended to measure weathering intensity. However, due to the potential for taxonomic ambiguity in the special case of meteorite weathering, a precise meaning for "weathering index" must be agreed upon before proceeding further. The gross definition of weathering intensity used in this study, unless otherwise specified (as in the case of iron oxidation), will be as follows:

> The degree to which pre-terrestrial bulk meteoroid chemistries have been cumulatively altered by terrestrial effects.

Note that this definition is specific for chemical alterations and ignores physical weathering. Also, this definition does not refer to specific alterations, but addresses only their collective consequences.

Like the ABCe index, the weatherometers examined in this study will focus on relative abundances of iron oxide formation; hence the term "oxidometer" to describe these indices. **The principle objective of this investigation is to test a viable oxidometer which could function as a complementary alternative to the existing ABCe system for choosing research-quality meteorite samples from the Antarctic collection.** Any index considered suitable for the situation in Antarctica could also find applicability in the newly discovered Australian meteorite fields (Bevan and Binns, 1989). The approach used here is to compare two independent measuring scales, both of which are designed to quantify the severity of iron oxidation, and to evaluate any resulting relationships. If both indices accurately and precisely represent real variations in the weathering intensities of reduced iron in respective meteorite samples, then samples should plot on an X-Y graph, with each index represented by one axis, as a linear trend with a non-zero slope. Another criterion for the usefulness of such an index would be some measure of its reproducibility.

The two experimental oxidometers chosen for this project are (1) a simple petrographic modal analysis of micropetrographic weathering features, and (2) the negative loss on ignition method (-LOI) modified for meteorites by Ann Yates of Arizona State University (Yates, 1988). The

-LOI technique compares weight gains (negative loss) from laboratory-induced oxidation (accelerated weathering) of ferrous and metal iron in a weathered sample of an equilibrated meteorite, with weight gains predicted for an unweathered "fresh" sample of the same taxonomic group. An index value is assigned according to the difference of the two weight gains, thereby indicating the relative amount of rust produced by weathering for that sample.

In the case of Antarctic meteorites, any practical weathering index must be easily and quickly employed for large numbers of samples at a time. While point counting is a time consuming task and therefore not practical for assessing weathering indices for thousands of meteorite samples, -LOI is relatively quick and uncomplicated, and many samples can be assessed simultaneously.

1.5 Scope of Experimentation

The goals of this research are to (1) determine if clay minerals are present in highly weathered ordinary chondrites; (2) examine the potential for applicability of the -LOI experimental oxidometer to the further quantification of Antarctic meteorite weathering intensities; and, as the understanding of meteorite weathering is still in its infancy, (3) investigate any

additional weathering mechanisms or processes which may be revealed during analytical procedures.

19 highly weathered (category C) ordinary chondrites from Allan Hills and Lewis Cliff, Antarctica were obtained from the Johnson Space Center in Houston, Texas through the NASA Antarctic Meteorite Working Group in the form of ≅ 5.0 gram bulk samples and corresponding polished petrographic thin-section microprobe mounts. The chondrites were selected to range in petrologic type from 3 to 6. In addition to modal analysis and negative loss on ignition (-LOI) studies, the samples were examined petrographically for general characterization and photodocumentation (see Appendices A and B). Additional chips from each meteorite were examined petrographically at the Smithsonian Institution National Museum of Natural History, Division of Meteorites, in Washington, D.C. Moreover, three samples were examined by oriented powder mount X-ray diffraction (XRD) analysis for identification of visible and microscopic oxides, as well as a test for the presence of clay minerals for the reasons outlined in Section 1.3.3. XRD analysis, -LOI and petrographic analysis were also performed on the highly weathered non-Antarctic ordinary chondrite Carichic (H5) for comparison with the less weathered Antarctic samples.

2 EXPERIMENTAL METHODS

2.1 Photomicrography

All photomicrographs were taken through a Leitz petrographic microscope with 100 ISO Ektachrome™ slide film. Photographic subjects were chosen according to their relative significance to general and specific weathering problems. An index to photomicrographic transparencies is presented for reference as Appendix B. This index should be examined thoroughly and regarded as a fundamental component of this thesis.

2.2 Modal Analysis

Two separate modal analyses were performed on each of the 19 samples. The first used a petrographic count of 500 points per sample to differentiate opaque, stained and unstained phase volumetric abundances. In this count, stained areas included all types of rust visible in thin section. The unstained category simply referred to areas unaffected by product deposition and included matrix, chondrules and free crystal grains. Total stain values are regarded as

contributing significantly to visually determined ABCe weathering taxonomy. The second count used 500 points per sample to differentiate OPL from non-OPL phases, which were distinguished as will be discussed in Section 3.1.

There were several advantages in point counting OPL material as representative of iron oxide weathering. The material is denser and easier to recognize than most other phases, even when thin. Some structural organization (possibly incipient or complete crystallization) is usually visible in both plane and polarized light, making identification straightforward.

All point counts utilized medium power objectives and the condenser apparatus. The first modal count was performed by making manual adjustments of the mechanical stage, while the second employed an automatic stage-advancing unit. All thin sectioned samples were stored at room temperature in plastic containers with screw-on lids, which in turn were sealed in zip-lock bags.

2.2.1 Difficulties in Modal Analysis

Some difficulties in modal analysis vary with weathering intensity. These problems are described below.

Some samples, such as ALHA85025,10 had very smooth color transitions from light yellow to deep red among the oxide products, making differentiation of OPL and NNL phases difficult. It was necessary to rely on morphological distinctions to identify OPL in such cases where color was not a discriminating characteristic.

The classification under the crosshair of a given secondary feature within the elected set of modal categories becomes increasingly difficult with increasing thin section opacity, particularly with regard to non-crystalline phases. Thus, less weathered samples may be more accurately characterized under the microscope than more weathered samples. This bias will be discussed more fully in Section 3.2.

It was observed in some samples (e.g., ALHA77230,48) that OPL material is heterogeneous in its local distribution, making averaging throughout the meteorite volume very approximate. Because of this intrasample heterogeneity among secondary products, it is clearly necessary for microprobe chips to be sampled from areas on the meteorite that are close to the source from which the 5.0 gram bulk samples were selected in order for -LOI data to yield the best match with petrographic modal data. This information was not provided by NASA when the samples were shipped. However, it is probable that where the chip numbers of microprobe mounts and corresponding 5 gram bulk samples are

consecutive, the chips were located adjacently on the parent rock (refer to Table 4.1).

Due to the tendency for stained areas to grade to high transparency, it is sometimes difficult to distinguish NNL from unstained areas. However, for reasons that will be outlined in Section 4.1.3, the volume percentage of NNL material is anticipated to be negligible, compared to that of the much denser OPL phases. This factor is therefore not considered to be a significant problem for this project. Variations in mount thicknesses were taken into account with regard to stain intensities.

The deepest red OPL outlines were accepted to represent former boundaries of opaque grains (i.e., OPL is pseudomorphous after opaques), and so may be counted in addition to opaques to represent former, pre-weathered opaque volumes. This, when compared with -LOI values should theoretically produce a near linear trend because both are designed to measure the same degree of iron oxidation. However, in cases where unaltered metal particles appeared to grade into OPL products, an approximate interface between OPL and metal would often be identified by secondary reflectance from the metal surface of ambient room light.

2.3 X-ray Diffraction

Samples ALHA77182, ALHA77271 and ALHA84075 were chosen for X-ray diffraction analysis because they are representative of the suite variability of modal total oxide percentages (refer to Table 3.1). X-ray diffraction was performed both to identify secondary mineralogy and as a specific test for the presence of clay minerals.

2.3.1 Sample Preparation and General Pretreatment

Samples were hand crushed with a porcelain mortar and pestle to a maximum estimated particle diameter of 2.0 millimeters. The mortar was carefully scraped with a clean spatula to obtain as much residue as possible. The powder was then suspended in 250 ml of distilled water in 400 ml beakers, and 5.0 ml of Calgon solution was added to inhibit particle flocculation. Each beaker was then transferred to an ultrasound unit and agitated for 10 minutes to further disaggregate the larger particles. After removal from the ultrasound bath, the slurry was first stirred to bring all particles into suspension, then quieted as much as possible with the stirring rod to minimize any horizontal movement. The particles were allowed to settle undisturbed for a pre-calculated amount of time until the undesirable size fractions had descended to a depth of 5.0 cm into the solution. Settling times were 1.7 minutes for 20 μm, and

205.0 minutes for 2 μm size fractions. The liquid above this depth was recovered with a clean pipette inserted to the depth where the maximum desired particle size was determined to be suspended. Approximately 100 ml of this suspension was recovered for each specimen preparation.

A total of 17 preferentially oriented powder mounts was created from the decantates by forcing the settling of suspended material by negative pressure onto 0.20 μm Millipore filters. During the suction process, samples were saturated with glycerol and/or magnesium chloride, as the experiment demanded. These pre-treatments were used in anticipation of detecting and identifying clay minerals, primarily in Carichic, and are not significant for the identification of oxides.

Microscopic metal and silicate particles from the chondrite matrix precluded transfer of the sediments to glass slides. This is usually accomplished by pressing the still-moist mount against the clean glass surface of a slide, and then carefully pealing back the filter. The filters were therefore trimmed and mounted to the glass slides directly (sample-side out) using small pieces of double sided tape. The tape pieces were located strategically along the periphery of the filter to ensure a flat filter surface parallel to the surface of the slide.

All diffractograms were generated at 35 kilovolts, 25 milliamps, a chart speed of 1 centimeter per minute, a scan rate of 1°2θ per minute, using ½/.3/2 filters at 1K or 2K counts per second full scale and a time constant of 2 seconds with CuKα radiation (wavelength = 1.54091Å).

2.3.2 Citrate Dithionite Pretreatment

The citrate dithioninte pretreatment dissolves and removes crystalline iron oxides and oxyhydroxides by the reduction of iron from the ferric to the ferrous state. It was performed on subject samples in the hopes of reducing background noise on diffractograms. Ideally, this enhances reflections of clay minerals. While the attempt was largely unsuccessful in removing iron (background levels remained high), it was found that smaller size fractions produced lower amounts of noise following the pre-treatment relative to higher size fractions. Also the treatment had the effect of revealing the possible presence of akaganéite in the Carichic sample.

The following method is borrowed from Jackson (1967). Approximately 1 gram of sample of the Carichic meteorite was used to test the citrate dithonite treatment. The sample was ground to a powder and added to 40 ml of 0.3 molar sodium citrate solution and 5.0 ml of 1 molar sodium carbonate solution. The mixture was brought to a

temperature of 79°C in a water bath before adding 1 gram of $Na_2S_2O_4$. The solution was then stirred continually for one minute and then for alternating intervals of five minutes. A second 1 gram measure of $Na_2S_2O_4$ was then added and stirred as before, followed by a third 1 gram measure and additional stirring for five minutes. 10 milliliters of saturated sodium chloride solution and 10 milliliters of acetone were then added to the slurry to promote flocculation, followed by thorough mixing with continued heating. The suspension was then centrifuged for 5.0 minutes at 1600-2200 revolutions per minute and the supernatant decanted to remove the dissolved iron. XRD mounts were then prepared from the sediment by adding distilled water and stirring to re-suspend the desired size fractions before allowing them to settle as described above.

2.4 Negative Loss on Ignition

The following procedure is based on that developed by Yates (1988, 1989). Twelve ¼-ounce porcelain crucibles were numbered with a permanent marking pen and heated in an oven at 110°C under negative pressure for twenty-three hours. Each crucible was transferred from the low temperature oven to a digital balance while hot and weighed to four decimal places. The crucibles were then allowed to cool to room temperature over a 30 minute period and re-weighed. This

procedure was performed to determine the weight percentage of absorption by the crucibles of ambient volatile constituents during cooling to room temperature.

It was found that a 0.05 to 0.07 weight percentage increase occurred in each of the twelve crucibles during cooling (see Table 2.1), presumably as a result of water vapor absorption within the porous ceramic structure of the crucibles. As this is a significant increase, it was decided to weigh each crucible while hot during all loss on ignition procedures. Such action would preclude unwanted adjustments of crucible and sample weight values by water vapor.

A high temperature furnace was preheated to 1040°C. Ten crucibles were placed in this environment for four hours, and transferred to the 110°C oven immediately following, before cooling to water vapor absorption temperatures. Here they remained for 5 to 20 minutes before being tare weighed. Immediately prior to weighing, each crucible was delivered a single, brief blast of compressed air along the base to drive away any clinging particulate matter inherited from the furnace or the oven. It was reasoned that the crucibles would be too hot to take on any significant additional weight from the highly volatile constituents in the compressed air. It was then noticed that the numbers made with the permanent marker were no longer discernible. All

Table 2.1. Crucible weights before and after cooling

Crucible number	Hot weight	Cool weight	% weight increase
1	4.3977	4.3997	0.05
2	4.3755	4.3776	0.05
3	4.1739	4.1760	0.05
4	4.3626	4.3651	0.06
5	4.2253	4.2275	0.05
6	4.1898	4.1917	0.05
7	4.3268	4.3297	0.07
8	4.1905	4.1934	0.07
9	4.2462	4.2491	0.07
10	4.1963	4.1989	0.06
11	4.3239	4.3269	0.07
12	4.3266	4.3293	0.06

All weight values in grams

tracking of samples was therefore accomplished by carefully recording their positions in the furnace and oven.

NASA-prepared 5 gram bulk samples arrived in vials sealed within airtight packaging, and are further sealed within zip lock plastic bags. Some vials are plastic, while others are stainless steel. Airtight packages are cut with a pair of scissors and cannot be resealed. Approximately 1 to 1½ grams each of 19 bulk meteorite samples was crushed in a ball mill for 2.5 to 3.0 minutes. Large pieces were selected for the 1990 analysis as preferable to smaller pieces and dust to minimize the effects of laboratory weathering when comparing with point count-determined volumes. Time duration in the ball mill for each sample depended on subjective impressions of relative friability before crushing and on visual inspections of the samples during crushing. In this way a qualitative constancy of maximum grain sizes for all samples was achieved. Between uses, the ball mill was completely disassembled, washed first with hot tap water, then cool distilled water, dried with Kimwipe™ tissues, and allowed to air dry for five minutes in the 110°C oven. Samples were deposited separately in the tare-weighed crucibles and weighed to four decimal places. Crucibles with samples were then transferred to the high temperature furnace, which was preheated to 1040°C. After baking for 4 hours, the samples were removed and re-weighed in the manner outlined above.

Reused crucibles were first cleaned of encrusted meteorite material with a spatula, then rinsed and dried thoroughly. They were then replaced into the high temperature furnace at 1040°C overnight and re-weighed while hot to four decimal places as before. Thus any material incorporated into the ceramic structure from previous samples would be accounted for in the following -LOI procedures.

The -LOI procedure was repeated for all 19 samples and the non-Antarctic meteorite Carichic at a furnace temperature of 1040°C to obtain a second set of results. This second analysis was performed 16 months after the first as a test for reproducibility of weight gains upon ignition and to monitor any addition curatorial weathering effects. The first sample run was performed in November of 1990, and the second in March of 1992. The samples were prepared by NASA in June, July, August, and September of 1988. It was decided to include small chips and dust in the 1992 -LOI analysis as well as larger chips to better detect any shifting in -LOI values over time, since more surface area would be exposed. Thus shifting covers the time period from 1988 to 1992 for this second analysis, not merely a 16-month interval.

3 ANALYTICAL RESULTS

3.1 Petrographic Characterization of Oxides

3.1.1 Antarctic Samples

The most readily identifiable alteration products in the 19 polished thin-sections/microprobe mounts are limonites (iron oxides), which form the basis for the current ABCe weathering index. As is common among terrestrial rocks, such oxides occur in Antarctic meteorites in the form of rust stains, which are usually extinct between crossed nicols, but also exist in other diversified phases, some of which display pronounced birefringence between crossed nicols. Many of these products can be recognized (although not as easily identified) petrographically, and some varieties can be identified mineralogically using X-ray diffraction (XRD) techniques (see Sections 3.4 and 4.2.1.2). This section defines the diagnostic features of the two most common petrographically distinguishable types of rust.

The most widespread oxide visible in thin section is a stain varying in color from very light yellow to deep yellow,

orange, and brown in plane polarized light (Figures 3.1 and 3.2). This material is most often isotropic, modifying birefringence colors where it overlaps grain surfaces, but crystallizes locally, as revealed by unique birefringence colors, internal reflections and extinction characteristics under crossed polarizers (Figures 3.3, 3.4 and 3.5). The neoformation precipitation mechanism, that of constituent chemical species being transported in solution to precipitate at some distance from their source (e.g., Yatsu, 1988), appears to be the dominant formation process for this phase. The phase does not seem to replace primary phases. This is evident by its lack of a preferred association with any primary phase, and by the near ubiquitous occurrence of the stain throughout each specimen observed. Stain locations appear to be governed more by the availability of free-space avenues, than by the location of primary minerals. The color variations are commonly thickness-dependent, as indicated when the material is found near thin edges of certain thin sections. At these places the colors display a sequence of decreasing opacity in plane polarized light from the interior toward the outer edge of the sample.

This neoformed, non-pseudomorphic limonite (NNL) appears as ribbon-like strands, filling grain fractures, cleavage planes and grain interstices throughout much of most specimens. This is consistent with the petrographic observations of terrestrial Antarctic rocks by Cambell and



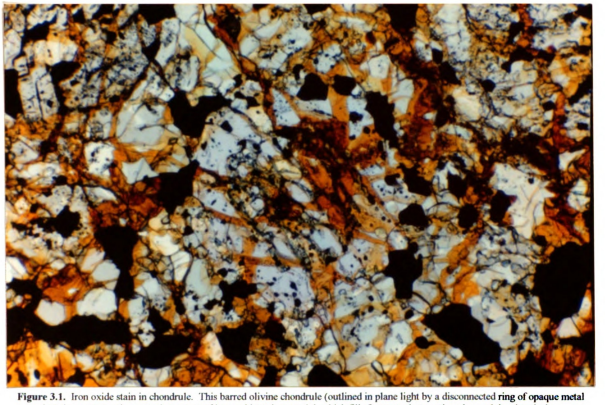


Figure 3.1. Iron oxide stain in chondrule. This barred olivine chondrule (outlined in plane light by a disconnected ring of opaque metal grains) demonstrates the pervasive nature of iron oxide stain material, which fills fractures that continue beyond the chondrule boundaries. In ALHA77288,34. Frame dimensions are 1.0 by 1.5 mm.

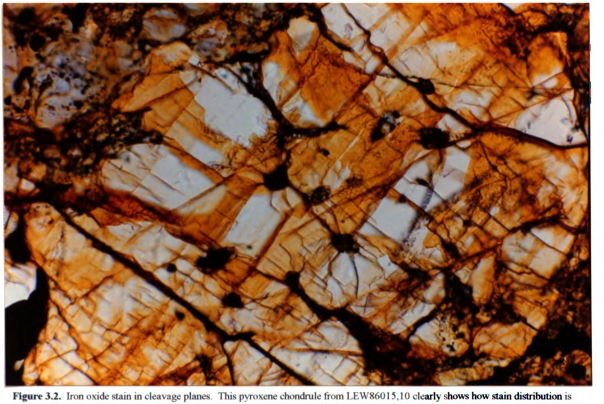


Figure 3.2. Iron oxide stain in cleavage planes. This pyroxene chondrule from LEW86015,10 clearly shows how stain distribution is controlled by available migration pathways such as cleavage planes, grain interstices and fractures. Frame dimensions are 400 by 600 microns.

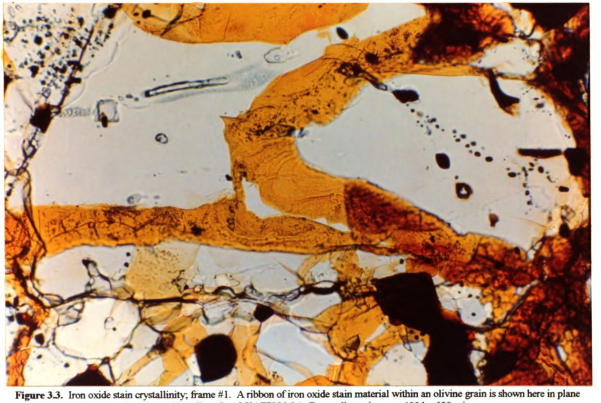


Figure 3.3. Iron oxide stain crystallinity; frame #1. A ribbon of iron oxide stain material within an olivine grain is shown here in plane light. Note subconcentric structural banding. In ALHA77288,34. Frame dimensions are 400 by 600 microns.

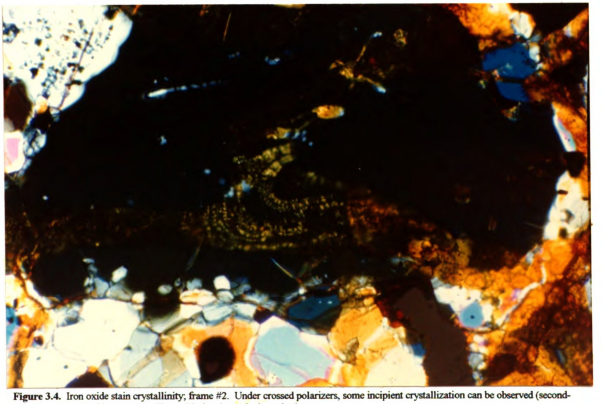


Figure 3.4. Iron oxide stain crystallinity; frame #2. Under crossed polarizers, some incipient crystallization can be observed (second-order yellow birefringent crystallites). Notice the optical continuity.

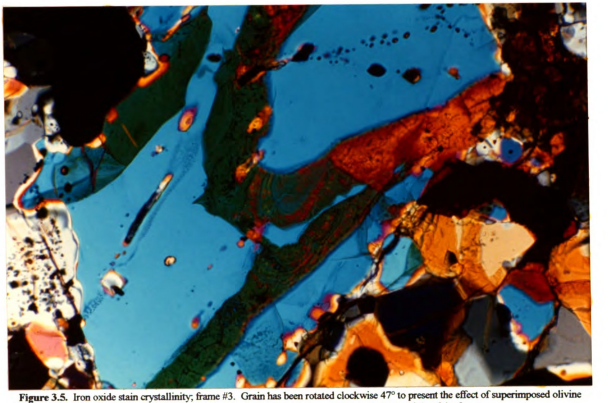


Figure 3.5. Iron oxide stain crystallinity; frame #3. Grain has been rotated clockwise 47° to present the effect of superimposed olivine crystal on oxide stain coloration. Note well-crystallized red and orange region to the lower right of the frame.



Figure 3.6. Opaque-pseudomorphic limonite haloes. Typical example of opaque-pseudomorphic limonite (deep red) replacing metal grains (black). Sample is ALHA84075,7. Frame dimensions are 400 by 600 microns.

Claridge (1987). These strands are very uniform in tone and completeness where they occur, filling the finest fractures with little apparent interruption, and occupying fractures that traverse the entire thickness of the thin-section, as evident by "far" and "near" focusing of the microscope. Under high magnification, a stippled or bubble-like texture to NNL-filled grain fractures is often noticeable, possibly indicating a circumventing migration path of NNL-bearing fluids around points of contact between two fracture surfaces. If such is the case, these residual points of contact between separating crystal surfaces would indicate that separation had not progressed very far prior to fluid migration through the avenue.

The second common oxide phase often has a deep red color in plane polarized light, displays high birefringence colors between crossed polarizers and possesses well-defined outlines (Figures 3.6, 3.7 and 3.8). This opaque-pseudomorphic limonite (OPL) phase occurs most frequently as haloes and partial haloes surrounding opaque grains, but occasionally is found expanding away from opaque phases into free spaces (Figures 3.9, 3.10, 3.11, and 3.12). Evidence for in-situ alteration of opaque grains is that opaque/OPL interfaces are frequently embayed or sutured, in contrast to the smooth boundaries of opaque minerals not associated with OPL. Although deep red is the color most often encountered, many examples of OPL exist which have orange or yellow hues.

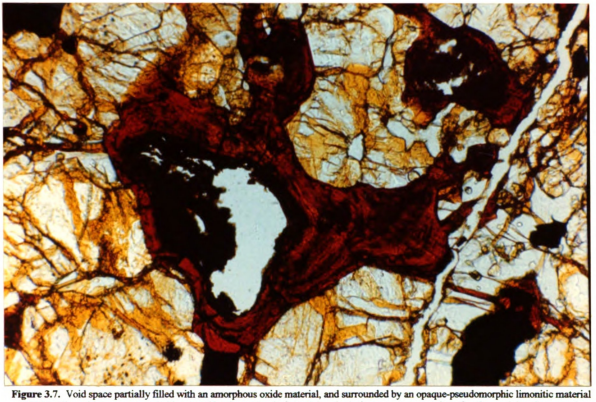


Figure 3.7. Void space partially filled with an amorphous oxide material, and surrounded by an opaque-pseudomorphic limonitic material (OPL). The void space was probably caused by the removal of a metal grain during mount preparation after the partial replacement by the OPL. From ALHA81027,26. Frame dimensions are 400 by 600 microns.

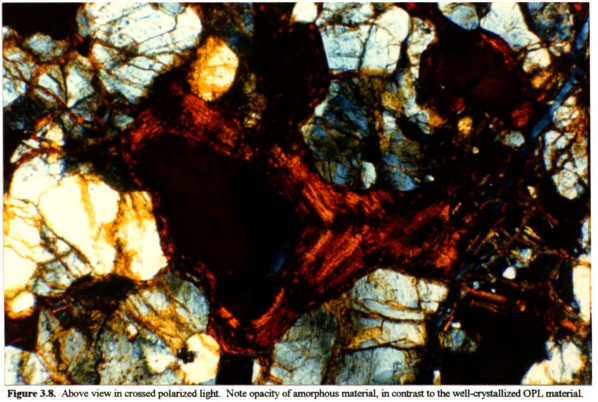


Figure 3.8. Above view in crossed polarized light. Note opacity of amorphous material, in contrast to the well-crystallized OPL material.



Figure 3.9. A well-defined OPL deposit appears to be expanding into the free space beyond the meteorite's surface and separating from the inferred primary opaque metal grains. Note embayments into metal grains, coalescence of material beyond the primary grains, and fractures along lamellae which are subparallel with opaque grain surface. From LEW86015,10. Frame dimensions are 400 by 600 microns.

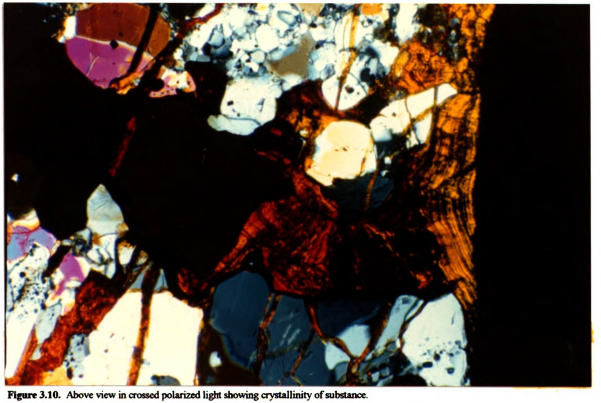


Figure 3.10. Above view in crossed polarized light showing crystallinity of substance.



Figure 3.11. Another example of OPL material at a sample boarder expanding into the free space beyond, and into nearby fractures. Note deep embayments within primary opaque material. From LEW85332,11. Frame dimensions are 400 by 600 microns.

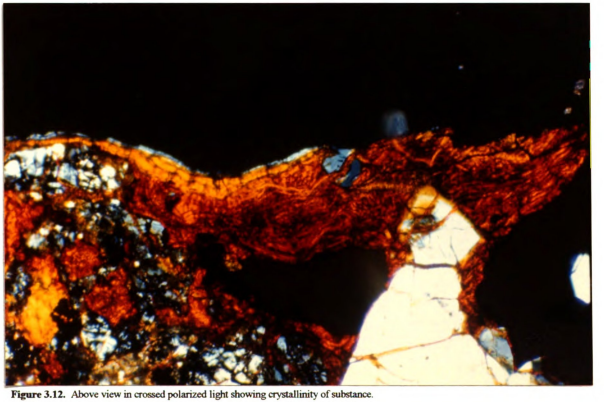


Figure 3.12. Above view in crossed polarized light showing crystallinity of substance.

The color variations are proportional to microprobe mount thickness, and can be observed both in plane polarized and cross polarized light (Figures 3.11 and 3.12). Figure 3.13 shows an opaque grain at the ALHA81027,26 thin section boundary which appears to be altering and disintegrating systemmatically, apparently facilitated by the expansion of growing OPL alteration product visible within. This image appears strikingly similar to the textbook description of soil formation on a bedrock surface in cross-section.

OPL and NNL are the two most common oxide types observed in thin section. They are usually easy to distinguish from each other. The OPL material appears to have strong relief, while the NNL material has low relief with color variations appearing simply to be various intensities of surface staining.

Other, less common phases and phase habits include the following: (1) Transparent limonite fracture fillings (TLFF), birefringent deposits appearing similar to OPL deposits but filling fractures, and having their locations farther from likely opaque source minerals than OPL phases, suggesting higher mobility of their constituents than typical OPL minerals (Figures 3.14 and 3.15); (2) Opaque limonite fracture and void space fillings (OLFF), similar to TLFF but appearing opaque in plane and polarized light, and lining the walls of both fractures and void spaces (example

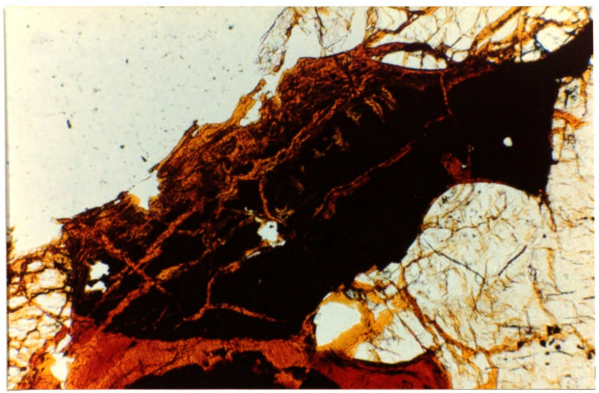
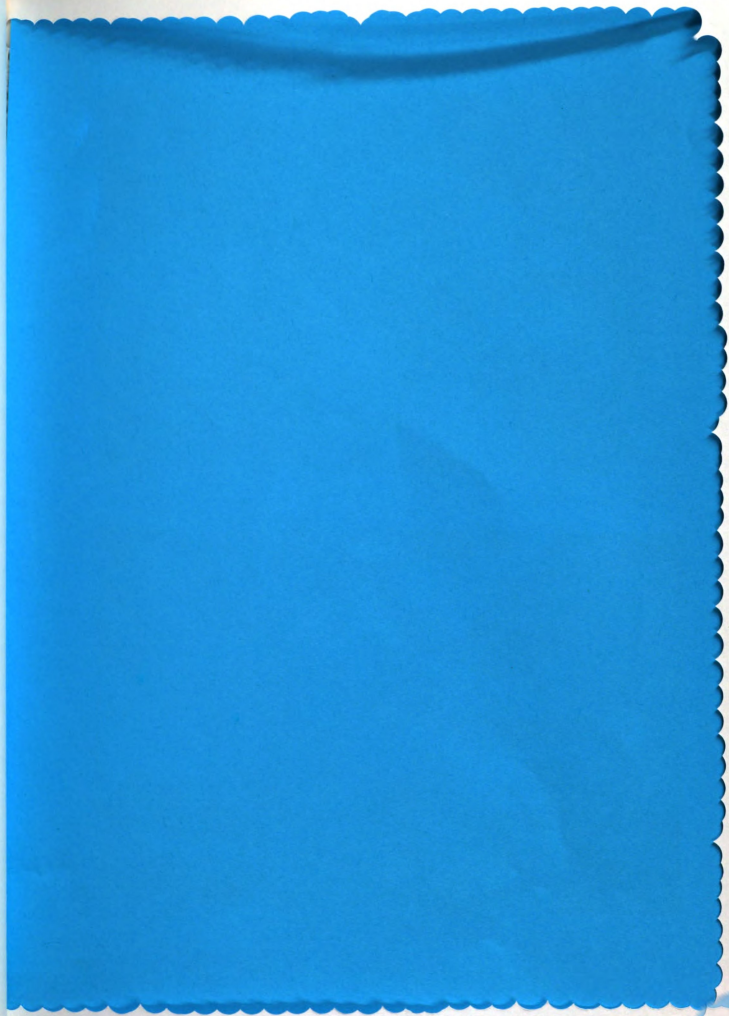
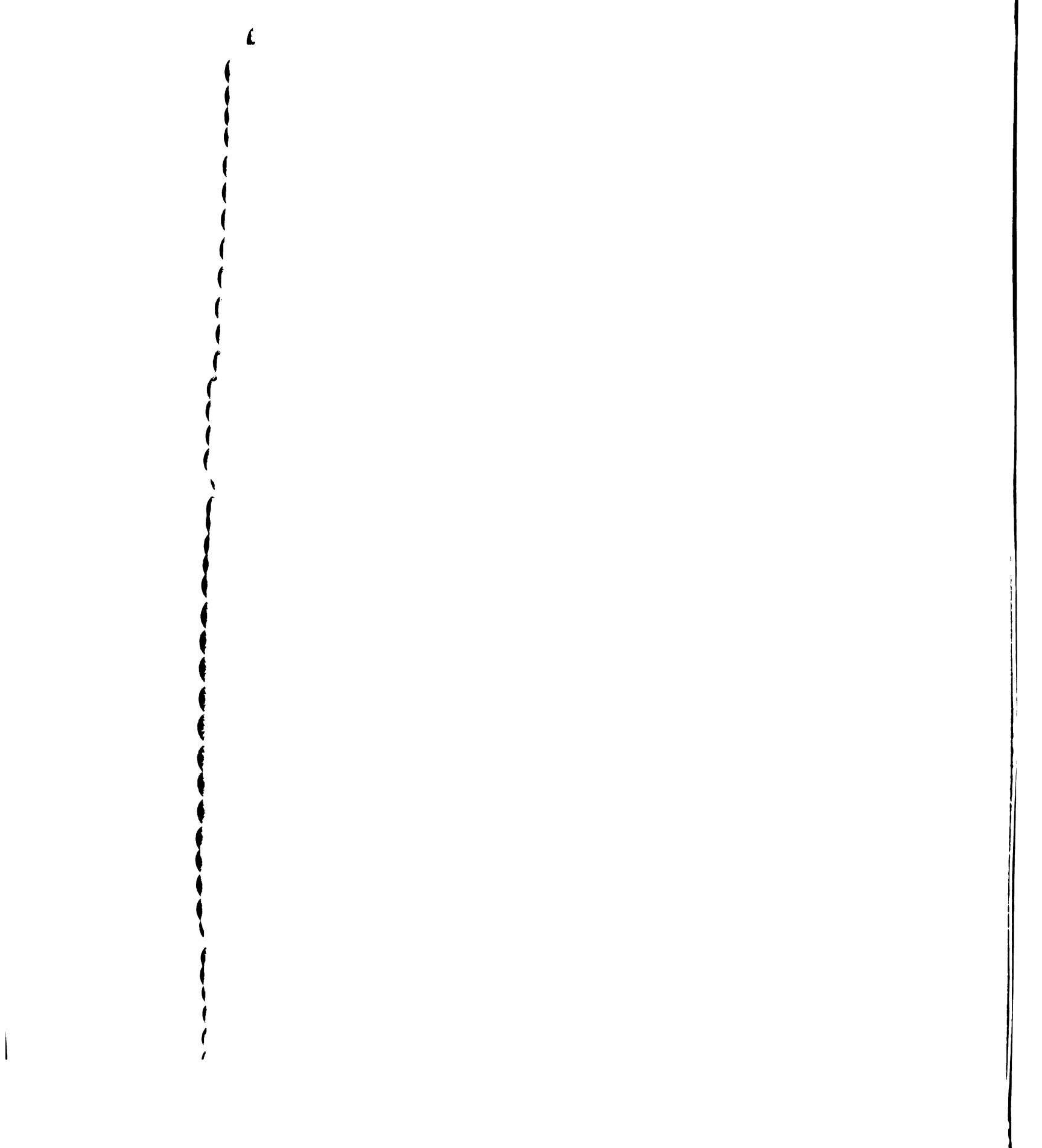


Figure 3.13. Disintegrating opaque grain. Attack of alteration proceeds similar to classic "soil horizon formation on bedrock" scheme, with a gradation from product, to product and primary, to all primary material, from the outer edge to the interior. This suggests a mechanical breakdown of metal grains may accompany and assist chemical alteration. Oxide-filled avenues are suborthogonal, possibly reflecting mineral structure within the grain. From ALHA81027,26. Frame dimensions are 400 by 600 microns.





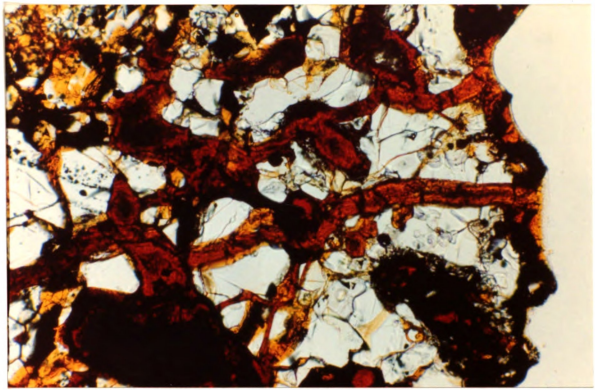


Figure 3.14. Transparent limonite fracture fillings. Well crystallized, well integrated. Oxide appears to take advantage of existing shock-fractures. Oxide fillings are wide (> 25 microns), and so appear to have been widened from their original width, which presumably was of submicron thickness. From ALHA85025,10. Frame dimensions are 400 by 600 microns.

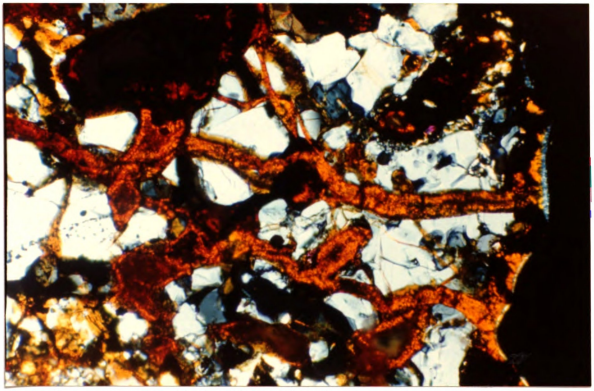
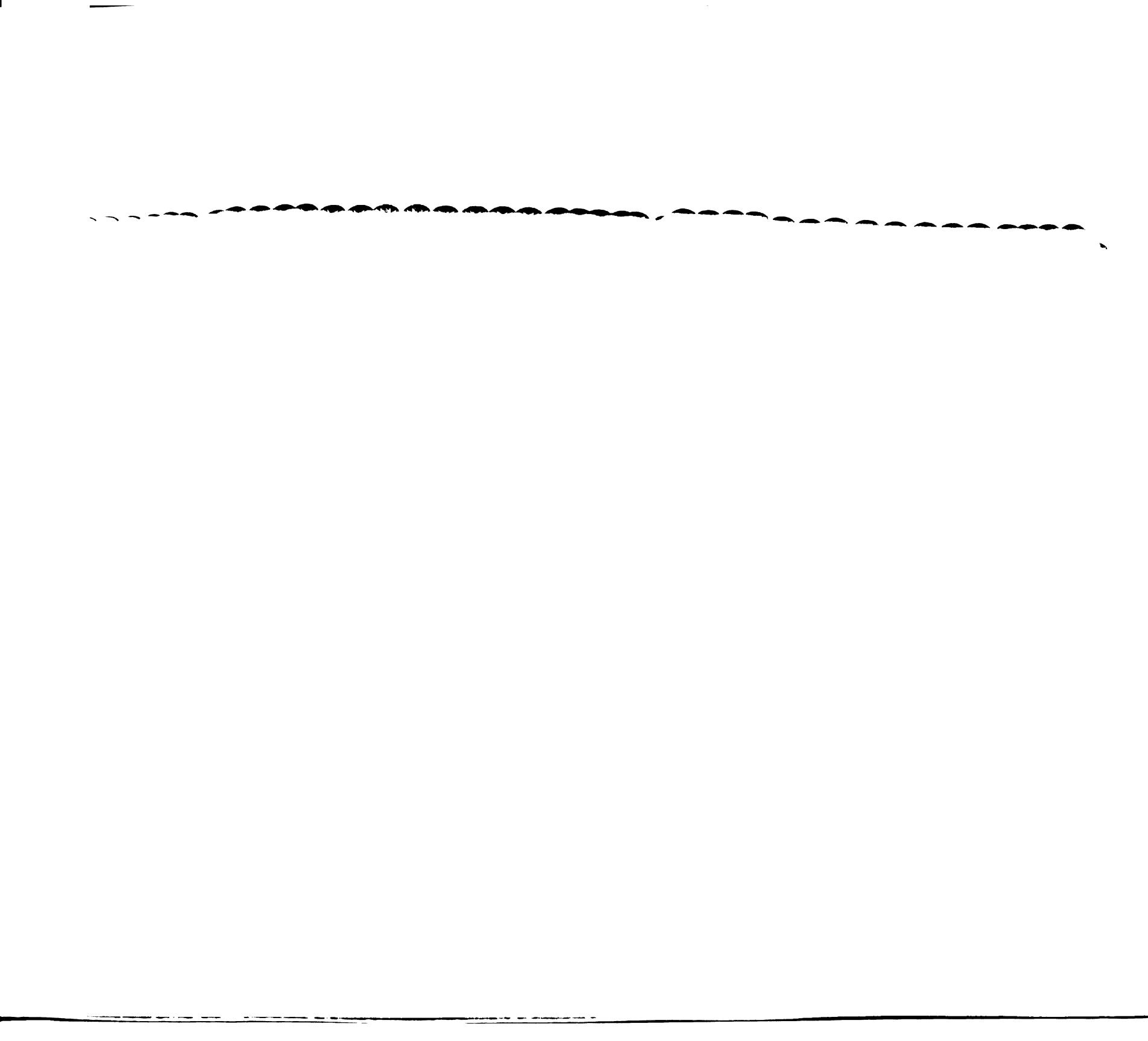


Figure 3.15. Above view in crossed polarized light. Material is well-crystallized.



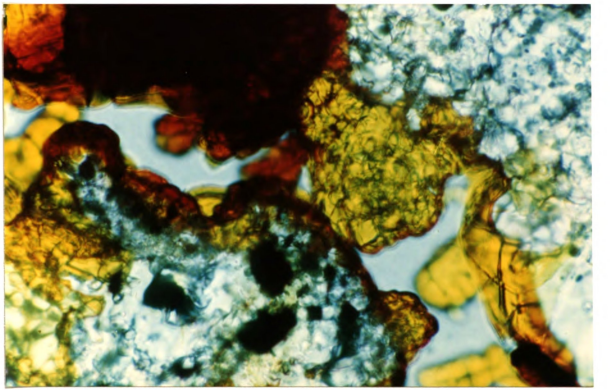
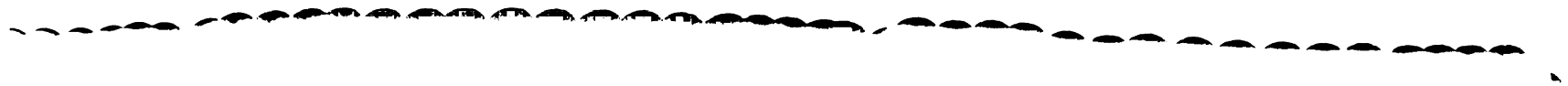


Figure 3.16. Botryoidal void space fillings. Rust deposits lining void spaces in botryoidal habit. The depth of field is apparent by the differences in focus among the various protruding bulbs. From ALHA77271,28. Frame dimensions are 160 by 240 microns.



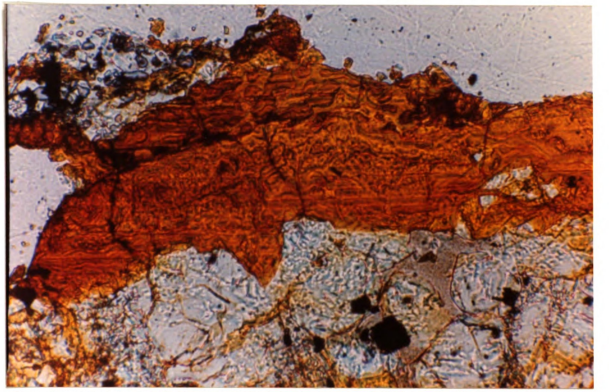


Figure 3.17. Sharp contact phase. Oxides are not associated with any opaque grains in the plane of the thin section. It is difficult to determine whether striae are genetic in origin or the result of a saw blade. The patterns may be related to the primary crystal structure primary to replacement. In ALHA77004,22. Frame dimensions are 160 by 240 microns.

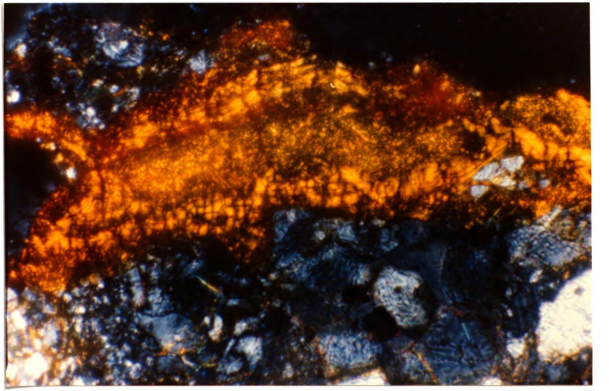
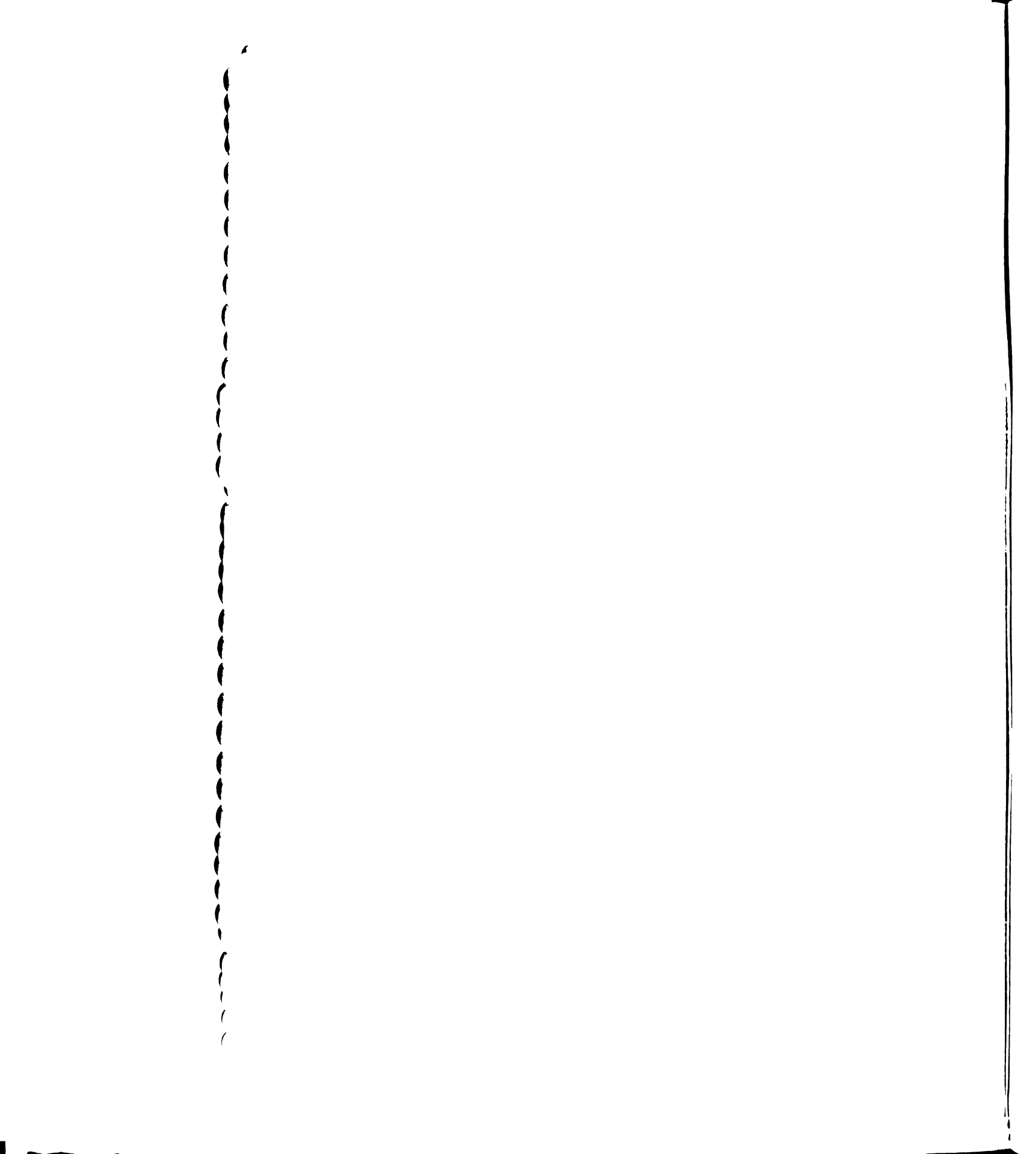


Figure 3.18. Above view in crossed polarized light. Again, the material is well-crystallized.



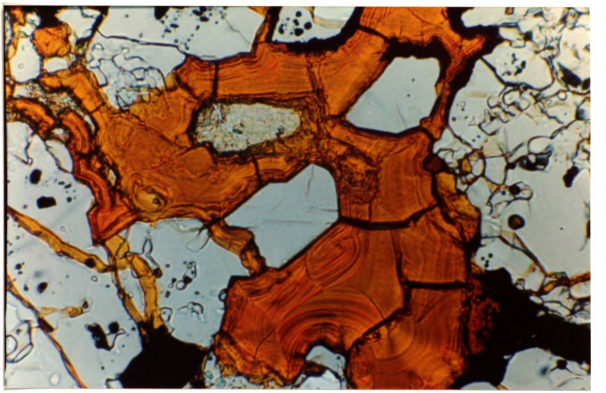


Figure 3.19. Sharp contact phase. Another example of a sharp contact phase. Some remnant opaque material persists with highly sutured edges. Note concentric internal structure. From ALHA77271,28. Frame dimensions are 160 by 240 microns.

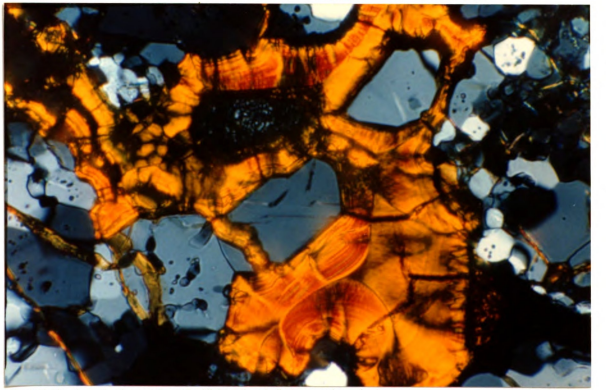


Figure 3.20. Above view in crossed polarized light. Minerals display sweeping extinction.

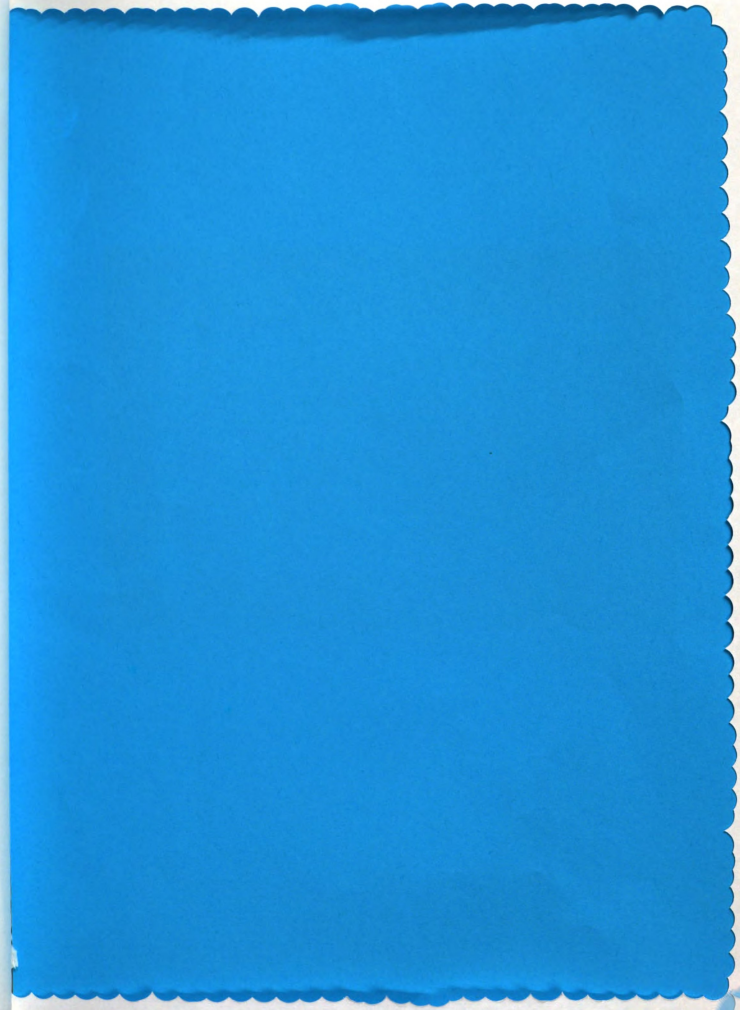




Figure 3.21. Carichic. Thin section of Carichic in reflected light. Bright flecks are kamacite and taenite grains. Dendritic fractures transect the specimen axial to notable dark-stained veins devoid of metal grains. Thin section dimensions (glass slide) are approximately 1 by 1¾ inches.

visible in Figures 3.7 and 3.8). This material can also have a structurally weak, "fluffy" appearance when found within a void space; (3) Botryoidal void space fillings (BVF), intricate, often orange colored deposits with bulbous or botryoidal morphologies that partially fill some void spaces (Figure 3.16); (4) Sharp contact phases (SCP), well-defined bodies of oxide having very clean contacts with silicate phases, often showing well-developed laminar or concentric internal structures, conspicuous by the lack of nearby opaque material (Figures 3.17, 3.18, 3.19, and 3.20). These minerals may simply represent the complete replacement of opaque grains by OPL material. It is important to note that these morphologic differences do not necessarily reflect mineralogical differences. For example, TLFF, BVF and SCP may be the same mineral, but identified at different stages of development or in different habits.

3.1.2 Carichic

Carichic is a 17 kilogram H5 1983 find from Chihuahua, Mexico and is catalogued as extremely weathered (Graham *et al.*, 1984). The density of oxide product was too high to permit study of oxides under transmitted light. However, Figure 3.21 is an off-axis photograph of a Carichic thin section in refelcted light. Immediately apparent are the highly reflective residual taenite and kamacite grains (opaque in transmitted light), which appear well preserved

in regions removed (approximately 2 mm distant) from fractures that crosscut the section, and entirely absent in regions close to fractures. Also, the metal-vacant area is remarkably symmetric about the fractures. Closely paralleling this pattern are zones of lighter and darker oxide staining.

3.2 Modal Analysis

Petrographic modal analysis data are presented in Table 3.1. The materials comprise three main categories including (1) total counted opaque phases, (2) total unstained silicates (identified as clear areas in plane light), and (3) total identifiable oxides. The oxides are then further broken down into OPL and non-OPL categories. Non-OPL includes, obviously, all forms of rust not classified as OPL.

Table 3.2 presents the average normative mineralogy of H- and L-group ordinary chondrites. All modal opaque values obtained for the study samples fall consistently near average normative values for chromite, ilmenite, troilite and nickel-iron (opaque mineral) volume total abundances. Normative mineral abundances for ordinary chondrites are nearly identical to their modal proportions, particularly in types 4 and higher (Dodd, 1981); volumetric abundances will

Table 3.1
Modal Analytical Results

	Point count #1; 500 points			Point count #2; 500 points			
Specimen	Opaque	Unstained	Total Oxides	OPL	Non-OPL	OPL/(OPL + Opaques) x 100	OPL + Opaques
ALHA81031,19	11.0	32.8	56.2	3.4	52.8	23.6	14.4
ALHA77230,48	13.0	30.4	56.6	2.0	54.6	13.3	15.0
ALHA81027,26	12.4	8.8	78.8	4.2	74.6	25.3	16.6
ALHA77004,22	13.4	25.8	60.8	5.8	55.0	30.2	19.2
ALHA77208,29	16.6	23.6	59.8	10.8	49.0	39.4	27.4
ALHA77225,18	15.4	29.0	55.6	4.4	51.2	22.2	19.8
ALHA77226,37	15.2	16.6	68.2	8.6	59.6	36.1	23.8
ALHA77232,16	13.2	22.6	64.2	3.0	61.2	18.5	16.2
ALHA77233,21	13.0	23.2	63.8	6.4	57.4	33.0	19.4
ALHA77182,36*	10.4	48.2	41.4	26.4	15.0	71.7	36.8
ALHA79025,16	15.4	33.8	50.8	7.4	43.4	32.5	22.8
ALHA79029,21	11.6	19.2	69.2	7.2	62.0	38.3	18.8
ALHA84075,7*	15.6	10.2	74.2	5.6	68.6	26.4	21.2
ALHA85025,10	17.0	37.0	46.0	12.8	33.2	43.0	29.8
ALHA77271,28*	13.2	28.4	58.4	13.4	45.0	50.4	26.6
ALHA77288,34	16.0	26.2	57.8	11.2	46.6	41.2	27.2
ALHA84082,9	18.8	27.4	53.8	15.2	38.6	44.7	34.0
LEW85322,11	16.4	65.6	18.0	16.8	1.2	50.6	33.2
LEW86015,10	17.0	13.4	69.6	9.4	60.2	35.6	26.4
Arithmetic mean	14.5	27.5	58.1	9.2	48.9	35.6	23.6
Standard deviation	2.2	12.9	13.1	5.8	17.2	13.2	6.5

The two oxide counts in point count #2 represent the breakdown of the total oxides count of point count #1
All modal values in percents
*** corresponding bulk samples used in XRD analysis**

Table 3.2. Modal opaque mineral percentages

Meteorite	Class	Modal % opaque				Reference
		Fe-Ni	Troilite	Chromite	Total	
L Chondrites						
Junction, Texas	L5d	4	8	0.7	12.7	Ehlmann & Keil, 1987
Qidong, China	L5d	4.7	4.3	nr	9	Wang & Ruben, 1987
Bayard	L5	6.4	nr	nr	6.4	Struempler & Kaelin, 1987
Reliegos	L5	6.1	nr	nr	6.1	McCoy et al., 1990
Roosevelt County 025	L5a	1.3	6.2	nr	7.5	Pen et al., 1990
Roosevelt County 028	L5a	3.9	6.5	nr	10.4	Pen et al., 1990
Roosevelt County 066	L5a	0	1.6	nr	1.6	Pen et al., 1990
Roosevelt County 067	L5a	1.3	4.6	nr	5.9	Pen et al., 1990
Roosevelt County 068	L5a	0.4	3	nr	3.4	Pen et al., 1990
Roosevelt County 069	L5a	0.4	3.5	nr	3.9	Pen et al., 1990
Roosevelt County 074	L5(S3)	Trace	1.5	nr	1.5	McCoy et al., 1993
Roosevelt County 076	L4(S3)	3.7	4.6	nr	8.3	McCoy et al., 1993
Roosevelt County 077	L4(S2)	Trace	6.6	nr	6.6	McCoy et al., 1993
Roosevelt County 078	L4(S2)	2	6.2	nr	8.2	Gomes & Keil, 1980
		Normative % opaque				
Average values		7.5	6.1	0.6	14.4*	Dodd, 1981
H Chondrites						
Olton, Texas	H	11.2	4	nr	15.2	Keil et al., 1990
Dalhart, Texas	H5a	1	3	nr	4	Ehlman & Keil, 1987
Rosebud, Texas	H5c	8	4	nr	12	Ehlman & Keil, 1987
Cranfills Gap, Texas	H6c	1	4	nr	5	Ehlman & Keil, 1987
Ingella Station	H5a	13.6	5.4	nr	19	McCoy & Keil, 1988
Molina	H5	21.1	7	0.7	28.8	McCoy et al., 1990
Guarena	H6	20.7	4.8	1.1	26.6	McCoy et al., 1990
Olmedilla de Alaron	H5	20.9	nr	nr	20.9	McCoy et al., 1990
Springer, Oklahoma	H5(S3)	15	5.3	nr	20.3	Ehlman & Keil, 1992
Roosevelt County 073	H5(S2)	1.9	4.6	nr	6.5	McCoy el al., 1993
Anton, Texas	H4b	19	8	nr	27	Ehlman & Keil, 1987
Venus, Texas	H4d	15	8	nr	23	Ehlman & Keil, 1987
Hashima	H4	8.2	5.8	nr	14	Hohino & Suea, 1992
Allen, Texas	H4(S2)	8	oxides	nr	8	Ehlman & Keil, 1992
May Day, Kansas	H4(S2)	14.5	4.7	nr	19.2	Ehlman & Keil, 1992
Pony Creek, Texas	H4(S3)	8.1	5.4	nr	13.5	Ehlman & Keil, 1992
		Normative % opaque				
Average values		18.6	5.3	0.6	24.7*	Dodd, 1981

Fe-Ni = Iron-nickel metal
nr = Not reported
Many of the low values are low because of weathering
* includes ilmenite

be discussed more thoroughly in Section 4.2.2.3. This is therefore accepted as evidence for the accuracy of the point count.

An iron oxide weatherometer derived from petrographic modal analysis cannot simply be a measure of the total rust point counted in thin section. This is because the volume of secondary species, which can be defined as mineral thickness per unit cross-sectional area of microscope stage, is not a constant. NNL films seldom span the perpendicular cross-sectional distance from the top to the bottom of the thin section, while other materials, such as OPL, apparently do. Thus varying relative abundances of these different materials will yield modal indices that are out of proportion to actual rust product volumes. The geometry of this phenomenon will be illustrated in Section 4.1.3.

In addition, H ordinary chondrites have greater reduced metal fractions than L ordinary chondrites. In this study the volume of NNL staining is taken to be negligible compared to OPL volumes for the reason stated above. As OPL material is considered an *in-situ*, pseudomorphic replacement of reduced opaque phases, the weathering index for the point count results will represent the volume percentage of such replacement, i.e., OPL/(OPL + Opaques) x 100. The rationale for assuming isovolumetric replacement is clarified in Section 4.2.2.1. This calculation produces a metal

oxidation index that ranges from 0 to 100 percent (Figure 3.22).

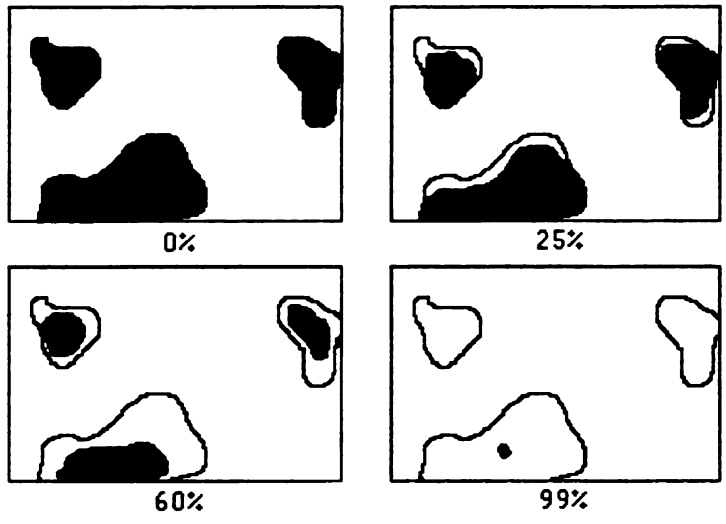


Figure 3.22. Theoretical opaque metal grain (black) replacement by pseudomorphic limonitic material (OPL) (white within outlines).

3.3 X-ray Diffraction

X-ray diffraction data is presented as Appendix C. The non-Antarctic ordinary chondrite Carichic (an H5 find) was recovered in 1983 from the humid to semi-arid climate region of Chihuahua, Mexico. It is in an advanced stage of weathering (Graham *et al.*, 1984) which probably exceeds by far that of any Antarctic specimen. It was investigated for comparison with the Antarctic samples as a possible indicator of mineral assemblages toward which chemical weathering of ordinary chondrites may be progressing in the Antarctic environment; and to assist in assessing the long term evolution of weathering meteorites in general.

Oxide mineral identification is particularly difficult in the case of ordinary chondrites. X-ray backscatter from the metal particles in the matrices of ordinary chondrites is a significant problem. Some metal particles are small enough that they are not separated from clay-size silicates during sample preparation, but remain suspended within the sampled water column along with secondary phase particles, and therefore become included in the oriented powder mount.

With the exception of the citrate dithionite-treated Carichic samples, the ≤ 20 μm size fractions produced lower background intensities than the ≤ 2 μm size fraction. It may be that particle size distributions for ordinary chondrite matrices, which are essentially poorly sorted sediments, are skewed toward the smaller size fractions, as with some terrestrial diamictites (e.g., Flint, 1970). We therefore find much more primary material incorporated within the powder mount than experience with weathered terrestrial rocks might lead us to expect. Also, larger size fractions contain larger crystals, which produce more intense peaks. It was thus found that the ≤ 2 μm size fraction produced correspondingly lower peak amplitudes and poorer peak definition than the ≤ 20 μm fraction. The ≤ 20 μm particle size was therefore sampled most frequently for the XRD analysis.

The natural superimposition of oxide peaks with each other and with those of the primary phases also exacerbates the task of mineral identification. This problem has been encountered before with the identification of secondary minerals in meteorites (Barber, 1985; Zolenski and McSween, 1988; Yates, 1988). Examples include the 2.51Å olivine peak, which overlaps 2.53Å, 2.51Å, 2.51Å, and 2.49Å peaks for magnetite, maghemite, hematite, and goethite respectively. The 2.69Å goethite peak overlaps the 2.69Å hematite peak, and the 2.95Å maghemite peak overlaps the 2.92-2.95Å plagioclase peak. Because of this, oxide mineral detection and identification are often reduced to the identification of single diagnostic peaks. These peaks are considered diagnostic only if at or close to the maximum (100 percent) relative peak height.

Another probem is that incomplete isomorphous substitution of ions within the crystal structure can affect line positioning in iron oxides and oxyhydroxides (Dixon and Weed, 1982). This uncertainty increases the potential for confusing minerals with similar d-spacings.

3.4 Negative Loss on Ignition

Results from the loss on ignition measurements are presented in Tables 3.3a and 3.3b. Meteorites are represented by

Table 3.3a
Negative loss on ignition data for Autumn of 1990

A	B	C	D	E	F	G	H	I
Crucible number	Specimen identification	Tare mass	Crucible + sample mass 110°C	Pre-ignition sample mass D - C	Crucible + sample mass 1040°C	Post-ignition sample mass F - C	% -LOI (G - E)/E x 100	Oxidation index
	L-3s							100 - (H/4.4 x 100)
19	ALHA81031,17	4.3279	5.4757	1.1478	5.4733	1.1454	-0.21	NA
	L-4s							
6	ALHA77230,29	4.1896	5.2676	1.0782	5.2955	1.1059	2.57	41.59
	L-6s							
10	ALHA81027,25	4.1971	5.2929	1.0958	5.3214	1.1243	2.60	40.90
	H-4s							100 - (H/8.4 x 100)
2	ALHA77004,21	4.3765	5.3490	0.9725	5.3914	1.0149	4.36	48.10
1	ALHA77208,28	4.3979	5.2824	0.8845	5.3366	0.9387	6.13	27.02
3	ALHA77225,16	4.1738	5.1836	1.0098	5.2283	1.0545	4.43	47.26
13	ALHA77226,34	4.3632	5.4464	1.0832	5.5014	1.1382	5.08	39.52
7	ALHA77232,14	4.3275	5.4572	1.1297	5.5219	1.1944	5.73	31.79
18	ALHA77233,20	4.2265	5.2304	1.0039	5.2779	1.0514	4.73	43.69
	H-6s							
14	ALHA77182,21	4.1919	5.5130	1.3211	5.5336	1.3417	1.56	81.43
9	ALHA79025,03	4.2470	5.4689	1.2219	5.4901	1.2431	1.74	79.29
8	ALHA79029,20	4.1915	5.2988	1.1073	5.3259	1.1344	2.45	70.83
4	ALHA84075,02	4.3626	5.5380	1.1754	5.5965	1.2339	4.96	40.71
16	ALHA85025,09	4.1973	5.3569	1.1596	5.4032	1.2059	3.99	52.50
	H-8s							
12	ALHA77271,27	4.1744	5.2851	1.1107	5.3483	1.1739	5.69	32.26
5	ALHA77288,30	4.2255	5.4343	1.2088	5.4914	1.2659	4.72	43.81
17	ALHA84082,06	4.1904	5.3879	1.1975	5.4400	1.2496	4.35	48.21
11	LEW85322,09	4.3985	5.5084	1.1079	5.5468	1.1483	3.65	58.55
15	LEW86015,09	4.2473	5.4330	1.1857	5.4831	1.2358	4.23	49.64

Values for columns C through G in grams.
NA = not applicable.

Table 3.3b
Negative loss on ignition data for Spring of 1992

A	B	C	D	E	F	G	H	I
Crucible number	Specimen identification	Tare mass	Crucible + sample mass 110°C	Pre-ignition sample mass D - C	Crucible + sample mass 1040°C	Post-ignition sample mass F - C	% -LOI (G - E)/E x 100	Oxidation index
	L-3s							100 - (H/4.4 x 100)
34	ALHA81031,17	4.3645	6.0016	1.6371	5.9876	1.6231	-0.86	NA
	L-4s							
21	ALHA77230,29	4.3245	5.7209	1.3964	5.7521	1.4276	2.23	40.91
	L-6s							
24	ALHA81027,25	4.3767	5.8174	1.4407	5.8484	1.4717	2.15	40.91
	H-4s							100 - (H/8.4 x 100)
25	ALHA77004,21	4.2478	5.6627	1.4149	5.7117	1.4639	3.46	58.81
26	ALHA77208,28	4.3640	5.7573	1.3933	5.8296	1.4656	5.19	38.21
20	ALHA77225,16	4.1914	5.6794	1.4880	5.7305	1.5391	3.43	59.17
37	ALHA77226,34	4.3305	5.7828	1.4523	5.8513	1.5208	4.72	43.81
23	ALHA77232,14	4.3968	5.5890	1.1902	5.6466	1.2478	4.84	42.38
36	ALHA77233,20	4.3768	5.7726	1.3958	5.8009	1.4241	2.03	75.83
	H-5s							
32	ALHA77162,21	4.1949	5.1253	0.9304	5.1347	0.9398	1.01	87.96
35	ALHA79025,03	4.2489	5.9206	1.6717	5.9532	1.7043	1.95	76.79
28	ALHA79029,20	4.1743	5.5734	1.3991	5.5968	1.4225	1.67	80.12
27	ALHA84075,02	4.1930	5.6642	1.4712	5.7380	1.5450	5.02	40.24
30	ALHA85025,09	4.3994	5.7183	1.3189	5.7814	1.3820	4.78	43.10
22	Carichic	4.3290	5.6624	1.3334	5.6483	1.3193	-1.06	NA
	H-6s							
33	ALHA77271,27	4.1922	4.9569	0.7647	5.0047	0.8125	6.25	25.60
29	ALHA77288,30	4.3274	6.0257	1.6983	6.1068	1.7794	4.78	43.10
38	ALHA84082,06	4.3268	5.8513	1.5245	5.9159	1.5891	4.24	49.52
31	LEW85322,09	4.3281	5.6207	1.2926	5.6781	1.3500	4.44	47.14
39	LEW86015,09	4.1752	5.6023	1.4271	5.6736	1.4984	5.00	40.48

Values for columns C through G in grams.
NA = not applicable.

their identification numbers in order of increasing class and petrologic type designations. In the tables, column C presents the mass in grams of each tare-weighed crucible. Columns D through G present the mass in grams of each sample, separately and together with its respective crucible, prior to and immediately following ignition. Column H then gives the percent difference between the pre- and post-ignition sample masses. Column I is the oxidation index, defined as;

$$OI = 100 - \frac{H}{4.4} \times 100$$

for L chondrites, where H is the value given in column H and 4.4 is the average percent weight gain for unweathered L chondrites as determined by Yates, (1988); and;

$$OI = 100 - \frac{H}{8.4} \times 100$$

for H chondrites, where 8.4 is the average percent weight gain for unweathered H chondrites as determined by Yates, (1988). Thus, a scale of 0 to 100 percent will represent the possible range of values resulting from a suite of samples with metal and sulfide grains that are 0 to 100 percent oxidized.

The first 19 tests were conducted in November of 1990, and the last 20 during March of 1992. The second -LOI data set was obtained in an attempt to monitor any additional weathering that may have occurred in the samples while in storage. Carichic is too heavily oxidized (containing too much opaque material) for petrographic modal analysis.

4 DISCUSSION

4.1 Graphical Representation of Data

4.1.1 Modal Analysis

Figure 4.1 presents the results of the modal analysis using the three most basic petrographic components; (1) primary opaque material, (2) unstained silicates, and (3) total oxides. Immediately apparent is that even among the most weathered Antarctic meteorites, some opaque material has remained. Also to be noted is the narrow range of these residual opaque mineral abundances. Notice too the spread in values perpendicular to the "opaques" end-member. Although the data points cluster near the "total oxides" end-member, where one would expect to find weathering category C ordinary chondrites, there is considerable overlap into "less stained" areas of the diagram.

The ABCe oxidometer has five categories to encompass the entire range of iron oxide production observed so far in Antarctic meteorites. The intent behind these categories is to measure the fraction of exterior surface area that is

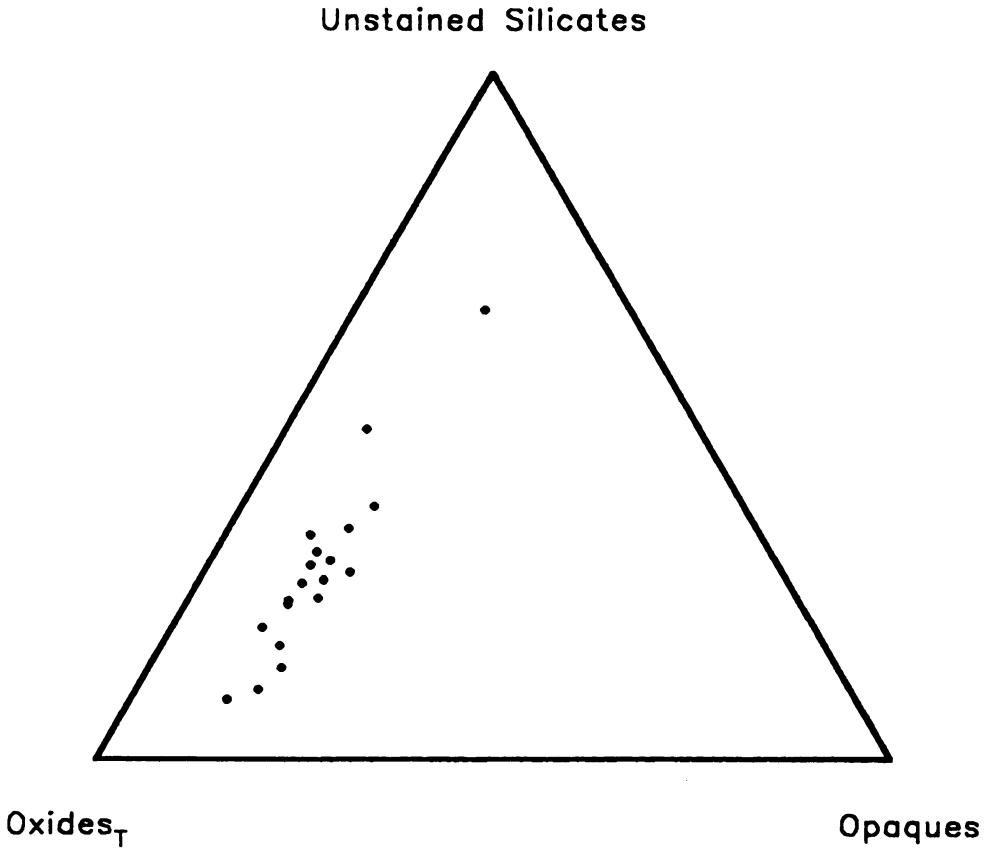


Fig. 4.1. Modal analytical data plot in terms of three most basic components.

visibly (in hand specimen) discolored by rust. The five categories can be defined precisely by allowing each to represent one fifth of the total possible range from 0 to 100 percent stained. Weathering category A would then represent 0 to 20 percent; A/B, 20 to 40; B, 40 to 60; B/C, 60 to 80; and C, 80 to 100 percent stained (Figure 4.2). In actuality, the most intensely weathered Antarctic meteorite is probably far less than 100 percent oxidized (all metal grains consumed by oxidation). The category ranges in Figure 4.2 will therefore serve as an upper limit to the ranges possible for the Antarctic ABCe index.

In an attempt to identify any trends in the production of secondary minerals (particularly OPL), the non-OPL rust component of the "total oxides" end-member was separated from the OPL fraction and included with the unstained silicates fraction (Figure 4.3). This produces the effect of keeping constant the sum of (1) all formerly clear areas, whether stained or unstained, and regardless of the stain intensity, and (2) all less abundant varieties of rust. Hence the non-OPL and unstained silicates categories together represent by definition all components visible in thin section other than OPL and opaques.

In Figure 4.3 the opaque abundances decrease from roughly 19 to 10 percent as the OPL abundances decrease from roughly 26 to 2 percent (excluding the obvious outlier). Meanwhile, a

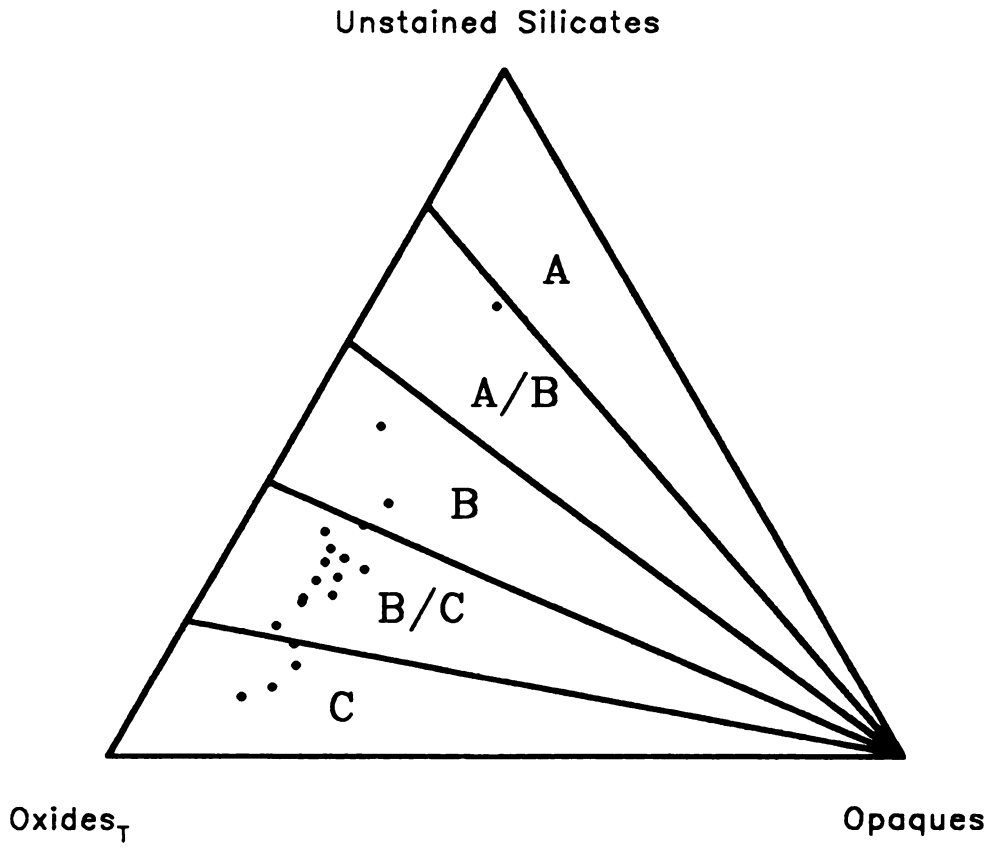


Fig. 4.2. Theoretical distribution of current Antarctic meteorite weathering categories.

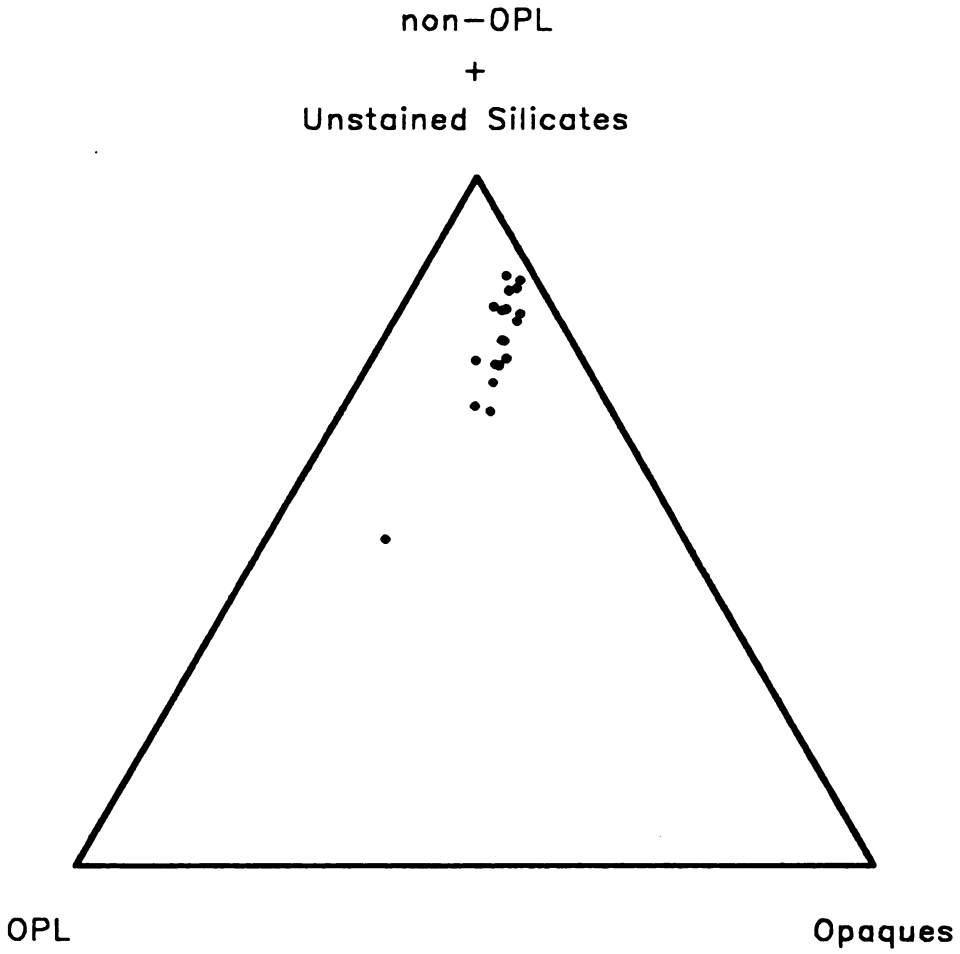


Fig. 4.3. Redistribution of modal analytical data with non−OPL separated from OPL.

corresponding increase from approximately 63 to 86 percent occurs in the unstained and non-OPL fraction. All points originally begin at positions along the ternary boarder perpendicular to the "OPL" end-member as unweathered meteorites. If OPL were replacing opaque material isovolumetrically, each point would be translated from right to left along a horizontal line, ending up on the ternary boarder perpendicular to the "opaques" end-member, and exactly opposite its original position, after all opaque material had been consumed. Having weathered to category C intensities, which we now see are somewhere intermediate between "fresh" and "completely weathered" end-members, the modal data points have somehow become aligned in Figure 4.3.[1]

4.1.2 Negative Loss on Ignition

Figure 4.4 represents a test of the index value reproducibility for negative loss on ignition as an oxidometer, using the two sample analyses performed in November of 1990, and in March of 1992. Perfect reproducibility would yield data points that fall on a line with a 1:1 slope, as indicated in the figure. Only 18 of the 19 samples are represented in this and all following

[1] In actuality, some material opaque in transmitted light will likely remain regardless of the degree of metal and sulfide grain replacement by translucent products because of the presence of primary opaque oxides such as magnetite, ilmenite and chlorite.

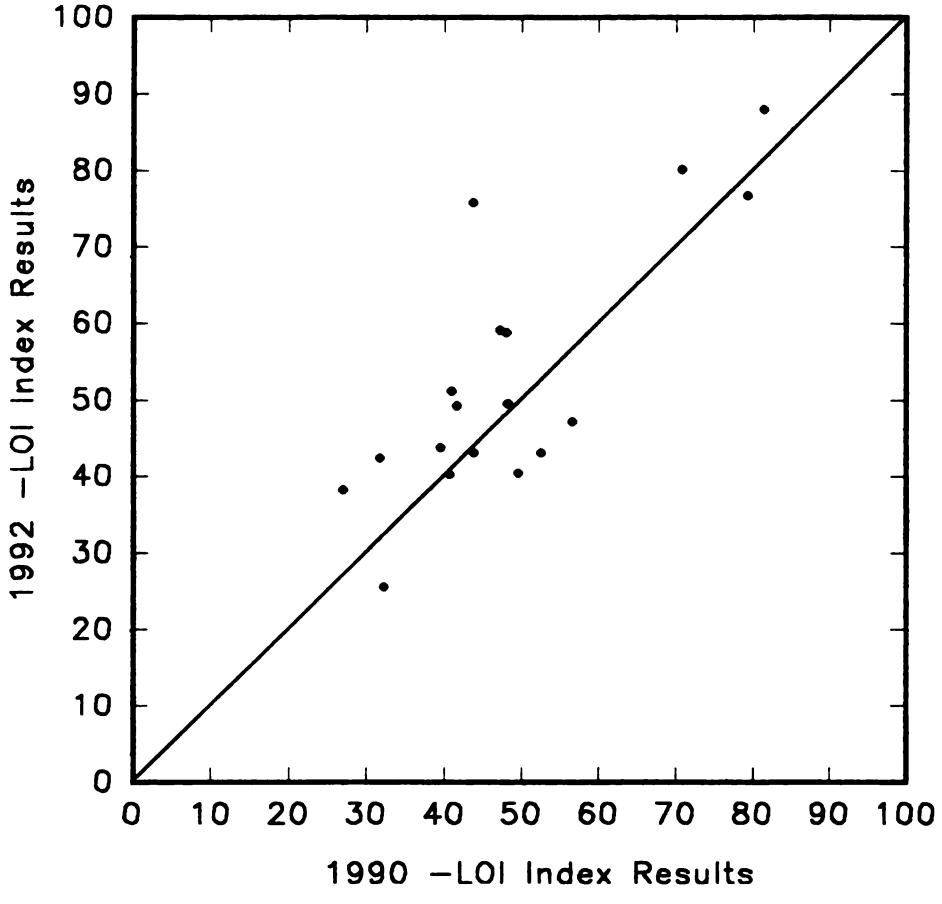


Figure 4.4. Reproducibility of -LOI results.

-LOI charts because the L3 chondrite ALHA81031 underwent a true loss on ignition during both sample runs, and so would not produce a positive value when the -LOI index was calculated (see Tables 3.3a and 3.3b). Notice that most sample points plot near this line, with 13 plotting on or above it. Figure 4.5 is another representation of these data, but with sample-specific taxonomic class and petrologic types indicated. Note that the data can be divided into two dissimilar zones, one centered on the 1:1 line and consisting of H5 and H6 ordinary chondrites, the other forming a somewhat smaller cluster above the 1:1 line, and consisting entirely of L and H4 chondrites. Figure 4.6 shows these data once again, but with the fracture indices represented. Notice that while no continuous trend exists, the least fractured (A category) samples can be easily separated from the most fractured (C category) samples. Notice also that most of the H4 chondrites belong to the C fracture category.

4.1.3 Experimental Oxidometer Contrast and Comparison Diagrams

The NNL stain material tends to occur in fractures and cleavage planes which are thin compared to the thin section thickness. In the modal analysis, volume percentages for total rust, as determined from the point counting of light stains plus denser oxides, are exaggerated by a factor that is inversely proportional to the angle between a given NNL-

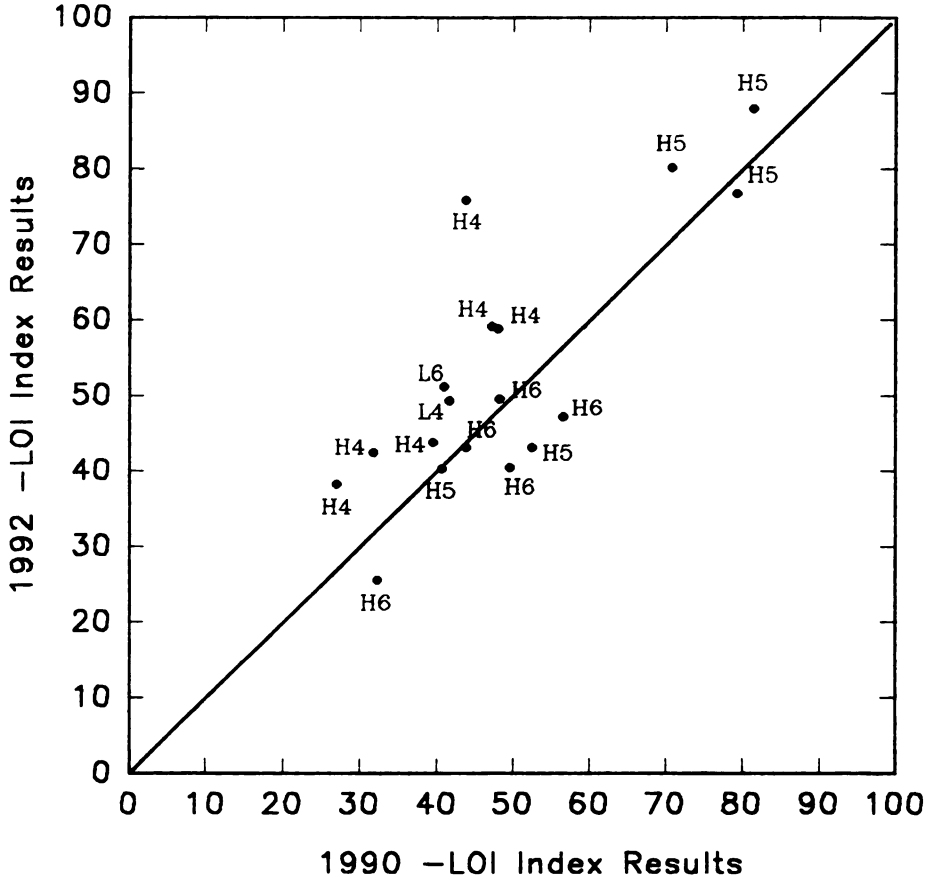


Figure 4.5. Reproducibility graph with meteorite class and petrologic type indicated. Data points can be separated into two groups with L and H4 ordinary chondrites comprising one, and H5 and H6 ordinary chondrites comprising the second.

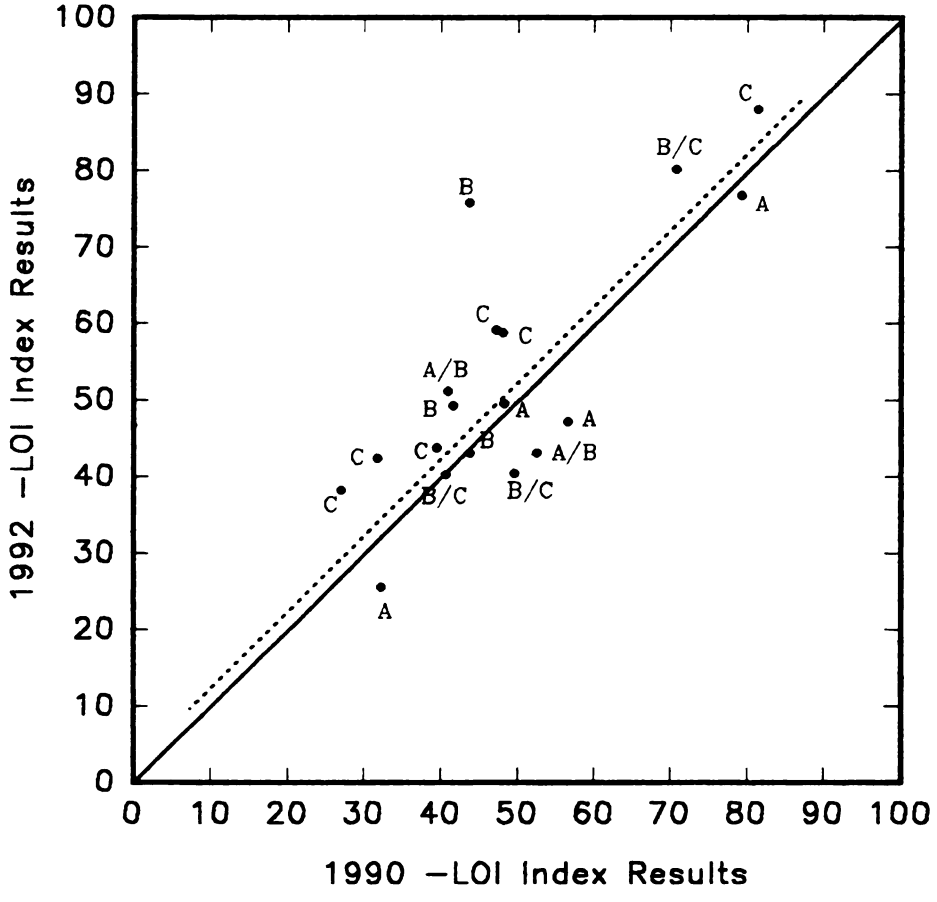


Figure 4.6. Reproducibility graph with fracture index indicated. Note that while no continuous trend exists, a line could be drawn just above the 1:1 line which would separate the least fractured from the most fractured (dashed).

filled fracture plane and the microscope stage (Figure 4.7). The NNL therefore comprises a substantially smaller fraction of total rust than indicated in the modal analysis. For example, ALHA81027,25 has a total count of 78.8 percent for overall rustiness because of extensive light staining. Conversely, LEW85322,9 has a very low total of 18.0 percent because of very little NNL staining. However, these two stones differ less drastically when either their modal or gravimetric index values are compared (Table 4.1).

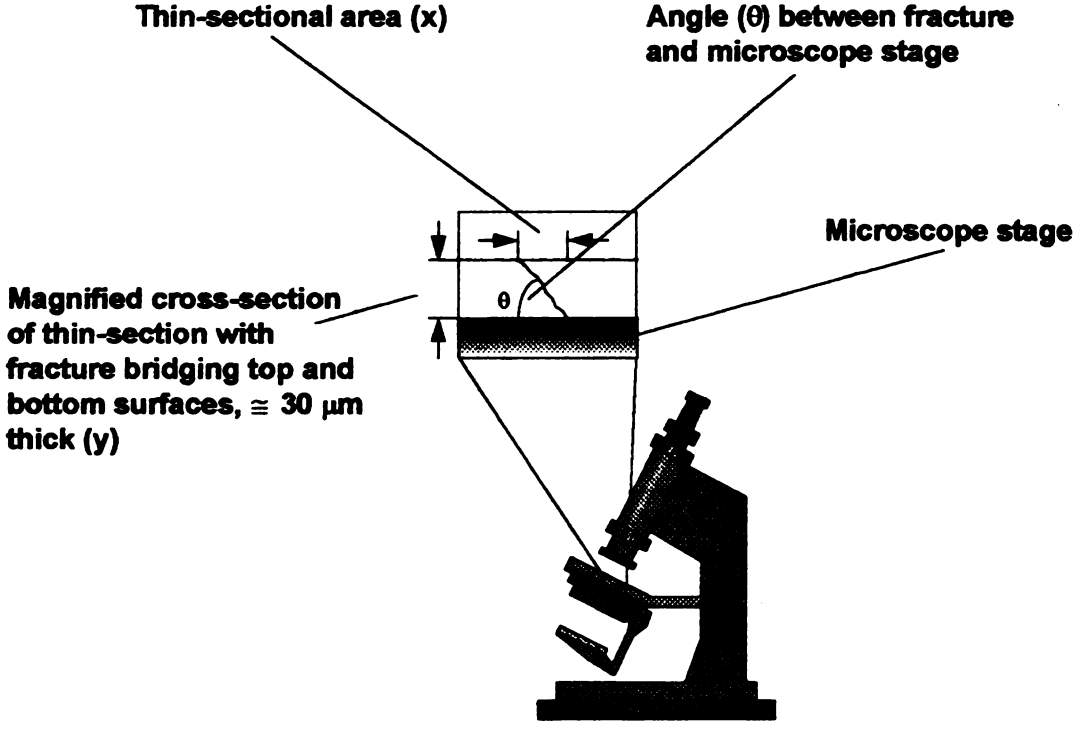


Figure 4.7. Because fractures are much thinner than thin section thicknesses, NNL staining in fractures produces false modal values for this substance according to the geometrical relationship illustrated.

Table 4.1. Summary of sample-specific information

Specimen identification	Group and type	Modal analytical index	-LOI index 1990	-LOI index 1992	Δ -LOI (1992 - 1990)	Recovered sample mass (g)	Fracture index	NASA packaging	Fusion crust in TS
ALHA81031	L3	23.6	NA	NA	NA	1,594	B/C	double ziplock	no
ALHA77230	L4	13.3	41.59	49.31	7.72	2,473	B	single ziplock	yes
ALHA81027	L6	25.3	40.90	51.13	10.23	3,835	A/B	single ziplock	no
ALHA77004	H4	30.2	48.10	58.81	10.71	2,230	C	single ziplock	yes
ALHA77208	H4	39.4	27.02	38.21	11.19	1,733	C	single ziplock	no
ALHA77225	H4	22.2	47.26	59.17	11.91	5,878	C	single ziplock	no
ALHA77226	H4	36.1	39.52	43.81	4.29	15,323	C	single ziplock	yes
ALHA77232	H4	18.5	31.79	42.38	10.59	6,494	C	single ziplock	no
ALHA77233	H4	33.0	43.69	75.83	32.14	4,087	B	double ziplock	no
ALHA77182	H5	71.7	81.43	87.98	6.55	1134	C	single ziplock	no
ALHA79025	H5	32.5	79.29	76.79	-2.50	1,208	A	ss capsule/zl	yes
ALHA79029	H5	38.3	70.83	80.12	9.29	505	B/C	single ziplock	yes
ALHA84075	H5	26.4	40.71	40.24	-0.47	788	B/C	single ziplock	yes
ALHA85025	H5	43.0	52.50	43.10	-9.40	713	A/B	single ziplock	yes
ALHA77271	H6	50.4	32.26	25.60	-6.66	609	A	single ziplock	yes
ALHA77288	H6	41.2	43.81	43.10	-0.71	1,880	B	ss capsule/zl	no
ALHA84082	H6	44.7	48.21	49.52	1.31	556	A	single ziplock	yes
LEW85322*	H6	50.6	56.55	47.14	-9.41	582	A	no ziplock	no
LEW86015	H6	35.6	49.64	40.48	-9.16	780	B/C	single ziplock	yes
Carichic	H6	NA	NA	NA	NA	17,000	NA	NA	NA

zl = ziplock bag
ss = stainless steel
NA = not applicable
TS = thin section

LEW85322 is an H6, 582g	5g bulk *
LEW85323 is an L6, 874g	Smithsonian sample
LEW85332 is a "Chon. (unique)", 114g	Thin section, suspect misidentification; likely -322

The apparent volume would thus be given by,

$$V_a = y\int_0^{FL} x\,dx \propto \frac{1}{\theta}$$

where y is the thin section thickness, x is the thin-sectional area perceived through the microscope objective, and FL is the fracture length. Any oxidometer developed using the NNL point counted values will probably be misleading. The NNL modal fraction will therefore not be included in the index formula used in this study.

The modal oxidometer for this thesis is based on volumetric opaque and OPL abundances. Figure 4.8 introduces the modal index, and is a scatter plot showing the samples as represented by both modal and gravimetric experimental oxidometers. The modal index is defined as the volume percentage fraction of OPL in partly replaced opaque phases. The negative loss on ignition index (abscissa) is the percentage weight gain out of the possible weight gain for a fresh fall of the same group for each meteorite; i.e., corrected for the difference between L and H ordinary chondrites (refer again to Tables 3.3a and 3.3b). Figure 4.8 displays -LOI data for November of 1990 only. Figure 4.9 is a similar graph, but presenting data point positions based on -LOI data obtained in March of 1992. Figure 4.10 shows the two sets of results together, where the 1992 positions are represented by the filled circle, and the 1990

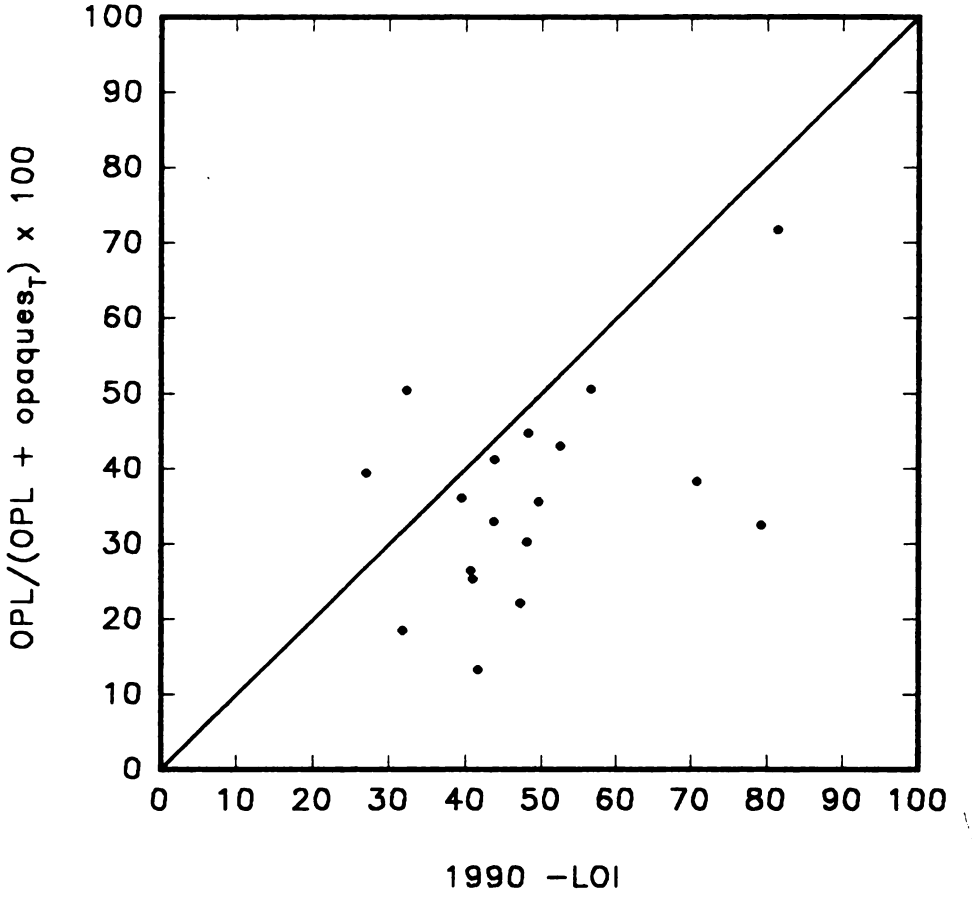


Figure 4.8. 1990 gravimetric and modal index values.

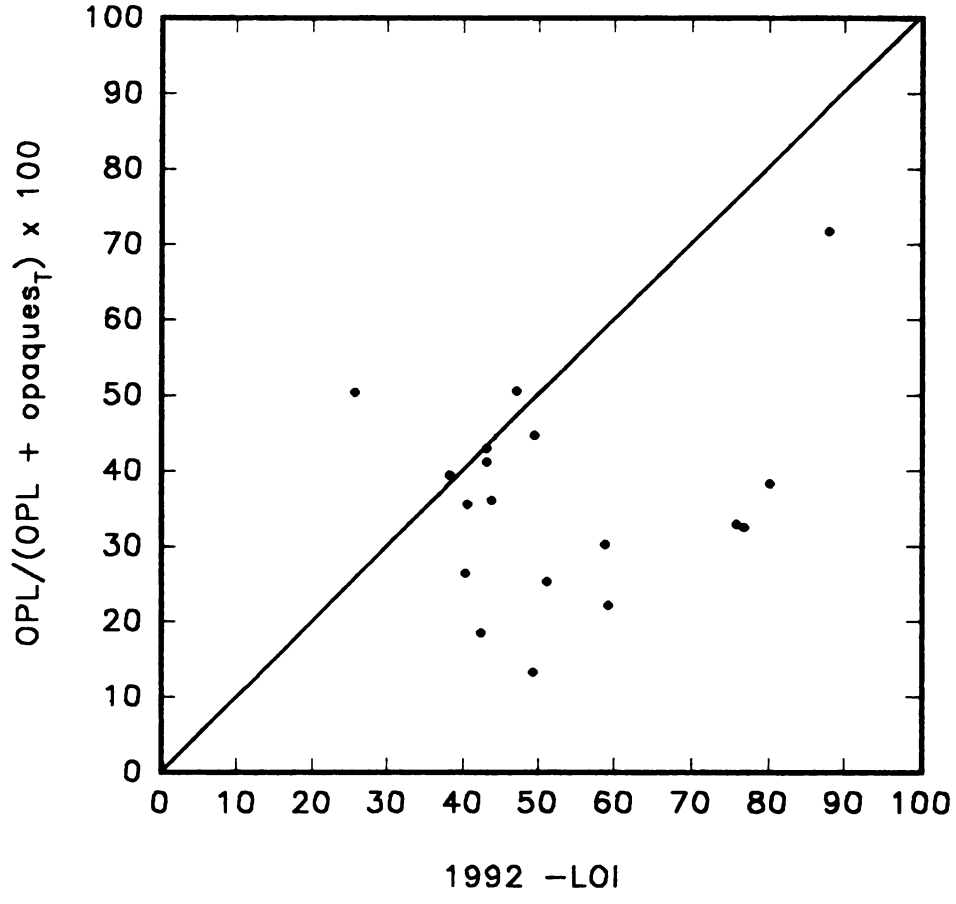


Figure 4.9. 1992 gravimetric and modal index values.

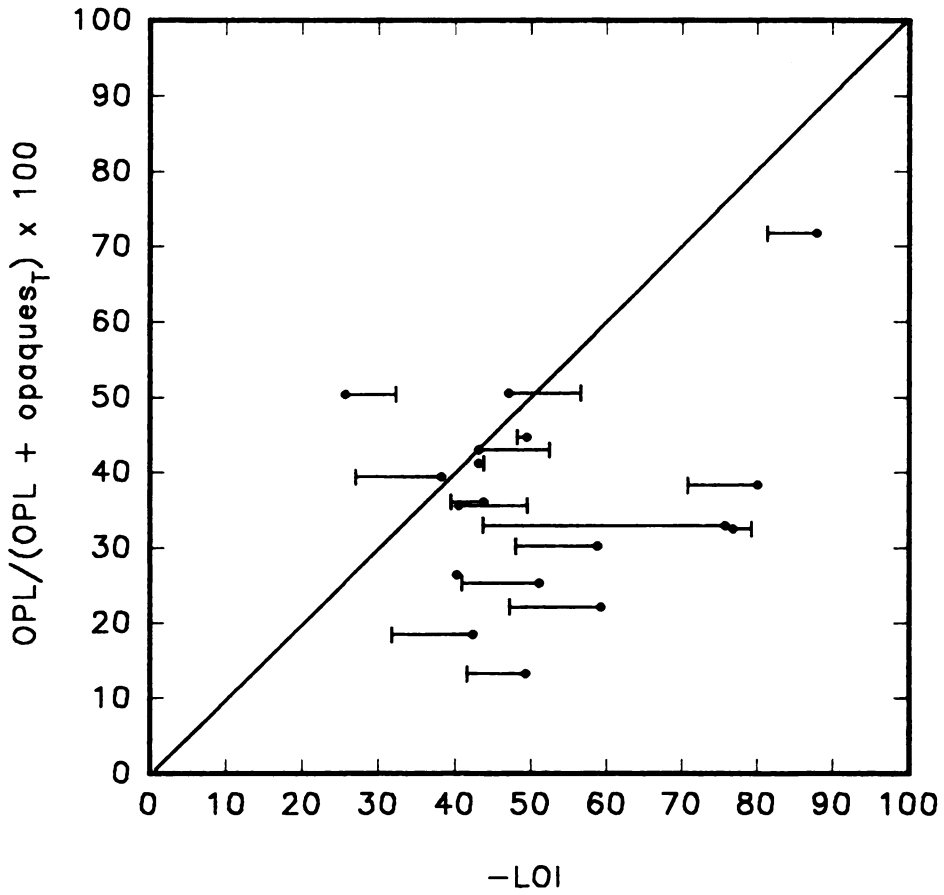


Figure 4.10. Plot representing both 1990 and 1992 −LOI data. 1992 data are depicted as points, 1990 data as vertical lines.

positions are indicated by the short vertical lines. Horizontal lines connecting the two data sets illustrate the direction and magnitude of shifting between the two sample runs. Right lateral shifts have occurred in all but seven samples. Of these seven, two have remained essentially stationary. Five have undertaken significant left lateral shifts.

As with Figure 4.5, the Figure 4.10 scatter plot was examined for patterns in group and petrologic type distribution. Figure 4.11 shows the data points can again be represented by two assemblages with different patterns of behavior. The Ls and H4 meteorites occupy the lower portion of the data point cluster and display substantial and relatively consistent increases (right lateral shifts) in -LOI index values between the two analyses. The H5s and H6 meteorites occupy the upper portion of the cluster and exhibit erratic shifting behavior: some shift to the right, some to the left, and some hardly at all.

4.1.4 Recovered Sample Mass Diagrams

When considering the possible influences on meteorite weathering behavior in the Antarctic environment that could effect the interpretation of oxidometer relationships, it was recognized that some investigation of individual sample mass may be appropriate. Table 4.1 presents the recovered

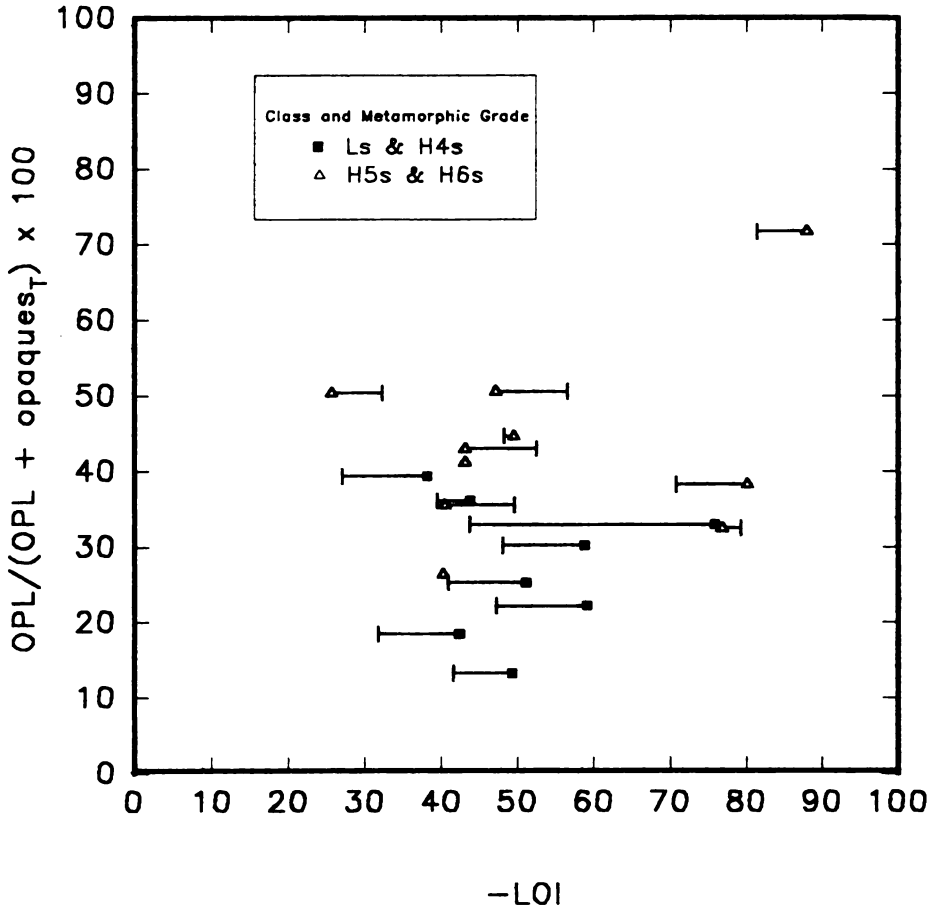


Figure 4.11. Taxonomic group and petrologic type.

mass of each meteorite (data from SCES publication No. 28). Figure 4.12 is a scatter plot of sample mass (abscissa) versus the modal index (ordinate). Notice that smaller samples tend to be (1) more weathered, and (2) more diverse in their weathering intensity, than larger samples. In Figure 4.13, which plots the 1990 negative loss on ignition data against sample mass, we find the -LOI oxidometer reflects a similar "mass versus weathering" relationship, where the most weathered samples are again the least massive samples, and the smallest samples again show the greatest variability in the *y*-axis. However, if we plot the 1992 data for -LOI against the sample mass (Figure 4.14), the scatter widens and is shifted in a positive *x* direction for larger mass specimens.

Figure 4.15 shows the Figure 4.4 graph again, but with the sample points divided into two groups; those with recovered masses greater than (>), and less than (<) the arbitrarily selected value of two kilograms. Note that with the exception of a single point, the two groups are identical to those of Figure 4.5. We can now observe that the H4 chondrites, in addition to being among the most fractured, are also the heaviest chondrites, together with the two L chondrites.

Figure 4.16 is the scatter plot for 1990 data showing, in addition, the individual recovered sample masses in grams.

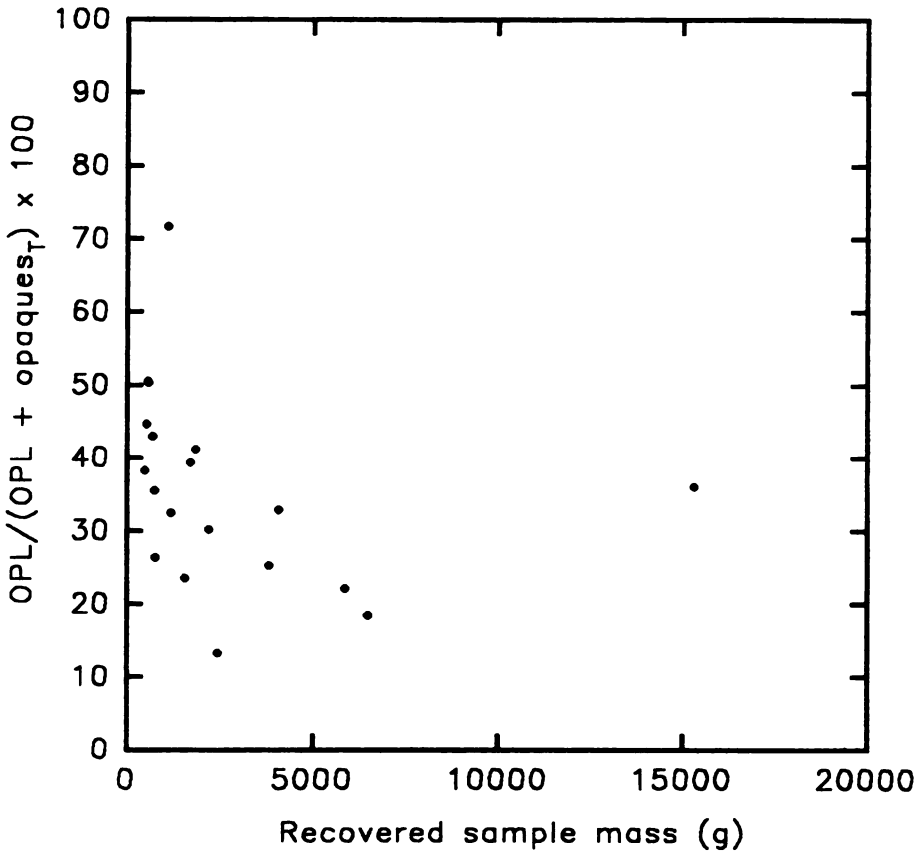


Figure 4.12. Recovered sample mass verses modal index.

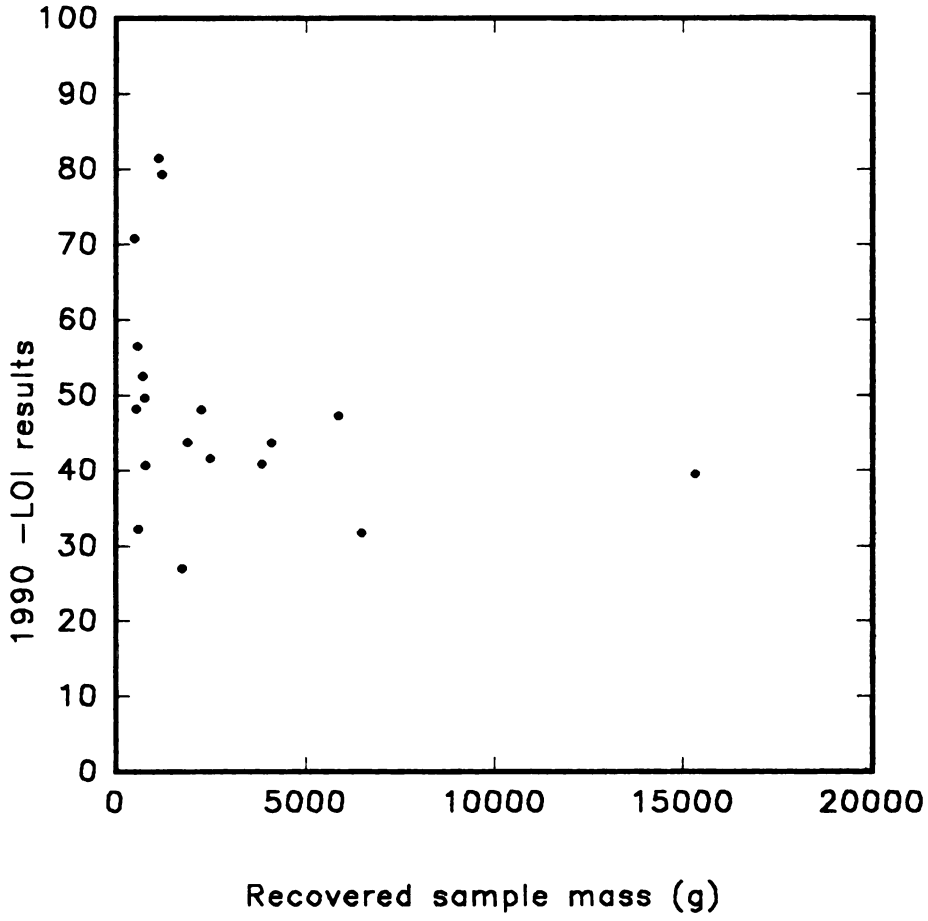


Figure 4.13. Recovered sample mass verses gravimetric index.

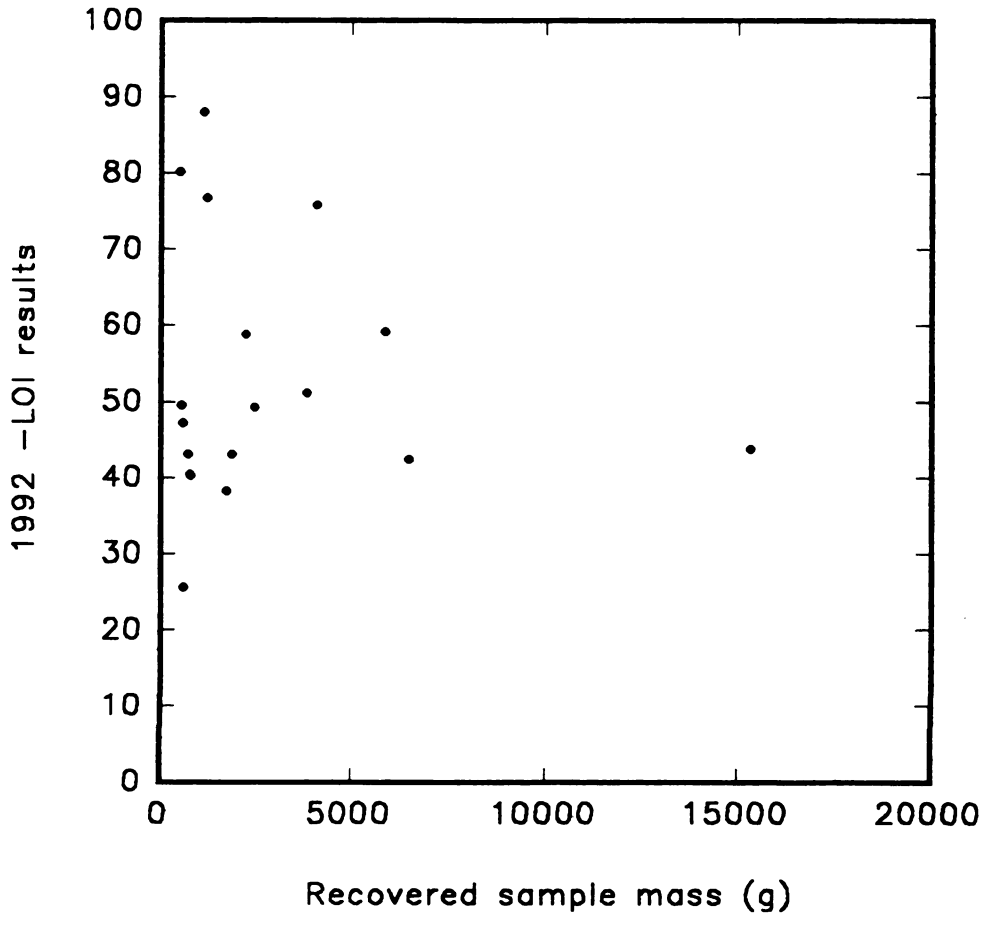


Figure 4.14. Recovered sample mass verses 1992 gravimetric index.

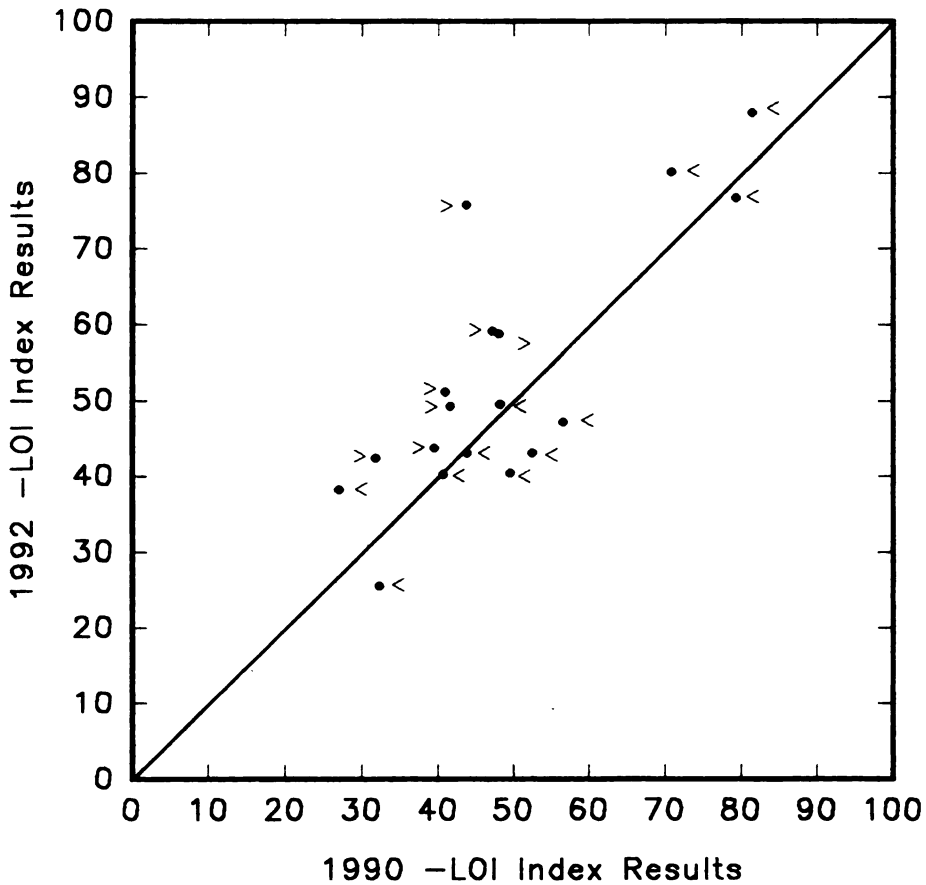


Figure 4.15. Reproducibility graph indicating all samples with a recovered mass in excess of 2 kilograms (>), and those under 2 kilograms (<).

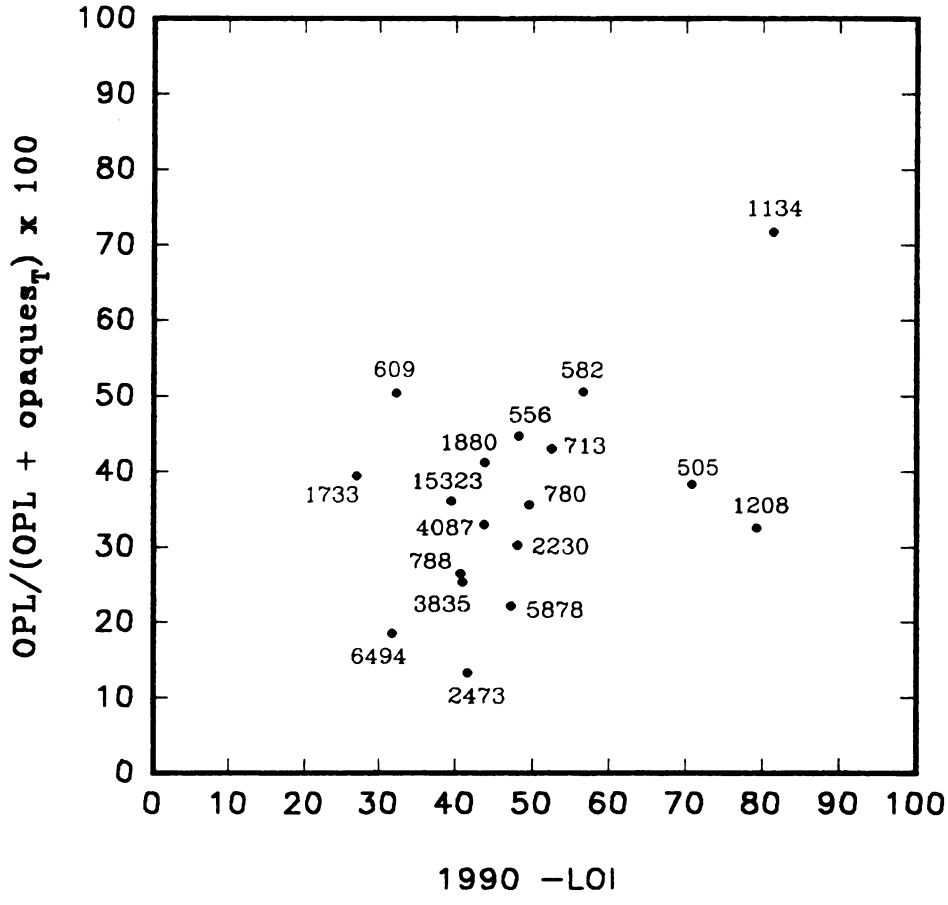


Figure 4.16. 1990 −LOI data points with recovered sample masses indicated in grams.

The samples separate into two vertically overlapping groups (segregated above and below the value of 2 kilograms), represented by the ellipses in Figure 4.17. When the 1992 data are added to the diagram, in the class- and type-specific manner of Figure 4.11, we observe an obvious right lateral shifting and enlarging of the > 2 kilogram ellipse, but very little change in the < 2 kilogram ellipse, Figure 4.18.

This pattern is re-illustrated in Figure 4.19 for which the difference in value between the two sample runs is calculated by,

$$\Delta\text{-LOI} = 1992_{OI} - 1990_{OI}$$

where the OI subscript denotes the use of oxidation index values (as opposed to raw loss on ignition values). Again, while those samples with masses below two kilograms may have positive, negative or very small Δ-LOI values, those above two kilograms all have pronounced positive shifts. Also notice the greater average magnitude of shifts in the positive direction than negative. This difference will be addressed quantitatively in Section 4.2.5.2.

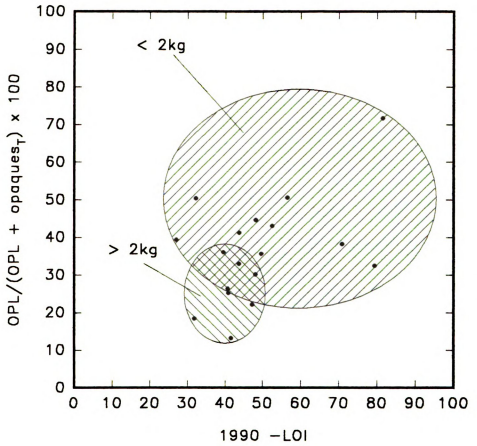


Figure 4.17. Mass distribution of 1990 −LOI data points as determined by 2 kilogram cut−off.

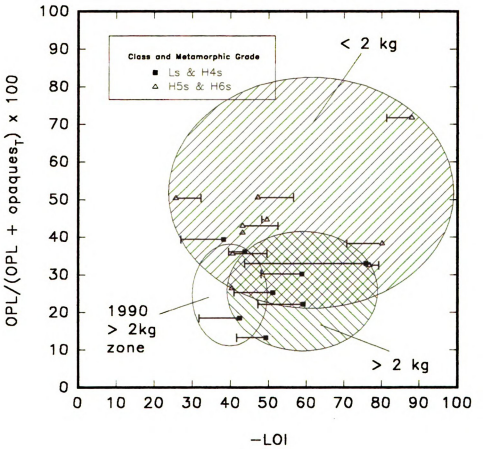


Figure 4.18. Addition of the 1992 −LOI data causes a shifting and expansion of the > 2kg cluster, but produces very little change in the < 2kg cluster due to erratic shifting behavior.

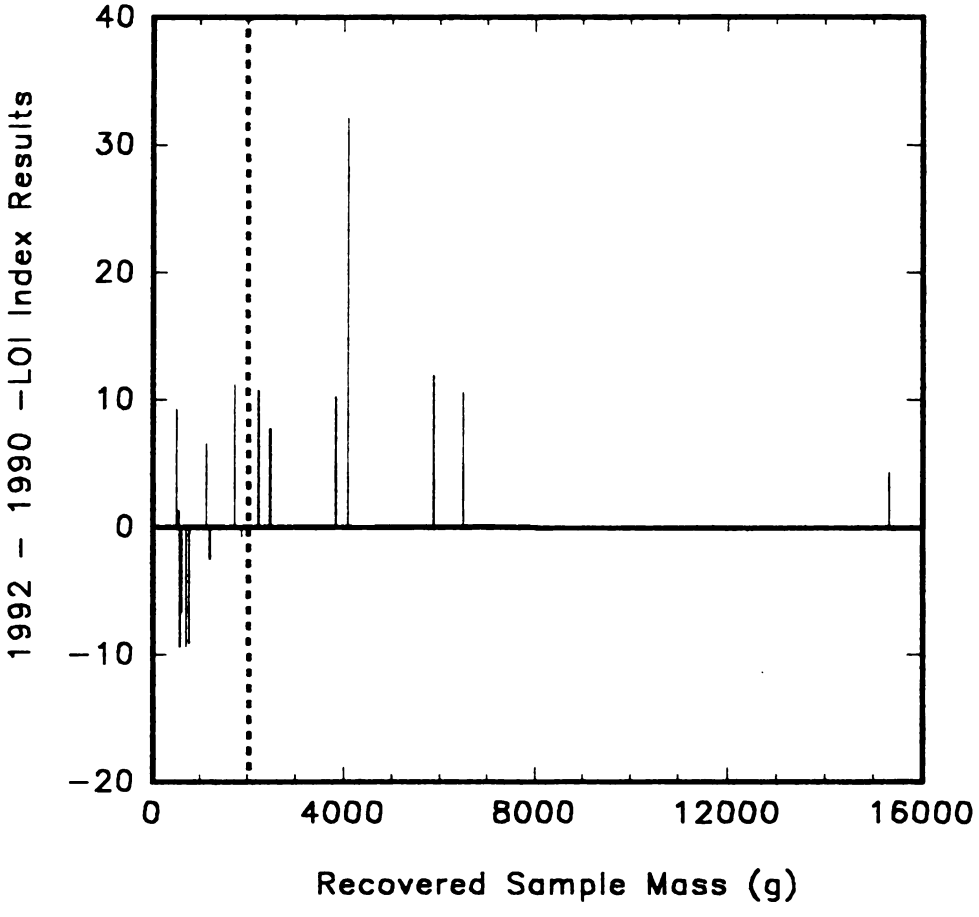


Fig. 4.19. Delta −LOI vectors with recovered sample mass. Dotted line marks 2 kg for reference.

4.2 Interpretation of Data

4.2.1 Secondary Mineral Identification

4.2.1.1 Theoretical Secondary Mineralogy

The formation of iron oxides results when liquid water is in direct contact with reduced iron at non-equilibrium *PTX* conditions, and in an oxidizing atmosphere. Though air temperatures rarely rise above 0°C in Antarctica, contamination of glacial ice by salts can adjust the ice-liquid stability curve and produce liquid water at sub-zero temperatures (Campbell and Claridge, 1987). Also, some zones within the ice sheet may be at the pressure-melting point and can produce liquid water (Sugden and John, 1984). Through experimentation with the non-Antarctic carbonaceous chondrite Allende, Schultz (1986b) determined Antarctic meteorites exposed to solar radiation may have internal temperatures (at depths up to 2.0 cm) rising as high as 5°C, producing liquid water through insulation heating under "normal" *PTX* conditions. This was on wind-free days when air temperatures remain below 0°C. Moreover, the following irreversible reaction, paraphrased from Buchwald and Clarke (1989), represents the formation of akaganéite from kamacite in the solid state within Antarctic chondrites and with

minimal volume change[2], where chloride (molecular chlorine) can be provided by the environment[3].

$$30\underset{\text{kamacite}}{Fe^{\circ}} + 2Ni^{\circ} + 47O + 4H^{+} + 2Cl_2 \xrightarrow[\text{irreversible}]{} 2[Fe_{15}Ni][O_{12}(OH)_{20}]Cl_2(OH) \quad (\underset{\text{akaganéite}}{\ })$$

The authors attribute the apparent ease with which chloride is sequestered to (1) the high ionic mobility of chlorine, (2) the electrochemical nature of the reaction and (3) the size of the chlorine ion. However, under prolonged exposure to these conditions, and with increasing relative humidity and temperature, chlorine ions may remobilize through site exchange with OH^{-} ions. The remaining metastable phase may then decompose to maghemite and goethite according to the irreversible reaction;

$$2[Fe_{15}Ni][\underset{\text{akaganéite}}{O_{12}(OH)_{20}}](OH)_3 \xrightarrow[\text{irreversible}]{} 7\gamma\text{-}\underset{\text{maghemite}}{Fe_2O_3} + NiO + 16\alpha\text{-}\underset{\text{goethite}}{FeOOH} + NiO + 15H_2O$$

The authors admit that the proportions of maghemite and goethite products may vary widely and will not necessarily adhere to the above example.

---

[2] Buchwald (1989) noted "...the structural relationships of the meteoritic minerals are preserved in the initial stages of the corrosion attack," and "...the process may be seen as a replacement process, 'fossilizing' the original structure."

[3] If true, the introduction of open system chlorine should be noted as possibly significant in estimating terrestrial exposure ages for Antarctic meteorites using cosmic-ray-produced ^{36}Cl (e.g., Nishiizumi *et al.* 1989).

Scanning electron microscopy (SEM analysis) was performed on Carichic and three Antarctic samples in an effort to identify secondary oxide minerals. However, this proved unsuccessful due to the paucity of void spaces into which such minerals could grow unconfined by surrounding material (see Section 4.2.2.1; assumption 2).

Also, the oxide mineralogy is difficult to determine in thin section due largely to the fine-grained, cryptocrystalline habit of the few secondary minerals that display birefringence.

4.2.1.2 X-ray diffraction

Carichic

The Carichic diffractograms A, B, C, D, E, O, and P indicate the presence of the expected primary silicate minerals olivine, hypersthene, and plagioclase, as well as goethite and possibly akaganéite and maghemite. The diagnostic 4.18 Å goethite peak can be found in all but diffractogram P, in addition to other goethite peaks. Three akaganéite peaks can be found in both diffractograms D and E, which were run following citrate dithionite chelation treatment. The akaganéite peaks are well defined and separated from other

peaks. The largest peak of diffractograms D and E is an unknown at 3.11 Å. This peak is anomalous and probably represents a synthetic precipitation, possibly jarosite ($KFe_3(SO_4)_2(OH)_6$), produced as a result of the citrate dithionite process. A weak peak at 5.10 Å in diffractogram D is consistent with the presence of jarosite. Maghemite peaks are present in diffractogram A, C, D, and P at approximately 2.089 Å. Evidence for the primary iron-titanium oxide ilmenite is present in diffractogram C with peaks at 3.73 Å, 2.76 Å and 2.25 Å.

ALHA84075,7

Diffractograms F, G and H were produced for ALHA84075,7. Plagioclase, olivine, and hypersthene were, of course, identified in each diffractogram as primary silicates. Most diagnostic peaks for lepidocrocite (2.76 Å and 1.495 Å) overlap olivine peaks, and at similar relative intensities, so it is impossible to say with certainty that lepidocrocite is present. There is a peak at 6.33 Å that could be lepidocrocite, but it is very weak. Also, this peak could be the 6.35 Å maghemite peak. Other possible lepidocrocite peaks are weak but discernible, but the most intense candidates are probably olivine reflections.

As most maghemite peaks could be confused with olivine, magnetite or ilmenite, including the most intense (100 percent) peak, the peak considered to be most diagnostic for maghemite is the 2.089 Å peak, which was found in all three diffractograms. The 1.474 Å maghemite peak is absent.

Five possible goethite peaks are visible in diffractogram F. Diffractogram H is very rough and the peaks have low amplitudes due to the fine particle size of the oriented powder mount. Many peaks are difficult to distinguish from the background. The primary silicate peaks in diffractogram G are well pronounced.

ALHA77271,27

Diffractograms I, J, K, and L were run for ALHA77271,27. Too much noise exists in diffractogram K for the positive detection of any oxides. However the 4.17-4.18 Å goethite peak is present in each of the remaining three, and there are suggestions of lepidocrocite in diffractogram I, but again, these would be difficult to differentiate from those of olivine. Primary phases identified include olivine, plagioclase and hypersthene. High background noise coupled with the small size fraction results in few and indistinct peaks in diffractogram L.

ALHA77182,21

Only two diffractograms, M and N, yielded usable patterns for sample ALHA77182,21. Peak intensities are low in diffractogram M, due to the 2K CPS setting. The 2.086 Å maghemite peak is present. The 7.30 Å and 5.26 Å akaganéite peaks rise just above background, as does the 4.18 Å goethite peak. Diffractogram N is only slightly better and includes a peak at 7.31 Å that seems to represent the leveling of the background noise more than the reflection of X-rays. This may also be the case for the 7.30 Å peak in diffractogram M. The 4.17 Å and 1.720 Å goethite peaks are sharp and easily distinguished from the background, The 2.083 Å maghemite peak is also easily discernible.

On the basis of the theoretical evidence together with the XRD data, it is proposed the secondary oxide mineralogy of the study samples consists primarily of goethite, with possible lesser amounts of maghemite, akaganéite and/or lepidocrocite.

4.2.2 Modal Analysis Ternary Diagrams and the OPL-based Index

4.2.2.1 Assumptions

Two OPL-specific assumptions and one NNL-specific assumption are made regarding the interpretation of modal analytical results:

(1) It is assumed that the majority of OPL is *in-situ* altered opaque material. This is based on the observation that OPL is almost invariably found in intimate association with opaque phases, and fills what appear petrographically to be former opaque boundary outlines. OPL apparently forms from constituents less mobile than those forming NNL and other rusts, suggesting that it forms pseudomorphically after metal and perhaps sulfide grains.

(2) In considering the pseudomorphic replacement of opaque phases, it is also assumed that no significant volume change has occurred during OPL production, meaning the volume ratio of product to reactant (V_{prod}/V_{react}) is close to unity. This assumption of isovolumetric replacement follows from the general lack of void spaces into which secondary minerals may grow. Ordinary chondrites are dense rocks with few pre-terrestrial void spaces, although some shock-process-formed vugs exist (Olsen, 1981). A few small vugs (or "plucked zones" possibly formed during mounting operations) have been

found petrographically among the subject samples. These zones have become partially filled in many cases with BVF material (refer to Section 3.1), indicating that some net volume increase is taking place (Figure 3.15); but these are not common, and have not been found in all specimens. It was this lack of abundant pore space that rendered the SEM analysis ineffective in detecting identifiable secondary minerals (Section 4.2.1.1).

With little or no void space for OPL products to grow into, and in the absence of any wholesale, volume-reducing silicate weathering, for which there is yet no direct evidence, OPL replacement of reduced metal primary phases is probably isovolumetric. Non-isovolumetric metal alteration could occur only if fractures were enlarged, or new fractures created to expose unweathered surfaces to the environment. The work of Buchwald and Clarke (1989), focusing on akaganéite production in Antarctic ordinary chondrites, suggested that replacement of kamacite with this mineral occurred isovolumetrically.

(3) NNL stain is negligible. Extensive staining on terrestrial Antarctic rocks gives them "...a rich brown color and makes [sic] them appear considerably more weathered than they actually are [sic]," (Campbell and Claridge, 1987). NNL stains are essentially two-dimensional, and should not contribute significantly to the

volume of secondary products produced (see Section 4.1.3). It is quite possible that greater or lesser amounts of NNL stain or "varnish" are responsible for inappropriate estimations of Antarctic meteorite weathering intensities.

4.2.2.2 ABCe Index Inadequacies

If it is allowed that oxide material visible in thin section (modal abundance values) is identical in extent to that observed in hand specimen (ABC designation), then the inadequacy of the ABCe oxidometer is evident in Figures 4.1 and 4.2. Ideally, all meteorites stained to C intensities should plot within (or close to) the lower fifth region indicated in Figure 4.2, and they fail to do so. In all probability, however, the total oxide values represented in the modal analysis are somewhat higher than those observable in hand specimen because of enhancement of limonite features in transmitted light under magnification (versus reflected light in hand specimen). Hence, a corresponding shift toward the "unstained" end-member in the ternary diagram is probably appropriate when comparing these data to the ABCe system. Such a shift would produce a still greater number of data points to be found in "non-C" regions of the diagram, rendering the ABCe system even less suitable as an indicator of weathering intensities, unless one wished to increase the number of categories (e.g., extend ABC to include D, E and F and redistribute accordingly).

4.2.2.3 Residual Metal Grains and Pressure Equilibrium

While some variability in opaque components is present, no trend in the destruction of opaque material is obvious in Figures 4.1 and 4.2. Indeed, the linear pattern appears to be nearly perpendicular to the opaque end-member. One may infer that original opaque abundances have not been significantly lessened by alteration. It would therefore appear that only a minor volume of reduced metal is required to produce copious amounts of NNL stain. This may also indicate that weathering intensity (as represented by iron oxidation) is as much or more a function of the availability of liquid water and the mobility of iron, within a given volume of rock, than of actual exposure duration to weathering conditions. If residence time were an important oxidation factor, then one might expect to see a greater range in residual metal grain abundances (even among samples of a common weathering category), the stones having been exposed individually to terrestrial weathering conditions for lengths of time that may differ by several orders of magnitude (2 [±1] x 10^3 to 950 [±100] x 10^3 y.b.p. for Allan Hills (Nishiizumi *et al.*, 1989))[4]. More significantly, the persistence of metal grains within highly weathered ordinary

[4]This assumes that weathering continues for meteorites entrained within the ice sheet as well as for those at the ice surface, which has not yet been substantiated. It could well be that weathering reactions take place only while the stone is exposed to the atmosphere and sunlight. If the latter is true, and an assumption can be made that residence times near the ice surface are of comparable length (at least much less than total terrestrial ages) for all Antarctic meteorites, then exposure to weathering conditions would be comparable.

chondrites may indicate a metastable cessation of the oxidation process prior to complete destruction of the parent material. As will be explained in the following sections, this latter hypothesis is supported by modal data and observations of the Carichic meteorite, and is consistent with interpretations of negative loss on ignition data.

In Figure 4.3, each meteorite has left its origin on the ternary boarder perpendicular to the "OPL" end-member and migrated some distance toward the 100 percent-weathered boarder (perpendicular to the "opaques" end-member). A linear pattern has resulted which, if north is toward the top of the page, runs NNE to SSW. The possible data point migration scenarios on the Figure 4.3 ternary plot will now be examined to arrive at the most likely interpretation of this linear pattern.

Figure 4.20 summarizes the four feasible components of movement, where each arrow represents a direction of migration, for data points within the context of this analysis. Arrow A indicates the limit in left- to right-hand movement. No data point can cross, from left to right, a line that parallels arrow A because to do so would mean that reduced metal abundances had increased; an impossibility. Arrow B represents the case where opaque minerals alter pseudomorphically to OPL products with zero

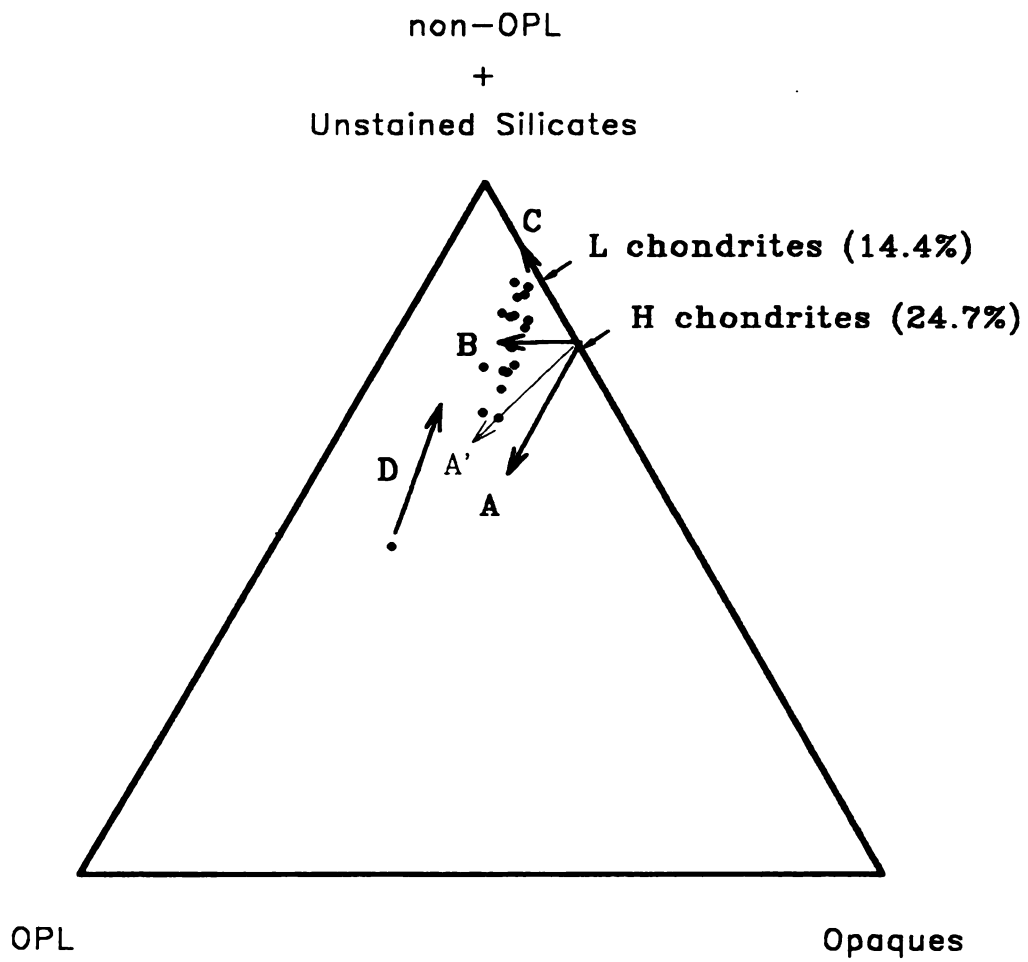


Figure 4.20. Possible scenarios of movement for data points on Figure 4.3. Positions for average opaque modal abundances are indicated for unweathered L and H chondrites (data from Dodd, 1981).

volume change. Any NNL stain produced during this process is not represented on the graph due to its absorption within the "non-OPL + unstained silicates" category, which remains constant. Arrow C represents alteration directly to non-OPL rusts, and arrow D suggests the possibility that OPL products may themselves be unstable and weather to non-OPL limonites. Obviously, OPL values must first increase before they can hypothetically decrease by such a tertiary alteration.

The linear data point trend in Figures 4.3 and 4.20 is not parallel to any ternary boarder, and therefore cannot be attributed to a simple variability in any single pair of components. Given that crossing a line parallel to Arrow A in Figure 4.20 is prohibited, the linearity also cannot indicate a preferred weathering pattern in a direction from near the "non-OPL + unstained silicates" end-member downward toward the ternary boarder perpendicular to the "non-OPL plus unstained silicates" end-member (NNE to SSW direction). Neither is it likely that the samples have moved along the trend in the opposite direction, imitating an "arrow D" route; no petrographic evidence was found to suggest that OPL has been altering to other types of rust. The most likely path of migration for each data point is along a line intermediate between arrows A and B (A') because of OPL expansion near rock surfaces and fractures (refer to Figures 3.8, 3.9, 3.10, and 3.11 for some examples). Such an "A'"

path is supported by the petrographic evidence given on the replacement of opaque minerals with OPL product (Section 3.1), and could represent a dilatation of the rock as a whole. Thus, on a ternary diagram, where volume is conservative, an "A'" path is the projection onto two dimensions of a three-dimensional tetrahedron where the fourth end-member is "volume change". Hence, apparent opaque volumes may be represented in a ternary diagram such as Figure 4.20 at less than their original value based on dilatation alone. Such a factor becomes important in the remaining discussion of this Section.

Empirically determined modal abundances of opaque minerals in non-Antarctic H and L ordinary chondrites have been gathered from the literature and are given in Table 3.2. The numbers are comparable, though slightly lower in some cases, to the point counted sum totals of OPL and opaque grain abundances in this modal analysis (refer to Table 3.1). Values from Dodd, 1981 for average modal abundances of opaques in L and H ordinary chondrites are indicated in both Table 3.2 and Figure 4.20. The fact of slightly larger "OPL plus opaques" values is again attributable to the expansion of product near rock surfaces or fractures.

It must be emphasized that general patterns based on volume percentages and reflected by ternary diagrams do not differentiate chemical alteration processes, but reflect

only the summations of static features recognizable in thin section. However, by effectively isolating the reactant (opaques) and product (OPL) minerals of an alteration sequence, some clues on the behavior of OPL reactions might be detectable. With this in mind, it is felt the trend in Figure 4.3 may indicate a temporary state of pressure equilibrium for OPL production in the Antarctic environment. The diagonal linear pattern seems to represent a zone of stabilization beyond which the meteorites have not progressed, and the positions along which seems to be determined by each meteorite's initial opaque mineral abundance; that is, the greater the original opaque mineral abundance, the greater the OPL mineral abundance. A direct relationship between metal abundances and OPL abundances is predicted by the observation that (1) a greater surface area for metal exists in meteorites for which there is a higher initial modal abundance of this material, and provided that (2) OPL replacement occurs to similar depths for similar time intervals within individual metal grains in different stones.

Table 4.2 is a look at mineral volume changes based on published unit cell dimensions, and with the assumption that kamacite and taenite are pure iron minerals and not iron-nickel alloys. One can see that for goethite, the most likely common secondary product based on XRD results (Section 4.2.1.2), the volume increase is more than three

Table 4.2. Calculation of primary and secondary mineral volume percent differences

Mineral crystal system	Unit cell axial dimensions (Å) a	b	c	Z	Unit cell volume (Å³)	Unit cell volume (m^3)	No. of unit cells in one mol UC(m^3) x 6.023E23/Z	V_{prod}/V_{react} after 100 percent oxidation*
Kamacite (iso)	2.86	2.86	2.86	2	23.394	2.33940E-29	7.0451E-06	Kamacite » goethite: 3.027
Taenite (iso)	3.56	3.56	3.56	4	45.118	4.51180E-29	6.79364E-06	Taenite » goethite: 3.139
Goethite (orth)	4.65	10.02	3.04	4	141.642	1.41642E-28	2.13277E-05	NA
Hematite (hex)	5.04	5.04	13.76	6	349.526	3.49526E-28	3.50866E-05	Kamacite » hematite: 4.980

* Increase is upper limit, based on hypothetical pure iron primary phase
NA = not applicable
UC = unit cell
Kamacite » goethite = weathering reaction from primary to secondary mineral

fold, and even greater for some other possible secondary minerals. It would appear that the growth of goethite at the expense of reduced metal phases must eventually exert a pressure on the surrounding groundmass, possibly forcing iron oxide-bearing fluids into all available fractures, cleavage planes and grain interstices, being thus responsible for the pervasive nature of the NNL staining. Clearly at some point, either (1) the rock must break, similar to periglacial frost wedging (Grawe, 1936), or (2) the growth process ceases. The linear pattern in Figure 4.3 could therefore represent a state of pressure equilibrium within each meteorite interior where the growth stress of the growing minerals are in balance with the tensile strength of the rock itself. This metastable state of affairs is adjusted each time the meteorite is broken until a state of equilibrium can be reestablished.

The bulk samples and thin sections chosen and prepared by NASA curatorial staff arrived in Michigan as largely unbroken single chips and sections, respectively. This is not surprising, given that some measure of hardness would be a natural prerequisite to the sectionability of samples, causing the sample suite to be somewhat biased in favor of moderate to high rock strength thin sections. Highly friable zones within a requested meteorite would be bypassed by NASA curatorial staff during sample preparation in favor of stronger lithic fragments, thereby ensuring that only

rock volumes likely to have been predisposed to sustainable pressure equilibrium conditions will be represented in Figure 4.3. More friable portions of rock may, however, have been included within the 5.0 gram bulk chip sample suite, and may have theoretically weathered further toward the ternary boarder perpendicular to the "opaques" end-member of the diagram, where no modal data are found.

4.2.3 Negative Loss on Ignition and the -LOI Index

The -LOI weathering index involves the measuring of a weight difference, which theoretically accounts for all secondary oxides produced by weathering. However, the presence of bound water and hydroxyl ions in the pre-ignited specimen can have a marked influence on this difference (Jarosewich, 1993). The L3 chondrite ALHA81031 apparently underwent a true loss on ignition, presumably due to the volatilization of bound water within its unequilibrated matrix. More equilibrated chondrites have less bound water, but uncontrolled amounts of moisture, bound or unbound, may still conceivably pose a problem for the use of -LOI as a weathering index. It is hoped that by cooking the samples at 110°C before ignition, any unbound water was volatilized and driven from the system.

The measure of -LOI data reproducibility from one sample volume to another within a given meteorite specimen is

indicated by the combined index value trend in Figure 4.4. The agreement of the data point trend with the 1:1 line is good, suggesting that -LOI may yet be considered as an alternative to the ABCe classification system for the oxidation intensity of equilibrated ordinary chondrites. This is also indicated in Figure 4.19, which shows that 1992-1990 reproducibility is within 10 percent for all but one of the samples. However, in the absence of more qualitative information on the nature of the reactions and the pre-ignition chemistry (bound water and other volatile and semi-volatile parameters) within individual meteorites, it is difficult to say whether the oxidometer behaves precisely as theory would predict. If we use the same criteria for assigning the five ranges in weathering intensity as was used in Figure 4.2 (0-20, 20-40, etceteras), then again it can be seen the values extend outside the zone of a single category. Notice that most of the data points cluster within a midrange section where one should expect to find A/B and B weathering category stones. It would be worthwhile to pursue further the possibilities of -LOI using a greater number of samples and with samples of other weathering categories.

4.2.4 Experimental Oxidometer Contrast and Comparison

Figure 4.10 plots the two experimental oxidometer values mutually. If both indices accurately represent a uniform

metal alteration, the points would align along a 1:1 line. No such relationship exists in the Figure. Ordinate deviations from the 1:1 line may be due to one or more of the following possibilities: (1) Greater weathering of bulk chips than of sealed thin sections while in storage; (2) Modal analytical measurement inaccuracies (see Section 2.1.1 for technical difficulties inherent in the point counting process); (3) Non-represented sample-specific variations in opaque chemical and mineralogical compositions; (4) Variations in pre-terrestrial modal abundances of metal. The weight taken on during oxidation of reduced metal phases should be proportional to the total relative abundances of these phases in each meteorite sample. However, the pre-terrestrial total amounts of metal is not known on a per sample basis, but is rather assumed from published averages for ordinary chondrites based on Yates (1988). (5) Iron oxide heterogeneity. Adherence to the 1:1 generality depends on how representative each chip is of the overall rustiness of its respective meteorite. As an aid to evaluating this likelihood, samples that possess fusion crusts are identified in Table 4.1. The presence of a fusion crust identifies the sample as having been cut from the surface of the meteorite and allows the assessment of its being representative, or simply part of a hypothetical weathering rind. It is not known which of the bulk samples have fusion crusts. No patterns were found which could

relate the occurrence of fusion crusts in thin section to any trends identified in the data analysis.

By the observation that most data points lie below the 1:1 line in Figure 4.9, in all likelihood the assumption of non-OPL rust abundances being totally negligible for the purpose of establishing an index is in error (assumption number 3 of Section 4.2.2.1), and the ordinate values have been underestimated by a factor proportional to individual non-OPL rust abundances. Identifying a means to correct for this discrepancy might raise each point an appropriate distance closer to the 1:1 line. This is an area for further study, for it could help to establish the reliability of the -LOI experimental index. Possibility number 1 of this Section, that of differential weathering of the bulk samples in storage, is also a likelihood, and will be further addressed in the Section on curatorial weathering (Section 4.2.5.2).

4.2.5 Non-index-related Anomalies

Beyond the question of oxidation indices, additional patterns can be recognized in Figure 4.4 and other figures that may lend some insight into other aspects of Antarctic meteorite weathering. That most of the data points in Figure 4.4 lie above the 1:1 line may be significant. Also,

Figures 4.5, 4.11, 4.17, and 4.18 show how the points can be separated into two non-overlapping groups based on taxonomic class, petrologic type and recovered sample mass. Moreover, Figure 4.6 illustrates that extremes in macro scale (trans-specimen) fracture density are well separated among the data point positions. It is the intent of the following discussions to show that these patterns are the results of a complex set of circumstances and processes, some of which are perhaps unique to the Antarctic environment, that involve the simultaneous interplay of the following four factors at a minimum: (1) the fracture-induced metal alteration heterogeneity effect (FIMAHE), (2) macro scale fracture density, (3) recovered sample mass (as an indication of size and therefore surface area), or class and petrologic type, or both, and (4) curatorial weathering. Each of these factors is discussed below.

4.2.5.1 Carichic, Fractures and the FIMAHE

The Carichic thin sections suggest that, while dark oxide staining is ubiquitous throughout the specimen, the locations of residual metal grains are tightly constrained by the location of fractures (refer to Figure 3.21), rendering an aspect of metal grain heterogeneity to the meteorite. Wright and Grady stated in 1989 the "—it is probable that fracturing takes place along pre-existing cracks, which may have been inundated with terrestrial

fluids." The following pictorial series proposes an alteration sequence based on the observations of the Carichic thin sections in reflected light. This sequence demonstrates how two samples from different locations within highly weathered meteorite interiors can yield different oxidometer values, and are more likely to do so, all other factors being equal, than two samples from within a less weathered specimen. This counterintuitive situation of increased sample heterogeneity with increased weathering intensity will be referred to as the fracture-induced metal alteration heterogeneity effect (FIMAHE). Magnification is approximately 15x in each of these figures.

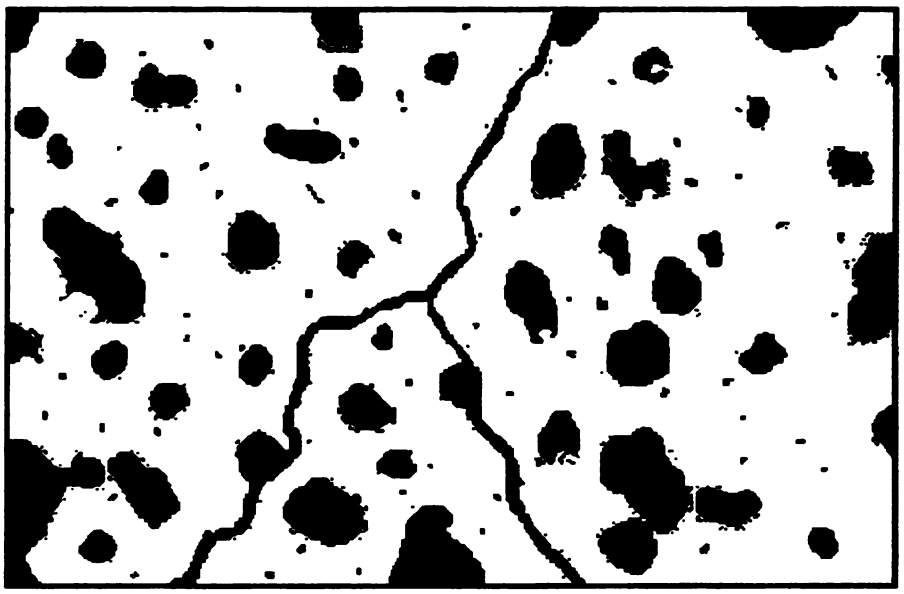


Figure 4.21. Representation of an unweathered "fresh" ordinary chondrite sample in thin section. Metal grains (black blebs) stand out in contrast to surrounding matrix, chondrules and crystal grains (represented together by the white background). A branching fracture (black line) transects the sample.

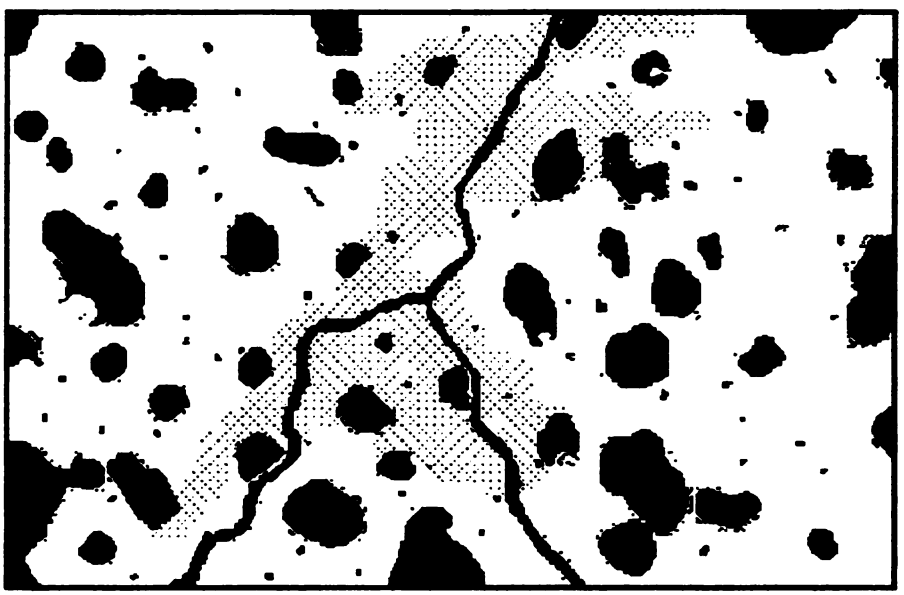


Figure 4.22. Initial stage. Incipient pseudomorphic alteration has occurred where the fracture encounters metal grains directly (white contact zones along fractures), and in other locations close to fractures. Some light staining has occurred (stippled pattern).

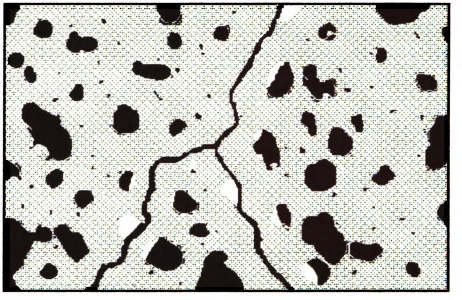


Figure 4.23. Intermediate stage. Widespread staining has occurred. Pseudomorphic alteration of metal grains (white) is most pronounced near the fractures. Most weathering category C Antarctic meteorites are probably at this stage.

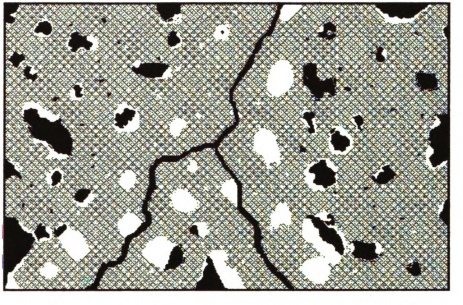
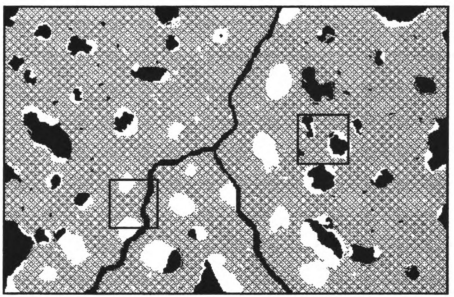


Figure 4.24. The Carichic sample (advanced stage). The sample is highly altered. Extensive dark staining throughout the specimen accompanies complete replacement of metal grains close to fractures. Moderate degrees of alteration can be found away from fractures, leaving OPL haloes surrounding relict metal grains.

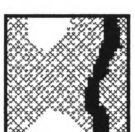
If pressure equilibration does occur for secondary oxides within weathered ordinary chondrites, it could account for the persistence of heterogeneity within Carichic, and

presumably, other ordinary chondrites. Those zones closest to fractures would weather more intensely and more rapidly than zones further removed, since they are closer to (1) available water, and (2) void spaces into which the expanding secondary products can grow. However, this increase in growth would eventually stabilize as the differential forces between the growing oxide and the surrounding rock become equal, thereby maintaining heterogeneity.





High gain on ignition
Low -LOI index value
Low modal index value



Low gain on ignition
High -LOI index value
High modal index value

Figure 4.25. Example of the fracture-induced metal alteration heterogeneity effect or FIMAHE, whereby different oxidometer values are obtained depending on where within the meteorite the sample is taken.

Theoretically, the intensity of the FIMAHE would be controlled in general by (1) the surface area exposed to weathering agents, and (2) the macro scale fracture density within a given volume of rock. Fractures permit the

migration of fluids to meteorite interiors. A greater fracture density would increase homogeneity and decrease the FIMAHE. Conceivably, samples that satisfy specific criteria for various ranges in fracture density might present a measure of residual metal heterogeneity that would change in a non-linear manner as the sample weathered. For example, fractures could introduce the FIMAHE locally, increasing heterogeneity, and with increased exposure the separate weathered zones would coalesce, decreasing heterogeneity. By contrast, in samples of lesser fracture density, the FIMAHE would produce a heterogeneity that would reach a critical limit and then stabilize due to the crystal growth pressure and tensile strength conditions discussed in Section 4.2.2.3, thereby preserving that magnitude of heterogeneity. A greater exposure of a given stone volume to weathering agents, either by high terrestrial age or, more probably, by a high surface area to volume ratio, coupled with a minimal fracture density, generates a more pronounced FIMAHE.

To summarize, the FIMAHE suggests that iron oxide distribution is proportional to the fracture density within a given volume of highly weathered meteoritic material. It is possible too that FIMAHE-like circumstances exist for other types of weathering than simple oxidation reactions. Much further research is necessary to learn the constraints on these effects and countereffects.

4.2.5.2 Associated Weathering Mechanisms

A. Sample-specific factors

Petrologic differences may be responsible for differences in weathering behavior. Figure 4.11 shows that (1) all Ls and H4s show pronounced right lateral (positive) shifting, and (2) the behavior of H5s and H6s can be described as inconsistent or erratic. Similarly, the pattern produced by petrologic differences in Figure 4.5 is nearly identical to that produced by mass differences in Figure 4.15. The obvious temptation is to conclude a correlation exists somehow between recovered sample mass and petrologic type and meteorite class. However, no control is given over the original sample mass of the fresh falls, as opposed to the recovered sample mass measured after some 0.1 to 1.0 Ma within the ice sheet. It is therefore impossible from the evidence at hand to describe the order of the causal sequence; that is, whether (1) an original small mass is responsible for higher weathering (by greater surface area to volume ratios), or (2) greater weathering susceptibility to certain petrologic types generates smaller samples through disintegration as the tensile strength of the rock is overcome by internal crystal growth pressures.

The circumstance of nearly perfect superimposition of the dichotomous pattern in Figure 4.5 with that of Figure 4.15 therefore has at least one of four explanations: (A) Differences in weathering susceptibility due to class and/or petrologic type, which facilitate the breakdown of particular stones into smaller fragments. It may be useful to consider that certain volumes within a given stone may be well protected from attack irrespective of any FIMAHEs, possibly differing among petrologic types because of differences in textural integration; (B) Differences in weathering susceptibility due to initial differences in mass because of surface area to volume ratios; (C) coincidental selection for samples with mass and petrologic type difference correlations, as opposed to any intrinsic differences in weathering susceptibility; and (D) mass/class/type correlations may be based in pre-terrestrial compositional properties and thus independent of weathering effects.

(I) Class and petrologic type weathering

It is recognized that 19 specimens are too few to constitute a statistical sample of the Antarctic ordinary chondrite population. It was therefore decided to investigate the remaining population to determine if the trends discussed have any relevance on a larger scale where mass/class/type relationships are concerned.

Figure 4.26 is a logarithmic plot of the percent frequency distribution of 2066 unpaired H and L Antarctic ordinary chondrites representing each type of meteorite studied in this thesis. All Antarctic meteorites collected by the United States field teams through the 1986 field season are included with the exception of stones with masses in excess of 10 kilograms (source: SCES publications). The symbol locations represent bins defined in logarithmic space, and are not discrete data points. It can be seen that a greater proportion of stones in the 1 to 10 kilogram range is found among the H4 and L6 categories than in any other category. This is consistent with the data point positions in Figure 4.18. Harvey and Cassidy (1986) discuss the relationship of mass frequency distribution curves for Antarctic Allan Hills Main Icefield find to modern falls and conclude: (1) "The most startling difference between modern falls and Antarctic finds is the observed overabundance of H's in Allan Hills Main Icefield finds.," and (2) "...the H chondrites show a curve strongly skewed toward the smaller sizes." The researchers feel these differences are intrinsic to the pre-terrestrial meteoroid population sampled at the time these meteorites fell. In considering the weathering effects on the frequency distribution of terrestrial age estimates, Nishiizumi *et al.*, (1989) state that "The weathering hypothesis is contradicted by the greater abundance of H chondrites in Antarctic meteorite collections compared to

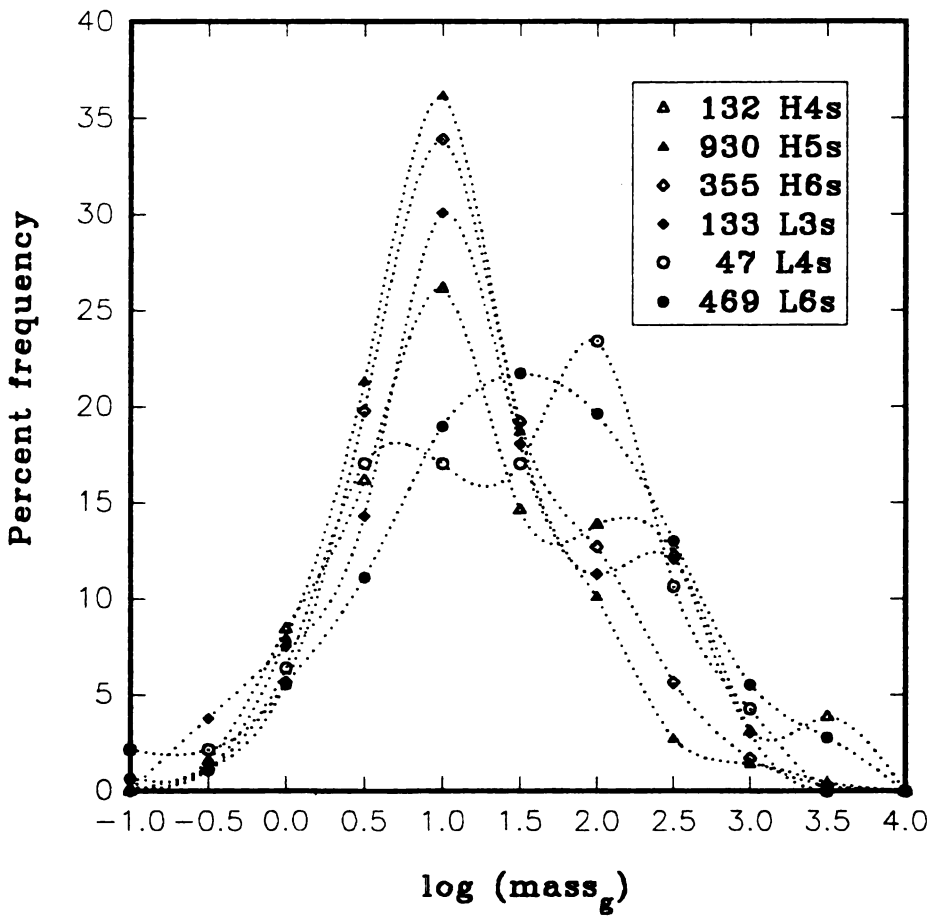


Figure 4.26. Mass frequency distributions among Antarctic ordinary chondrites. Symbol locations represent bins defined in logarithmic space, and are not discrete data points.

those found as recent falls in non-Antarctic areas." The "contradicted" weathering hypothesis in this case was the suggestion that weathering may disrupt the concentrations of cosmogenic radionuclides to skew the terrestrial age frequency distribution toward recent years.

However, the two Harvey and Cassidy (1986) observations taken together may suggest preferred H chondrite fragmentation (explanation (A) above) as responsible for the differences, thus indicating that physical as well as chemical weathering mechanisms could be operating within Antarctic meteorites. Huss (1991) felt that such meteorite fragmentation was caused by freeze-thaw effects in Antarctica. However, the body of this thesis suggests that H chondrites may be more susceptible to fragmentation than L and LL chondrites because they have, by definition, a greater abundance of reduced iron. More reduced iron might allow, during weathering, the required critical amounts of internal crystal growth pressures per unit volume necessary to overcome the tensile strength of the rocks and cause them to break apart. The means to verify this idea would be at hand if a database of all specimens with fusion crusts, and percentages covered thereof, were available. If true, a second theory would be needed to explain why some H4s appear to behave similarly to Ls.

By this reasoning, one might also expect the H population of Antarctic meteorites to yield a higher percentage of highly weathered samples than the L population. Again referring to the SCES publications, out of 644 H chondrites, 21.27 percent belong to weathering category C; whereas the Ls have only a 18.35 percent C weathering abundance out of 327 samples. It was noticed while making this count that 92 (61.67 percent) of all weathering category C L chondrites are L3 stones. Only 6 (0.9 percent) of the H chondrites are of petrologic type 3. Allowing that UOCs may be more susceptible to weathering for as yet unknown reasons, we might try subtracting these from our database to determine the relative susceptibility of EOCs to oxidation in the Antarctic environment. Subtracting all petrologic type 3 meteorites from both the H and L classes yields totals of 638 and 235 for Hs and Ls, respectively; and weathering category C stone abundances of 21.47 and 9.79 percent, respectively. Based on these data, it would appear that H chondrites tend to weather to C intensities more readily than L chondrites in Antarctica. This is consistent with the above supposition of greater fragmentation among H chondrites over L chondrites due to their greater metal grain content.

Although H4s are also among the most fractured specimens within the study sample suite, no trend in the occurrence of fracturing among Antarctic ordinary chondrites was found to

exist between any group, class or petrologic type in the SCES publications. The preponderance of the C category fracturing index among the H4 samples is therefore considered to be coincidental.

The occurrence of fragmentation would render explanation (B), that of weathering susceptibility because of sample size, as a possible secondary mechanism by which these differences could be intensified and accelerated. Explanation (B) is examined below.

(II) Mass-dependent weathering

Figure 4.27 again separates the samples into groups above and below two kilograms, but uses the ternary format of Figure 4.3. The distribution of sample weights among the data points reemphasizes the role of sample mass in weathering behavior. The distribution can be explained easily using the theory of pressure equilibration outlined in Section 4.2.2.3, and dramatizes the implications of Figures 4.12 and 4.13 — that smaller stones are more weathered than larger stones. The width of the linear trend in Figure 4.3 indicates the range in equilibrium states represented by the study sample suite. Theoretically, if a meteorite on the right-hand side of the cluster was in pressure equilibrium, and then exposed to additional weathering forces, it may break or its existing fractures may widen. The data point position for this stone on the

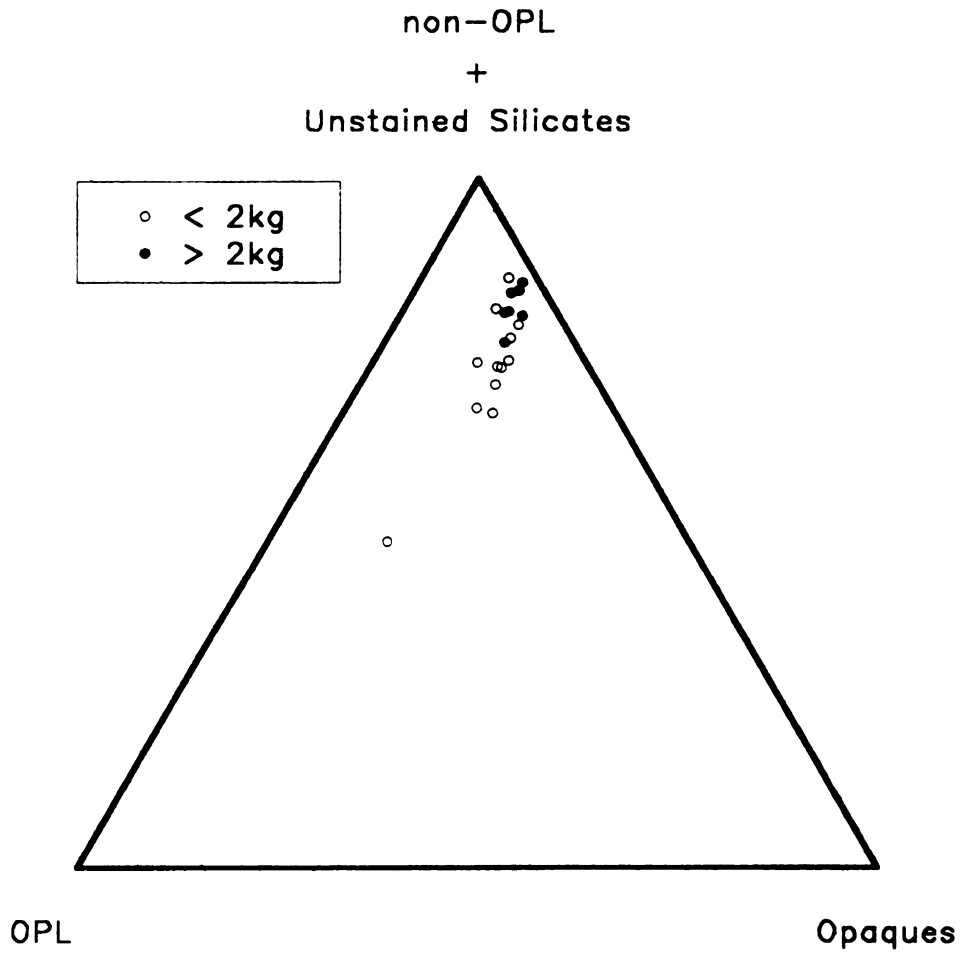


Fig. 4.27. Recovered mass distribution.

ternary would then be shifted further to the left as more OPL was formed at the expense of opaques. Therefore, the least weathered meteorites should plot in the "north-northeast" quadrant of the cluster. Samples that plot further "south-southwest" along the diagonal trend would necessarily be more weathered since, being further "west" along the trend, they are a greater fraction of the distance along from the ternary boarder perpendicular to the "OPL" end-member (0 percent weathered) to the boarder perpendicular to the "opaques" end-member (100 percent weathered).

Figure 4.27 shows the "north-northeast" quadrant to be precisely where the largest meteorites plot on the diagram. These theories allow less weathered interiors of large Antarctic meteorites to be in pressure equilibrium while at the same time allowing small, more weathered interiors to be in pressure equilibrium.

B. Curatorial weathering

Both Figures 4.12 and 4.13, each by an independent experimental oxidometer, display trends that show smaller stones tend to include the most weathered meteorites. Both trends also indicate that smaller stones have a more diverse range in weathering intensity than larger stones. This is

true for -LOI results obtained shortly after the samples were removed from their airtight packages.

However, Figure 4.14 shows that 16 months after the meteorites were first exposed to the South Central Lower Michigan climate, the smaller meteorites still show the greatest diversity and weathering intensity, but the splits from originally larger H4 and L parent samples have increased their weathering intensity, and the trend in Figure 4.13 is shifted in the positive direction. These diagrams indicate meteorite weathering during curatorial storage in Michigan. Considering the following curatorial history, it is not surprising to find evidence of weathering in storage: According to the SCES publications, each sample has been (1) removed from the Antarctic environment (of proposed metastable pressure equilibrium) preserved in Teflon sample bags sealed with tape and enclosed within padded metal boxes, all of which has been cleaned "to the same specifications used in processing lunar samples," at temperatures below 0°C to the Curatorial Facility of the NASA Johnson Space Center, Lunar Curator's Division, (2) sealed within a cold storage room at a temperature of -40°C and (3) cut or chipped in a nitrogen cabinet. The samples were then (4) sealed within airtight packaging, (5) relocated to a temperate mid-latitude climate, (6) removed from their packages, (7) broken to obtain 1990 -LOI samples, and (8) allowed to re-equilibrate for 16 months in non-

airtight containers with broken seals. It may be significant that two of the samples with the least amount of curatorial -LOI shifting were sealed in metal capsules with tight fitting lids while all others were in plastic capsules with somewhat loose fitting lids (see Table 4.1).

Comparison of Figure 4.16 with 4.17 suggests that because the Ls and H4 stones are larger and have less weathered interiors, they weather curatorially in a more consistent way than the smaller stones. If curatorial weathering has taken place, then an explanation is required for why it has apparently affected the larger samples more than the smaller ones. Such an explanation is implicit in (1) the FIMAHE and (2) differences in weathering susceptibility due to freshness; both discussed below.

(1) Recall from Figures 4.12 and 4.13 that the smaller samples tend to be more weathered than larger samples, using an arbitrary cut-off of 2 kilograms. It follows that the influence of the FIMAHE may prevail over any curatorial weathering effects among samples where the heterogeneity effect is magnified by intense weathering (as described in Section 4.2.5.1). The erratic behavior in Figures 4.16 and 4.18 among smaller stones would then be produced by selecting samples from within zones of differing oxidation intensity, as in Figure 4.24. Note in Figure 4.18 that the four samples with the highest left lateral shifts have

masses less than 800 grams. It appears that the lower the sample mass, the greater the chance for producing a left lateral shift. Left lateral shifting seems to depend less on laboratory weathering than on residual metal grain distribution, which is proportional to the FIMAHE. Whether a left or right lateral shift occurs for a low mass meteorite in this study therefore depends on the intensity of the FIMAHE and on the temporal sequence of the two analyses.

Different zones within a larger, "fresher" meteorite would be much more alike unless acted upon by differential curatorial weathering forces. Therefore, large samples are more likely to produce right lateral shifts than smaller samples.

(2) Initially less weathered meteorites would also be more susceptible to curatorial weathering than more weathered stones due to their freshness. As secondary weathering products are produced for which V_{prod}/V_{react} is greater than unity, it is possible the layer of product becomes "protective," meaning the rate-determining mechanism is diffusion of mobile reactant and/or product elements through the layer itself (e.g., Velbel, 1993). As protective layers of oxide build up across metal grain surfaces, reaction rates could therefore be expected to decrease. Also, the filling of fractures, cleavage planes and grain interstices

with product could conceivably function to lower the effective permeability of the rock. Therefore, the less weathered a given chondrite is initially, the more it should respond to curatorial weathering forces in storage.

One should be able to notice a preferred positive trend among the Δ-LOI data if curatorial weathering forces are present, since these would increase the weathering intensity across the board and so be superimposed upon all previous weathering effects. Such a trend would be recognizable as a greater average magnitude for Δ-LOI values in the positive direction than the average magnitude of the negative shifts, which theoretically result from the influence of the FIMAHE or other factors. Figure 4.19 illustrates the Δ-LOI vector by direction and magnitude between the two sample runs and presents the 2 kilogram cut-off. Notice how negative Δ-LOI values decrease in magnitude as sample mass increases.

Table 4.3 performs some statistical analysis to establish a qualified mean based on the elimination of outliers (where coefficient of variance values greater than 0.5 indicate an outlier). The variance is given by;

$$\mathbf{V} = \frac{\sum_{j=1}^{n} \left| x_j - \bar{x} \right|^2}{\mathbf{n}},$$

Table 4.3. Determination of delta -LOI means

Negative		Positive	
Outlier	Valid	Outlier	Valid
	2.50		7.72
0.47			10.23
	9.40		10.71
	6.66		11.19
0.71			11.91
	9.41		4.29
	9.16		10.59
		32.14	
			6.55
			9.29
			1.31
Arith. mean	5.47		10.54
Qualified mean	7.43		8.38
Variance	7.14		10.54
Standard deviation	2.67		3.25
Coefficient of variance	0.36		0.39

where x_j is a sample, $\bar{x}$ is the mean, and n is the number of samples. The standard deviation is then given by;

$$\mathbf{sd} = \sqrt{\mathbf{v}},$$

and the coefficient of variance by;

$$\mathbf{cv} = \frac{\mathbf{sd}}{\bar{x}}.$$

Arithmetic mean values are greater by 92.7 percent in the positive direction than the negative direction and the qualified mean values are 12.8 percent greater. It can be observed that even by these conservative statistical criteria, -LOI values favor an increase over the 16 month storage period between analysis, suggesting that a significant amount of oxidation has occurred during this period. At a minimum, it is advisable to take precautions against the possibility of curatorial weathering phenomena by maintaining an airtight and moisture deficient atmosphere for samples to be stored for long time periods. In addressing the long known curatorial oxidation effects with regard to nickel-iron meteorites, Buchwald and Clarke (1989) point out that "Understanding this corrosion process has obvious implications for developing strategies to terminate, or at least minimize deterioration that continues when these scientifically important materials are incorporated into research and exhibit collections."

5 CONCLUSIONS

1. Petrographic modal analyses, designed to characterize the overall appearances of "rustiness" which lead to meteorite classification within the ABCe system, show a wide variation within the assigned weathering category (C) for Antarctic ordinary chondrites. This lack of consistency reflects incongruous proportions of OPL and NNL materials among different specimens (and even within different areas of the same specimen). These lead to classifications that are non-representative of actual alteration intensities, but instead of the extent of low-volume stain (NNL) materials. Thus, the ABCe system presently employed is heavily biased by the thin, volumetrically insignificant but visually dominant NNL stains. Such wide variability observed within an established weathering category is significant and calls for a restructuring of the index.

2. An experimental modal index, designed to represent the volume of iron oxide produced through weathering, does not correlate with the experimental index based on H- and

L-corrected negative losses on ignition. However, good reproducibility of the -LOI data suggest that the -LOI method might serve as an inexpensive and complimentary alternative to the ABCe system for the iron oxide-based classification of weathering intensity in highly weathered Antarctic equilibrated ordinary chondrites. Both experimental indices also show a substantial variability which extends beyond that interpreted for a single weathering category.

3. Small-scale metal grain and iron oxide heterogeneities exist, particularly among severely weathered ordinary chondrites, which can inhibit the reproducibility of oxidometer values.

4. The distribution of relict metal grains is determined to a large degree by the fracture distribution.

5. Iron oxide production continues within samples while in storage in temperate climates with high average relative humidities and temperatures. It appears that this curatorial weathering may be mitigated or prevented by maintaining a tight seal on samples while in storage.

6. Iron oxide production can be arrested by the tensile strength of the surrounding rock mass.

7. In the dynamic environment of the Antarctic ice sheet, where meteorites have resided for long period of time, H chondrites appear to be more susceptible to fragmentation than L chondrites. This appears to be due to their higher reduced metal content, which produces internal pressures sufficiently high to weaken the rocks along existing fractures during iron oxide production, thus overcoming the tensile strength of the rock.

8. Consistent with conclusion number 7, the H chondrite population was also found to contain a higher relative abundance of highly weathered meteorites than does the L chondrite population in Antarctica.

9. H4 chondrites tend to occur as larger stones, than H5 and H6 chondrites.

APPENDIX A

PETROGRAPHIC DESCRIPTION OF SAMPLES

APPENDIX A

PETROGRAPHIC DESCRIPTION OF SAMPLES

Introduction

The following is a set of petrographic descriptions of the 19 NASA Antarctic meteorite samples and the non-Antarctic meteorite Carichic. The descriptions have been generated from the examination of 38 highly polished microprobe mounts and two Carichic thin sections. For descriptive purposes only, an arbitrary texture scale was created where "fine-grained" is ≤ 2.5 μm; "medium-grained" is > 2.5 and ≤ 25 μm; and "coarse-grained" is > 25 and ≤ 250 μm in average diameter.

The microprobe mounts were prepared at the Johnson Space Center in Houston, Texas by the NASA Antarctic Meteorite Working Group. However, for the purpose of this research, they were used as thin sections for the petrographic characterization of iron oxide type and distribution, and for photomicrographic documentation of notable features. The microprobe mounts were not necessarily cut to 30μm standard thin section thicknesses. Birefringence colors may

therefore deviate from those commonly associated with observed minerals.

Additional chips cut from different areas on the 19 Antarctic specimens were examined petrographically at the Smithsonian Institution's National Museum of Natural History, Division of Meteorites in Washington D.C. The Carichic thin sections were prepared at the Department of Geological Sciences at Michigan State University in East Lansing, Michigan.

Virtually all features mentioned in these descriptions have been photodocumented, with the exception of those found in the Smithsonian Institution samples. Attempts were made to photograph these latter chips, but were unsuccessful due to a camera malfunction. The catalogue of photomicrograph transparencies can be referenced for additional descriptive details (see Appendix B).

ALHA81031,19 L-3

Chondrule types in this specimen include microporphyritic olivine with euhedral crystals, granular olivine, cryptocrystalline excentroradial pyroxene, and barred olivine varieties. Opaque material fills portions of spaces between olivine plates in some of these latter chondrules. The chondrules are distinct, closely packed and range in size from 0.2 to 2 mm in diameter. There is no observable fusion crust. The matrix is fine- to medium-grained with considerable opaque material, and presents a definite clastic texture, where the individual sedimentary components are easily resolved. Some of the matrix can be seen filling embayments on granular chondrules. Other chondrules are dimpled. The chondrules are circular to slightly oblate in outline, with the oblate variety most common among the porphyritic and granular populations. Some microporphyritic chondrules are rimmed by 1 to 2 fine-grained alternating rings composed of a mixture of transparent and opaque material. Opaque phases exist as rounded blebs in size fractions from very fine to approximately 0.5 mm in diameter, with a calculated modal abundance of 11 percent. The fine grain size of this material gives the specimen a sooty appearance typical of type 3 matrix (Brearly *et al.*, 1988).

Deposits of OPL material are present in direct contact with opaque phases as haloes and partial haloes, comprising some 3.4 percent of the sample area. The rest of the specimen is lightly stained (52.8 percent). The mount is first order gray to first order yellow in color between crossed polarizers, indicating a non-standard thin-section thickness. One chondrule contains a "boxwork" of red rust, while other olivine grains appear to contain large scale etch pits. The *in situ* alterations are more red-orange in color than ruby red, again possibly due to the non-standard thin-section thickness.

The Smithsonian chip ALHA81031,4 was very similar in appearance, presenting haloes and partial haloes of OPL with light colored NNL stain.

ALHA77230,48 L-4

This specimen contains many readily delineated microporphyritic olivine, excentroradial pyroxene, granular olivine, and barred olivine chondrules set in a fine to moderately coarse textured matrix of fine material, crystal grains and chondrule fragments. Chondrules range from 0.2 to 4.0 millimeters in diameter. Some chondrules are rimmed with opaque particles, and very fine shock fractures can be detected here and there which each crosscut many chondrules simultaneously. Opaque phases are highly variable in size, and are subrounded to highly irregular in outline. The opaque phases comprise some 13 percent of the sample area.

A thin fusion crust is intact over most of the specimen length. OPL-filled fractures within the fusion crust are present locally, setting the fusion crust apart in this regard from most other areas in the specimen, which are lacking in OPL. The calculated modal abundance of OPL in this specimen is 2.0 percent, while that for NNL stain is 54.6 percent. NNL material is light brown in color and can be found confined to intercrystal spaces both within and between chondrules across the specimen. Very few obvious fluid migration avenues not been stained by this material. Some restricted regions close to the fusion crust have been stained darker than elsewhere in the sample.

Among the notable features present are barred olivine chondrule fragments with rust staining between platelets, widespread clouding of chondrules and crystal grains and a large pyroxene chondrule with an unusual strained extinction pattern. Some olivine grains display a fine network of intersecting cleavages lined with a well-crystallized oxide.

The Smithsonian chip ALHA77230,7 has a thin fusion crust over most of its length. NNL stain is light brown within and between chondrules, and confined to intercrystal spaces. All obvious migration pathways have been stained by this material. The sample contains many glass-containing microporphyritic chondrules containing euhedral olivine crystals. The glass in these chondrules is devitrified in many cases.

ALHA81027,26 L-6

Of the few chondrules discernible in this specimen, microporphyritic olivine and granular olivine varieties are evident. Crystal grain sizes range from 0.2 to 2.0 mm in diameter. A faint suggestion of textural lineation (fabric) exists among populations of elongated opaque grains. The opaque phase sizes and concentrations vary across the specimen from large and sparse to small and abundant, and comprise a calculated 12.4 modal percent of the area. The matrix is totally recrystallized, there is no fusion crust, and the specimen is moderately fractured.

The sample exhibits a nearly even, light yellow NNL staining (74.6 percent), with localized OPL deposits (4.2 percent), as well as a non-stained area in its interior. Some fractures which penetrate into the interior are devoid of secondary deposits. Other fractures have been filled along portions of their lengths. A granular, amorphous oxide appears within a ring of OPL material. Some rust haloes are light yellow or gold in color but show the same internal structure as OPL material found elsewhere. Some void spaces are partially filled with secondary products. One opaque grain near the edge of the sample displays a pattern of alteration deposits which resembles that of a classic "soil horizon" formation on bedrock (refer to Figure 3.13). Fractures penetrate to depth within the grain, allowing

migration of reactive fluids to produce a product distribution which increases in density outward toward the grain exterior.

The Smithsonian chip ALHA81027,5 possesses a isolated fusion crust. The NNL stain distribution is uneven, with a nearly even light yellow NNL stain occupying the region nearest the fusion crust, and a non-stained area occurring in the sample interior.

ALHA77004,22 H-4

This specimen contains readily delineated microporphyritic olivine and pyroxene chondrules, some granular olivine, and a few barred olivine and pyroxene chondrules. The surrounding matrix ranges in texture from fine to moderately coarse grained, with the chondrules themselves ranging in size from 0.2 to 1.0 mm in diameter. The specimen is heavily fractured, with many fractures branching dendritically and partially oxide-filled. Very little of the fusion crust remains intact. Opaque phases are present at a calculated modal abundance of 13.4 percent.

NNL material is extensive between crystals, and along fractures and cleavages within crystals, comprising a total calculated modal abundance of 55 percent within the specimen. OPL deposits (calculated modal abundance 5.8 percent) appear opposite a fusion crust remnant and in association with opaque phases as partial haloes. The darkest oxide stains follow the large scale dendritic fracture network across the specimen. The degree of staining decreases toward the edge of the mount possibly due to thinning of the specimen in this direction.

Among the notable features present are an olivine chondrule containing a partially OPL-filled void space, an olivine chondrule containing a microfault and possessing an

interesting platelet symmetry, preferential staining of glassy areas, and clouded pyroxene chondrules, one of which contains polygonal features resembling etch pits.

The Smithsonian chip ALHA77004,12 contains no fusion crust. It presents light staining with opaque grains sparsely affected by OPL replacement, appearing again as partial halo deposits along eroded opaque edges. The OPL is orange in color.

ALHA77208,29 H-4

Most chondrules in this specimen are readily delineated and include microporphyritic and granular olivine, barred olivine, excentroradial pyroxene, and cryptocrystalline pyroxene varieties. Chondrule diameters range from approximately 0.2 to 0.8 mm. Many olivine crystals within and outside chondrules are euhedral primocrysts. The sample is moderately fractured with most fractures rust-filled, and the matrix is fine grained to moderately coarse. A large, widened fracture zone contains copious amounts of rust which appears to have moved freely into the space, uninhibited by surrounding material. Opaque phases appear splotchy, containing silicates and displaying a partly disconnected/partly interconnected order. There is no fusion crust present.

Some chondrules are surrounded by haloes of fine-grained opaque material. The specimen is extensively stained in three distinct but overlapping tones of rust; OPL blebs associated with opaque phases, dark orange NNL staining, and light orange NNL discolorations which coat grain surfaces. A wide fracture zone contains copious amounts of rust which appears to have moved freely into the space unencumbered by surrounding material. One noteworthy chondrule is nearly surrounded by opaque phases which are altering to OPL lightly along the chondrule/opaque contact.

Other possibly important features include intercrystal oxide nodules (OPL-appearing oxide deposits visible within crystal grains), teardrop shaped features resembling pitting and opaque phases which appear to have been altered from the interior outward toward the exterior regions.

Smithsonian chip ALHA77208,4 contains red rust fracture fillings and has a dark, soiled appearance caused by a heavy NNL stain. There are many examples of OPL haloed opaque grains. The sample had no visible fusion crust.

ALHA77225,18 H-4

The chondrule types in this undifferentiated meteorite include granular olivine with euhedral to subhedral grains, pyroxene in coarse and cryptocrystalline excentroradial form, fine grained microporphyritic chondrules, and barred olivine chondrule fragments. They range in approximate diameter from 0.15 to 1.0 mm. The chondrules are readily delineated from the surrounding fine-grained matrix. Opaque phases are highly irregular in outline and partially surround some chondrules. They are present at a calculated modal abundance of 15.4 percent. There are very few visible fractures, and the entire specimen transmits in the first order gray in crossed polarized light, suggesting a non-standard thin-section thickness. Examples of partially devitrified glass can be found. There is trace of a fusion crust in this chip.

The rust staining is present at 51.2 percent, but less opaque than in other specimens. There are many examples of cleavage plane fillings exhibiting optical continuity upon stage rotation (see Appendix B). Some examples of ruby red OPL (4.4 percent) can be found in association with opaque materials. However, most OPL is dark orange in color rather than ruby red, possibly due to thinner mount thickness in these areas. There are also portions of OPL in the sample which seem to pinch out, becoming orange in color and

allowing greater light transmission, both in plane and polarized light. Many void spaces can be identified which contain thick growths of oxide material in botryoidal morphologies. There are many examples of cleavage plane fillings exhibiting an optical continuity upon stage rotation suggesting a transformation weathering mechanism.

The Smithsonian chip ALHA77225,10 contains devitrified glass, partial OPL haloes around opaque grains, light NNL staining, orange colored fracture fillings, and ruby red OPL deposits which pinch out near sample boarders, becoming lighter in color as they do so.

ALHA77226,37 H-4

The chondrules in this specimen range from 0.2 to 1.7 mm in diameter and consist of microporphyritic olivine with euhedral crystals, excentroradial pyroxene, and barred olivine varieties, with the former most abundant. One large (0.7 mm in diameter) euhedral olivine crystal is present. Partly devitrified glass can be found between olivine platelets in one barred olivine chondrule. This specimen is heavily fractured and possesses moderate chondrule/matrix integration. Fusion crust is fractured and discontinuous. Some devitrification is present within the glass zones of the fusion crust, and many additional features of interest are visible in and around the area. Among these are oxide-filled vesicles within the glass itself. Opaque grains comprise some 15.2 percent of the sample.

Rust staining is dark, extensive (59.6 percent) and almost opaque. Red oxide deposits fill most fractures. OPL haloes are sparse (8.6 percent total OPL), and many appear to be poorly crystallized. The fusion crust penetrates the meteorite interior along one corner of the chip, perhaps as a result of melted material permeating, collecting and solidifying within a pre-existing fissure as it migrated away from the friction-heated surface upon atmospheric entry. Additional features include a clouded pyroxene chondrule fragment, and a pyroxene chondrule with unusual

linearities suggesting removal of silicate material, and which have subsequently been filled with oxide material. Smithsonian chip ALHA77226,20 is different from chip '37 in that the OPL is nearly absent, except near one edge, and NNL stain is also sparse and light.

ALHA77232,16 H-4

The chondrule types in this specimen range from 0.33 to 1.03 mm in diameter, and include microporphyritic olivine and microporphyritic olivine/pyroxene chondrules, with excentroradial pyroxene and barred olivine chondrules in lesser numbers. A few of these latter chondrules exhibit a sweeping extinction pattern, and some pyroxene chondrules have slight convolutions in their radiating plates. Except for the cases of pure pyroxene chondrules (2 found), the chondrule/matrix integration is high, rendering chondrule boundaries indistinct. Olivine grains are predominantly euhedral, and opaque grains are highly irregular in outline, while remaining roughly equidimensional in form. This sample is moderately fractured, and presents first order gray and yellow birefringence colors under crossed polarizers, suggesting a non-standard thin-section thickness. Opaque grains have a calculated modal abundance of 13.2 percent in this sample.

NNL stain can be found throughout the sample (61.2 percent calculated modal abundance). This material tends to avoid staining chondrule interiors increasing the contrast between chondrules and matrix in plane light. One chondrule is partially surrounded by a dark orange variety of rust which appears similar in structure to red OPL in other specimens. OPL itself is present at an abundance of 3.0 percent. The

color difference in this case is attributed to the non-standard mount thickness. Examples of devitrified glass exist which show little sign of alteration, in contrast to *in situ* alteration immediately adjacent. Similarly, glassy phases in barred olivine chondrules do not show signs of preferential attack. Additional features include examples of clouded olivine crystals, what appear to be brecciated pyroxene crystal fragments set within a devitrified glass groundmass which also exhibits transverse clouding, and examples of amorphous oxide material lining void spaces.

Smithsonian chip ALHA77232,10 displays light grayish orange, homogeneously distributed NNL staining which avoids staining chondrule interiors, as with the '16 chip. Other features are similar to chip '16 as well.

ALHA77233,21 H-4

The chondrules in this specimen are moderately defined and range from 0.25 to 0.83 mm in diameter. Those which can be identified are largely of the microporphyritic and granular varieties, with lesser amounts of excentroradial pyroxene chondrules. One compound chondrule exists which contains two fused individuals, both of the droplet pyroxene variety. Also, one dark-zoned chondrule (Dodd and Van Schmus, 1971; Dodd, 1981 p 116.) was found. The matrix crystallinity is moderately coarse. Most of the finer details are obscured by oxide staining (57.4 percent calculated modal abundance). The meteorite is moderately fractured in this thin-section, and possesses a fusion crust only along one small (1.38 mm) section.

The specimen is heavily stained, but some areas, i.e. interiors of individual crystal grains and chondrules, are unaffected. The NNL stain is light orange-brown, and red rust fracture fillings line most, if not all, fractures. The zoned chondrule exhibits an alteration pattern in its interior different (more cloudy) than that of its outer portion. One microporphyritic chondrule contains olivine crystals which show clouding features resembling etch pitting under high magnification. The specimen also contains a pyroxene chondrule with interlocking grains whose contacts are smooth but irregular as though melted and

recrystallized. This chondrule is also etched with faceted (prismatic) pits. Smithsonian chip ALHA77233,13 displays a homogeneous light orange-brown NNL stain which, as in chip '21, avoids some chondrule and crystal grain interiors. Other features are also similar to those of chip '21.

ALHA77182,36 H-5

The chondrules in this meteorite range in size from 0.2 to 1.3 mm in diameter and include mainly microporphyritic olivine and granular olivine species in roughly equal proportions, with the remainder comprised of barred olivine, pyroxene, and dark-zoned varieties. One metal-bearing, large and rounded olivine crystal chondrule was found. A few large (≈ 0.5 mm diameter) olivine crystals exist which range in form from euhedral to anhedral. There are many chondrule fragments distributed throughout the specimen. Chondrule outlines are delineated in many cases by opaque blebs which are present in moderate abundance (10.4 percent calculated modal abundance) and highly interconnected. There is no fusion crust and no detectable fracturing of the sample as a whole.

OPL predominates in abundance (26.4 percent) over NNL stain (15.0 percent), with very nearly every opaque particle having been altered to some degree. OPL can be found aligned parallel to pyroxene crystal platelets in one chondrule. Signs of clouding are easily found among the olivine crystals. One olivine chondrule fragment presents alteration products along devitrified glass plates. With this exception, the chondrule interiors appear untouched by alteration. Botryoidal growths line void spaces in several locations. The void space deposits appear porous and grow

discontinuously, requiring refocusing of the microscope to view the texture across their entire thickness. It should be noted that nowhere else but within such void spaces has the botryoidal morphology been observed.

Smithsonian chip ALHA77182,15 has a dark soiled black appearance with a high amount of OPL and very little NNL stain, as with chip '36.

ALHA79025,16 H-5

Most chondrules in this specimen are readily delineated and range in size from approximately 0.3 to 3.0 mm in diameter. These include microporphyritic chondrules containing euhedral olivine crystals, which comprise the majority of the chondrule population, and granular olivine and pyroxene chondrules, which are in the minority. One barred olivine chondrule fragment was identified. Minor portions of a splendidly devitrified fusion crust remain.

Many chondrules are outlined by oxide material. The opaque phases, which make up some 15.4 percent of the specimen, range from semirounded to highly irregular in outline. The largest bleb of this material resides within an oblate granular olivine chondrule, which also contains an additional small, oblate, barred and rimmed olivine chondrule. The meteorite chip does not appear to have been fractured.

The specimen is extensively stained (43.3 calculated modal abundance), exhibiting a network of NNL strands together with OPL blebs (7.4 percent) which tend to partially envelop chondrules. Clouded areas within olivine grains show linear patterns.

Smithsonian chip ALHA79025,5 contains a great deal of OPL material with very little NNL stain. The chondrules are typically haloed by OPL, as with chip '16.

ALHA79029,21 H-5

This specimen is composed of microporphyritic olivine, excentroradial pyroxene and barred olivine chondrules and chondrule fragments. One excentroradial pyroxene chondrule contains subhedral olivine crystals. Most chondrules are readily delineated within a fine-grained matrix, and range in diameter between 0.2 and 1.0 mm approximately. The fusion crust is thin and sparse, but some portions contain crystals. A shallow but intact crystal-bearing fusion crust is present. Opaque phases are highly irregular in outline, heterogeneously distributed, and comprise some 11.6 percent of the sample. The sample displays a moderate amount of fracturing, with many of the fractures being wholly or partially filled with oxide deposits. The fractures are subparallel near one linear edge of the chip.

This specimen has a soiled appearance with extensive (62.0 percent) NNL staining. One portion of the fusion crust appears to have been completely replaced (or displaced) by OPL material. OPL rust is present at a 7.2 percent calculated modal abundance. The smaller chondrules are clear, appearing to be less affected by rust-producing alteration processes than larger chondrules. Some examples of OPL material are dissociated from opaque phases. Additional notable features include patterned clouding in a pyroxene chondrule fragment and in olivine chondrules, a

possible example of altered glass, and well pronounced features resembling etch pits in pyroxene grains and chondrule fragments.

Smithsonian chip ALHA79029,6 presents very light NNL staining and very little OPL material, except near one edge where it appears deep orange in color, indicating a non-standard thin-section thickness.

ALHA84075,7 H-5

A moderate amount of fracturing is immediately apparent in this specimen. There is one extended, straight and rust-filled fracture crosscutting the sample. Some fractures remain unfilled with rust. Others are partially filled with opaque material.

Some chondrules are poorly defined. Others, including a few droplet chondrules, are readily delineated and include microporphyritic, excentroradial pyroxene and granular olivine varieties ranging in size from approximately 0.2 to 1.0 mm in diameter. The matrix appears well recrystallized but remains somewhat fine-grained and clastic in appearance. A small portion of the fusion crust is still intact. Opaque grains are present at a calculated modal abundance of 15.6 percent.

This meteorite is extensively stained (68.6 percent), and appears light brown in color. NNL circumscribes some chondrules while staining the interiors of others. Most of the unstained chondrules are of the droplet variety. With the exception of these unstained chondrules, the staining appears evenly distributed. There are relatively few areas of OPL rust (5.6 percent).

One small chondrule has a population of OPL blebs within its boundaries, and another displays a rust growth pattern which is parallel to its radiating pyroxene plates. Very little matrix material remains unstained, while the pyroxene chondrules seem relatively resistant to staining. Certain crystal grains (commonly pyroxene) tend to show optical continuity with crystallized rust zones filling their fractures and cleavage planes. This optical phenomena may be consistent with a transformation weathering process.

The Smithsonian sample (chip ALHA84075,0) presented few differing characteristics. As with chip '7, it was heavily stained, only appeared a dark brown color as opposed to light brown. Like chip '7, chip '0 showed this stain to be evenly distributed, and possessed very few OPL deposits.

ALHA85025,10 H-5

This specimen is heavily fractured with a very coarse crystalline matrix surrounding microporphyritic, granular olivine, recrystallized pyroxene and coarsely crystalline excentroradial pyroxene chondrules. The chondrules range from 0.3 to 1.7 mm in diameter, and are set within a coarse textured matrix. One barred olivine chondrule was found. These chondrules are poorly defined with few discernible internal features. The opaque phases appear as rounded blebs, and are homogeneously distributed, but of varying sizes. They occur in a calculated modal abundance of 17.0 percent. NNL staining is manifest as an interconnected network across the specimen (33.2 percent). OPL (12.8 percent) appears in isolated areas, some of which are located in the vicinity of the fusion crust. The appearance is similar to that of ALHA77288,34. The oxides in this meteorite show very smooth color transitions from light yellow to deep red, making it very difficult to point count the OPL.

Among the more notable characteristics in this specimen is a set of opaque, NNL-surrounded dendritic features within a chondrule or crystal fragment, the rust-filled fracture patterns near and within the fusion crust, a clouded region which displays unique optical effects (internal

reflections), and examples of subrectangular features in olivine grains resembling etch pits.

The Smithsonian sample had no chip number (presumably zero), and presented no additional or differing features beyond those described above. Very smooth color transitions were observed among the oxides from light yellow to deep red, as with chip '10.

ALHA77271,28 H-6

The main chondrule type identified in this sample is microporphyritic olivine, including some chondrules with larger than usual (1.25 mm) crystals. Only one each of the cryptocrystalline pyroxene and excentroradial pyroxene chondrule varieties were found, the latter being a chondrule fragment. The chondrules have poorly defined boundaries and are set within a well crystallized matrix. They range from 0.25 to 0.88 mm in diameter). The opaque phases are highly irregular in outline and range in relative abundance from approximately 12 to 20 percent in different parts of the specimen. The average calculated modal abundance for the opaque grains is 13.2 percent. A small portion of fusion crust remains partially intact. No crosscutting fractures were detected. However, a fine network of rust-filled fractures can be found near the fusion crust.

The oxide texture gives a splotchy or spattered appearance rather than that of networked strands, as in some other samples. Some OPL examples possess well-defined internal structures and exhibit optically continuous sweeping extinction. Orange colored rusts can be found lining and partially filling void spaces in a bulbous or botryoidal habit. Many examples of product-lined pore spaces exist. Most oxides in this specimen possess very clean, sharp contacts with their neighboring constituents. The OPL

deposits are clearly in the process of replacing opaque phases, as evidenced by the sutured borders of remnant opaque grains, and outlines of the OPL deposits, which are consistent with those of the grains they are replacing. Some olivine grains present a zoned, clouded appearance with distinct lineations resembling etch pitting.

This sample definitely thins toward the edge, as evidenced by diminishing birefringence colors from second order blue to first order yellow on a single large olivine grain. This meteorite also possesses a chondrule with a highly eroded boundary, appearing to have been attacked, introducing the possibility of silicate weathering. This meteorite contains the best example found in the 19 specimens of a very well crystallized oxide product of exceptional detail and color variation (see 29;XN;40/.70 in Appendix B). Referred to in the text (Figures 3.19 and 3.20) as a sharp contact phase, this material is interconnected with other, similar but less striking materials. Some remnant opaque material remains in contact with this oxide, suggesting it represents a nearly complete replacement of a former metal grain.

Smithsonian chip ALHA77271,6 possesses no fusion crust. Its texture, including OPL and NNL abundance and distribution is very similar to that of chip '34.

ALHA77288,34 H-6

This specimen exhibits a high degree of chondrule-matrix integration. Chondrule relics include three or four pyroxene chondrules and only one barred olivine chondrule with most "bars" obliterated by secondary processing. Chondrule diameters range from 0.5 to 1.0 millimeters. No obvious fracturing is apparent on a section-wide scale. However, some alteration products appear to follow a pattern consistent with fracture fillings. The matrix is highly recrystallized around evenly distributed opaque grains (16.0 percent) A few large (up to 1.0 mm in diameter) olivine crystals are present. No surviving fusion crust is visible.

The limonite network is distributed consistently with light and dark NNL predominating (46.6 percent) and OPL present moderately (11.2 percent). Many opaque grains have thin partial haloes of OPL. The NNL permeates every sector of the sample to nearly constant densities, appearing homogeneous on a section-wide scale. This is possibly due to the highly granular texture of this petrologic type 6 sample, which might allow greater interconnectedness of fluid-conducting avenues. Of the few OPL examples present, some show a full range of color tones from yellow to red. These tone variations occur in OPL material deposited along the sample perimeter and are very likely thickness related. It is therefore difficult to distinguish NNL from OPL in

this sample. The deepest red deposits seem to outline former boundaries of opaque grains.

Additional notable features include clouded olivine crystals showing some linearity in the cloud patterns, a pyroxene chondrule with remarkable color diversity, and a region of NNL which appears to display incipient crystallization.

The Smithsonian Institution sample chip ALHA77288,4 exhibited virtually identical features to chip '34, including linear clouding patterns in an olivine crystal group, and similar proportions and distributions of OPL and NNL oxide varieties.

ALHA84082,9 H-6

This sample contains microporphyritic, granular olivine and excentroradial pyroxene chondrules and chondrule fragments. Some microporphyritic chondrules contain euhedral olivine grains. The chondrules are readily delineated and are set within a moderately coarse matrix. They range from 0.37 to 0.85 mm in diameter. Opaque phases exhibit rounded, irregular outlines. Many pyroxene crystals are highly birefringent, indicating a non-standard thin-section thickness.

OPL and NNL phases can be found in both the fusion crust and chip interior. However, there are differences in the relative amounts of these materials between the two regions. OPL deposits are sparse across the specimen as a whole, but are present at a calculated modal abundance of 15.2 percent, found mainly in the vicinity of the fusion crust, and are clearly associated with opaque phases; while the orange-brown NNL (38.6 percent) does not present a readily detectable association with any specific primary phase. NNL staining is absent at the opposite end of the sample from the fusion crust. One chondrule has a cloudy center which has been stained preferentially relative to the outer portion. This central nucleus also presents a pitted appearance under high magnification and differs in extinction from surrounding portions of the crystal,

suggesting zoning. This pitting occurs in linear and parallel rows within a crystal interior, and with rectilinear or oblate to irregular outlines. Smithsonian chip ALHA84082,0 displayed similar differences in the relative amounts of OPL and NNL across the specimen.

LEW85322,11 H-6

This specimen is marked LEW85332,11 on the bottle label. This is believed to be erroneous. Rubin and Kallemeyn (1990) report petrologic and bulk chemical data for LEW85332 that show it is probably a carbonaceous chondrite of a unique type. Microprobe data from Rubin and Kallemeyn (1990), indicate olivine to have a wide composition range for this meteorite (Fa_{2-37}) with a mean of Fa_9; less abundant pyroxene has a composition range Fs_{1-30}. This is unlikely for a petrologic type 6 chondrite.

According to Rubin and Kallemeyn (1990), the thin-section for LEW85332 shows "...an aggregate of small chondrules (up to 1.2 mm across, but most are less than 0.5 mm), chondrule fragments and irregular granular masses set in a translucent yellow-brown matrix. Chondrules are mainly porphyritic olivine and radial pyroxene/cryptocrystalline. Minor amounts of nickel-iron and sulfide are present, as small grains scattered through the matrix, and locally concentrated around chondrule rims." This texture is petrologically dissimilar to that of a type 6 chondrite.

The thesis specimen is composed primarily of micro-porphyritic chondrules with euhedral olivine crystals, and granular olivine chondrules. Other chondrule types are present in very small abundances only. Most chondrules are

poorly delineated. One cryptocrystalline pyroxene chondrule has a border partially integrated with opaque material. The opaque phases range in size from submillimeter dimensions to very fine particles, and have irregular outlines. Most olivine crystals are rounded and quite large, with one crystal pair slightly greater than 1 mm in diameter. There are few discernible fractures. However, rust-filled avenues can be found which resemble fracture fillings with the only difference being that of a tortuous, rather than straight, pathway.

The rust patterns are unusual with numerous OPL deposits and very little NNL staining. Curiously, the distribution of the OPL material does not appear to be as dependent on opaque phase distribution as in other samples. OPL deposits may represent completely altered metal grains in this case. Vacuolization patterns on select olivine grains resemble etch pitting and seem to occur within specific zones. Some oxide deposits protrude into void spaces in a bulbous or botryoidal habit. NNL stain penetrates as far as fractures extend into grains.

The Smithsonian sample was a chip from yet a third Antarctic meteorite, LEW85323, and is not relevant to this thesis.

LEW86015,10 H-6

A fractured and devitrified fusion crust borders one side of this specimen. Chondrule types include microporphyritic olivine, excentroradial pyroxene, and barred olivine varieties with the microporphyritic olivine making up the majority. The chondrules are readily delineated, ranging from 0.2 to 0.88 mm in diameter, and the matrix is coarse to fine grained. The opaque phases in this moderately fractured specimen are highly irregular in outline. Opaque grains are present at a calculated modal abundance of 17.0 percent.

Most if not all fractures in the fusion crust are filled by red rust deposits. Many other fractures within the sample interior are rust-filled as well. NNL stain can be found nearly everywhere (60.2 percent) with the exception of one small unaffected area. One concentrated region of OPL material, apparently a completely altered metal grain, is connected by a rust-lined fracture to the exterior. The sample contains many examples of well crystallized OPL phases (9.4 percent calculated modal abundance), characterized by their highly transparent interiors under crossed nicols.

Other notable features include amorphous oxide deposits (identified by their opaque, downy appearance), kink banding

in an olivine chondrule fragment, cleavage controlled stain distributions in a pyroxene chondrule, and blackening near the fusion crust.

The Smithsonian chip LEW86015,0 has very similar features, including red rust deposits in the fusion crust, a high NNL stain density (but having a dark orange-brown color), and well crystallized OPL deposits.

CARICHIC H-5

Carichic is an example of a highly weathered non-Antarctic meteorite. Most details are obscured by intense oxide staining and alteration. Highly altered areas between chondrules and crystals larger than matrix-sized particles are nearly or entirely opaque and indistinguishable from metal and metal sulfide particles. Also most every transparent crystal and chondrule is saturated with cloudiness.

The specimen is moderately fractured with most fractures being filled with opaque oxides. Interiors of many chondrules and chondrule fragments have been inundated by orange-brown oxides. Others are altered parallel to radial pyroxene or barred olivine plates. Chondrule varieties recognized include granular olivine with subrounded grains, $^{1}/_{3}$ to 1 mm in diameter, barred olivine, excentroradial pyroxene 0.33 to 1.25 mm in diameter, microporphyritic olivine with euhedral, randomly oriented olivine lozenges set in a matrix of either (1) fine grained and small rounded olivine, or (2) cryptocrystalline pyroxene with randomly oriented pyroxene plates, 0.25 to 4.7 mm in diameter. One olivine crystal is almost 2.0 mm in length. A barred olivine chondrule fragment exhibits sweeping extinction. Two subparallel shock veins penetrate and transect the specimen. Euhedral olivine crystals in one large

microporphyritic chondrule appear embayed, suggesting partial re-equilibration at lower temperatures.

Examining the Carichic thin sections in reflected light reveals zones of darker staining within which reduced metal grains cannot be found. Outside these zones, metal grains of varying sizes can be seen in abundance (refer to Figure 3.21).

APPENDIX B

DESCRIPTIVE CATALOGUE OF COLOR TRANSPARENCIES

APPENDIX B

DESCRIPTIVE CATALOGUE OF COLOR TRANSPARENCIES

ALHA81031,19; L3

10;XN;2.5/.008
Wide field shot showing heterogeneous texture of this petrologic type 3 UOC.

11;PL;2.5/.008
Same view in plane polarized light. Fine-grained dark matrix outlines chondrules. Chondrule types are highly varied.

12;XN;6.3/.20
Pyroxene chondrule with well defined platelets and sharp outline.

13;PL;6.3/.20
Same view in plane polarized light. OPL visible in upper left corner of frame.

14;XN;6.3/.20
Excentroradial pyroxene chondrule.

15;PL;6.3/.20
Same view in plane polarized light.

16;XN;6.3/.20
Plagioclase feldspar in chondrule pair.

17;PL;6.3/.20
Same view in plane polarized light. Feldspar grains appear hexagonal in outline and are difficult to distinguish from euhedral olivine grains in plane polarized light.

18;XN;6.3/.20
Cryptocrystalline excentroradial pyroxene chondrule is crosscut by NNL-filled fractures.

19;PL;6.3/.20
Same view in plane polarized light.

20;XN;6.3/.20
Black-rimmed granular chondrule.

21;PL;6.3/.20
Plane polarized light view displays black rim more clearly than polarized view.

22;XN;6.3/.20
Granular olivine chondrule.

23;PL;6.3/.20
Same view in plane polarized light.

24;XN;6.3/.20
Chondrule contains a grain which appears to have weathered in a boxwork pattern, and also exhibits possible evidence for direct (transformation) weathering of primary to secondary phases. To be noted in this view is that all rust-filled fractures, which crosscut the grain at subparallel angles, are simultaneously highly light-transmissive.

25;PL;6.3/.20
Same view in plane polarized light. Boxwork pattern in grain at lower right of frame is pronounced.

26;XN;16/.45
This image is part of a 2-slide sequence intended to demonstrate against the assertion of transformation in this case. This view shows several pyroxene grains with rust fillings in cleavage planes "lighting up" in optical continuity, as would be expected from the transformed weathering of different regions in a single primary crystal.

27;PL;16/.45
Same view in plane polarized light.

28;XN;16/.45
Rotated 47°, most all of the previously light-transmissive cleavage plane regions go extinct. A transformation weathering mechanism would explain this process only if occurring within cleavage planes of a single crystal.

29;PL;16/.45
Same view in plane polarized light.

30;XN;40/.70
Highly magnified view of cleavage plane and fracture fillings.

31;PL;40/.70
Same view in plane polarized light.

32;XN;40/.70
Rotation of stage show simultaneous illumination of parallel, crystalline cleavage plane fillings.

33;PL;40/.70
Same view in plane polarized light.

34;XN;16/.45
Two different cleavage sets "light up" within pyroxene crystal.

35;PL;16/.45
Same view in plane polarized light.

36;XN;6.3/.20
Rotated boxwork slide.

37;PL;6.3/.20
Same view in plane polarized light.

ALHA77230,48; L4

01;XN;2.5/.008
Wide field view showing general texture and weathering intensity.

03;PL;2.5/.008
Same view in plane polarized light.

04;XN;6.3/.20
Pyroxene chondrule with unusual fracture/strain pattern.
Extinction sweeps as stage rotates.

05;PL;6.3/.20
Same view in plane polarized light.

06;XN;2.5/.008
Microporphyritic chondrule with interchondrule microfault.

07;PL;2.5/.008
Same view in plane polarized light.

08;XN;6.3/.20
Higher magnification shows extent of microfault.

09;PL;6.3/.20
Same view in plane polarized light.

10;XN;16/.45
This grain appears to contain large etch pits.

11;PL;16/.45
Possible pitting is more pronounced in plane polarized light.

12;XN;40/.70
Pits appear to be free of secondary deposits, are elongated at nearly right angles to visible cleavage planes, and exhibit

consistent polygonal geometries which become more distinct with increasing dimensions.

13;PL;40/.70
This plane polarized light view shows the high relief of the pit areas, which occupy zones at different levels within the crystal as evidenced by focusing adjustments.

14;XN;16/.45
Another example of possible etch pitting within the same microporphyritic chondrule. Pits cover a large percentage of the visible crystal surface.

15;PL;16/.45
Pits are more readily discernible in plane polarized light than in polarized light.

16;XN;40/.70
Higher magnification reveals features with similar outlines to those of the previous slide series.

17;PL;40/.70
Same view in plane polarized light.

18;XN;6.3/.20
Granular olivine chondrule with clouded crystals.

19;PL;6.3/.20
Same view in plane polarized light.

20;XN;16/.45
Higher magnification reveals extent of clouding.

21;PL;16/.45
Plane polarized light view. Clouding pattern is not homogeneous but occupies preferential zones along grain boundaries and seemingly random zones within grains.

22;XN;2.5/.008
Fusion crust contains a higher relative abundance of OPL oxide than most areas within specimen.

23;PL;2.5/.008
Same view in plane polarized light.

24;XN;6.3/.20
Higher magnification of same area centered on fusion crust.

25;PL;6.3/.20
Same view in plane polarized light.

26;XN;2.5/.008
Beginning of zoom-in sequence on possible pitting within cryptocrystalline pyroxene chondrule.

27;PL;2.5/.008
Same view in plane polarized light. Thinning of microprobe mount toward edge of specimen is apparent.

28;XN;6.3/.20
Higher magnification of chondrule rim.

29;PL;6.3/.20
Same view in plane polarized light.

30;XN;16/.45
Still higher magnification shows linearity of pit feature patterns.

33;PL;40/.70
Linear pit feature patterns at high magnification.

34;XN;100/1.32
Same features at very high magnification.

35;PL;100/1.32
Same view in plane polarized light.

36;XN;16/.45
Elongated pit features in pyroxene chondrule fragment.

37;XN;16/.45
Duplicate view, but slightly more transparent.

38;PL;16/.45
Outline of chondrule fragment delineated by NNL deposits.

39;XN;40/.70
Higher magnification of same chondrule fragment showing linearity of pit features.

40;PL;40/.70
Same view in plane polarized light.

41;XN;100/1.32
Very high magnification of pitted crystal.

42;PL;100/1.32
Same view in plane polarized light.

43;XN;6.3/.20
Barred olivine chondrule fragment with oxide stain between platelets.

44;PL;6.3/.20
Same view in plane polarized light.

45;XN;16/.45
Higher magnification centered on chondrule fragment.

46;PL;16/.45
Plane polarized light view shows distribution of oxides along avenues between platelets.

47;XN;6.3/.20
Wide field view of large (> 3 mm) clouded cryptocrystalline pyroxene chondrule.

48;PL;6.3/.20
Plane polarized light view shows pyroxene chondrule to be highly clouded.

49;XN;16/.45
Another pyroxene chondrule fragment exhibits clouding in linear patterns.

50;PL;16/.45
Same view in plane polarized light.

ALHA81027,26; L6

02;PL;6.3/.20
Void spaces partially filled with amorphous oxide phase. The rest of the meteorite is highly stained with NNL.

03;XN;16/.45
Magnified view centered on oxide-filled void showing partial crystallinity.

04;PL;16/.45
Same field in plane polarized light shows encroaching oxide filling void space.

05;XN;16/.45
Another example at the same magnification. Notice linear trends within crystallized zones paralleling grain boundaries. Amorphous oxide can be seen from secondary reflected light partially filling void space.

06;PL;16/.45
Same field in plane polarized light.

07;XN;6.3/.20
OPL near edge of specimen.

08;PL;6.3/.20
Same view in Plane polarized light. Material nearly surrounds one opaque grain.

09;XN;16/.45
Magnified view centered on fractured opaque grain. Attack of alteration proceeds similar to classical "soil horizon

formation on bedrock" scheme. This suggests a mechanical breakdown of metal grains may accompany and assist chemical alteration progression, or that oxidation is simply taking advantage of an existing fracture situation.

10;PL;16/.45
Plane polarized light view of same field showing more clearly the "edge toward interior" progression of weathering. Fractures are parallel and perpendicular weathering "front".

ALHA77004,22; H4

01;XN;2.5/.008
Wide field view showing general oxide stain intensity. Note: Oxide stain intensity decreases toward microprobe mount edge due to thinning of specimen.

03;PL;2.5/.008
Same view in plane polarized light.

04;XN;6.3/.20
Vein fillings in highly fractured chondrule fragment.

05;PL;6.3/.20
Same view in plane polarized light.

06;XN;16/.45
Microfaulted barred olivine chondrule. Platelets exhibit interesting symmetry.

07;PL;16/.45
Same view in plane polarized light. Some preferential staining of glass areas has occurred.

08;XN;6.3/.20
OPL zone surrounding void space.

09;PL;6.3/.20
OPL distribution and void space more visible in plane polarized light than in polarized light.

10;XN;16/.45
Higher magnification of same area centered on OPL oxide and void space. Space appears to have once been occupied by opaque grain which may have been plucked during or preceding mounting process.

11;PL;16/.45
Features are more visible in plane polarized light.

12;XN;6.3/.20
Irregular glass patterns in olivine chondrule.

13;PL;6.3/.20
Same view in plane polarized light. Another void space is visible adjacent to chondrule.

14;XN;16/.45
Higher magnification of same area centered on chondrule.

15;PL;16/.45
Glass areas appear highly stained in plane polarized light, suggesting glass as probable source for iron during weathering.

16;XN;40/.70
Preferential weathering of glass zones apparent at high magnification. Some clouding of adjacent areas appears to have taken place.

17;PL;40/.70
Same view in plane polarized light.

18;XN;16/.45
Clouded pyroxene chondrule.

19;PL;16/.45
Same view in plane polarized light.

20;XN;40/.70
Higher magnification shows linear parallel and subparallel patterns in clouded areas.

21;PL;40/.70
Patterns are more strongly pronounced in plane polarized light.

22;XN;16/.45
Triangular features resembling indentations or pits in pyroxene grain.

25;PL;40/.70
High magnification view of triangular features in plane polarized light.

26;XN;16/.45
Barred olivine chondrule.

27;PL;16/.45
Same view in plane polarized light.

28;XN;16/.45
Oxides found not in association with any remaining opaque phases.

29;PL;16/.45
Plane polarized light view of same area shows clean contact with silicate phases.

30;XN;40/.70
Higher magnification shows internal structure of oxide.

31;PL;40/.70
Patterns may be related to primary crystal structure prior to replacement. Contact with silicate phases is irregular.

32;XN;6.3/.20
Microporphyritic olivine chondrule.

33;PL;6.3/.20
Same view in plane polarized light. Matrix is highly stained.

34;XN;40/.70
Stained and/or altered matrix appears glassy.

35;PL;40/.70
Same view in plane polarized light.

36;XN;40/.70
Another view of same chondrule shows linear clouding patterns in silicate grain.

ALHA77208,29; H4

01;XN;16/.45
Intercrystal oxide nodules.

02;PL;16/.45
Plane polarized light view shows intense staining in vicinity of this chondrule. Nodules may be superimpositions of material over crystal due to manipulation of oxide fragments during mount preparation.

03;XN;16/.45
Teardrop shaped features resembling etch pits.

04;PL;16/.45
Features are more pronounced in plane polarized light. Features line up at oblique angles to visible cleavage planes.

05;XN;16/.45
Oxide-filled fractures.

06;PL;16/.45
Plane polarized light reveals oxide to appear similar to OPL material, but without being well crystallized.

07;XN;6.3/.20
Partially stained pyroxene chondrule fragment.

08;PL;6.3/.20
Plane polarized light view shows extensive oxide deposition adjacent to chondrule fragment.

09;XN;16/.45
Higher magnification of area centered on chondrule fragment showing relative clarity of interchondrule region as compared with high staining of surrounding region.

10;PL;16/.45
Same view in plane polarized light.

11;XN;16/.45
Partially crystallized OPL material filling fractures throughout highly fractured crystal assemblage.

14;PL;16/.45
Detail of OPL from photomicrograph number 07. Opaque areas seem to be weathering from the inside out in this plane of visibility. Red zones exhibit sweeping extinction in polarized light.

26;XN;2.5/.008
Wide field view showing general character of sample.

27;PL;2.5/.008
Same view in plane polarized light.

28;XN;2.5/.008
Widespread oxide deposition along boarder of large void space.

29;PL;2.5/.008
Plane polarized light view shows delicate nature of amorphous oxide material.

30;XN;6.3/.20
Detail of OPL distribution along void space boarder. Variable crystallinity characterizes the material in this area.

31;PL;6.3/.20
Same view in plane polarized light.

32;XN;6.3/.20
Oxides completely surround but do not penetrate small, transparent grains.

33;PL;6.3/.20
Same view in plane polarized light. Note fractures only partially filled with oxide material, possibly suggesting recent, post-oxide-deposition development of fracture widening followed by further oxide formation and deposition.

34;XN;16/.45
Same area under higher magnification.

35;PL;16/.45
Same view in plane polarized light.

ALHA77225,18; H4

02;XN;2.5/.008
Wide field view showing general character of specimen.

03;PL;2.5/.008
Same view in plane polarized light. Many examples of OPL can be recognized.

04;XN;6.3/.20
Granular olivine chondrule with euhedral crystals. Olivine crystals can be identified by morphology. First order gray birefringence colors suggest nonstandard thickness for microprobe mount.

05;PL;6.3/.20
Same view in plane polarized light. Chondrule is partially bordered by OPL blebs.

06;XN;6.3/.20
Pyroxene chondrule surrounded by altered opaque material.

07;PL;6.3/.20
Distribution of OPL is more clearly discerned in plane polarized light. Note that OPL appears restricted to zones between crystals and does not penetrate the chondrule boarder except along one fracture.

08;XN;16/.45
Higher magnification of same area centered on chondrule. An oxide-filled fracture with a curious "zig-zag" pattern, apparently corresponding to cleavage planes, can be seen; as well as many well-crystallized OPL blebs in association with opaque phases.

09;PL;16/.45
Same view in plane polarized light. Former outlines of opaque grains can be seen.

10;XN;16/.45
Partially devitrified glass.

11;PL;16/.45
Same view in plane polarized light.

12;XN;16/.45
Secondary oxide products in *en echelon* arrangement within strained pyroxene grain.

13;PL;16/.45
Same view in plane polarized light.

14;XN;16/.45
As the grain is rotated, fracture fillings go extinct simultaneously, suggesting possibility of *in situ* transformation of primary crystal to secondary products.

15;PL;16/.45
Same view in plane polarized light.

16;XN;6.3/.20
Beginning of zoom-in sequence of detail of OPL alteration products in association with opaque phases.

17;PL;6.3/.20
Same view in plane polarized light. Large open space exists as result of separation along fracture during mounting operations.

18;XN;16/.45
Well crystallized OPL surrounding opaque grains.

19;PL;16/.45
Same view in plane polarized light.

20;XN;40/.70
At high magnification, details of crystal structure can be observed in the OPL material.

21;PL;40/.70
Plane polarized light view shows OPL oxides to exhibit botryoidal crystal habit. Material appears to be expanding into vacant spaces and may thus have formed following or just previous to mount preparation.

22;XN;6.3/.20
Granular olivine chondrule outlined by oxide deposits.

23;PL;6.3/.20
Same view in plane polarized light.

24;XN;16/.45
Same chondrule under higher magnification.

25;PL;16/.45
Same view in plane polarized light.

ALHA77226,37; H4

01;XN;2.5/.008
Wide field view showing general rust intensity of specimen.

02;PL;2.5/.008
Same view in plane polarized light.

03;XN;2.5/.008
Fracture fillings.

04;PL;2.5/.008
Plane polarized light view of same field showing extent and width of fracture.

05;XN;6.3/.20
Higher magnification of fracture zone.

06;PL;6.3/.20
Fracture presumably widened during mount preparation. However, very little if any post-mount deposition is visible.

07;XN;16/.45
OPL along fusion crust. Very well crystallized.

08;PL;16/.45
Definite color differences between the opaque-associated OPL and the fusion crust OPL can be seen in this plane polarized light view of the same field.

09;XN;6.3/.20
Another example of OPL along fusion crust.

10;PL;6.3/.20
Same view in plane polarized light.

11;XN;2.5/.008
Well developed crystal structure in OPL material.

12;PL;2.5/.008
Same view in plane polarized light.

13;XN;6.3/.20
Same area under higher magnification. A glass-filled fracture zone is visible running diagonally across the frame.

14;PL;6.3/.20
Same view in plane polarized light.

15;XN;16/.45
Higher magnification view centered on OPL-dominated region.

16;PL;16/.45
Glassy areas are visible in plane polarized light view.

17;XN;16/.45
Many features and feature associations are visible in the area dominated by the glass-filled fracture. Some devitrification is present.

18;PL;16/.45
The plane polarized light view shows bubbles within the glass zone which are filled with oxide weathering products.

19;XN;6.3/.20
Pyroxene chondrule with unusual linearities suggesting removal of silicate material and subsequent filling with oxide products.

20;PL;6.3/.20
Same view in plane polarized light.

21;XN;6.3/.20
Interchondrule features resembling recrystallization within tension fractures.

23;XN;16/.45
Same chondrule under higher magnification.

24;PL;16/.45
Same view in plane polarized light.

25;XN;6.3/.20
Interchondrule devitrification.

26;PL;6.3/.20
Same view in plane polarized light.

27;XN;16/.45
Higher magnification of devitrification area.

28;PL;16/.45
Same view in plane polarized light.

29;XN;16/.45
Zoned inclusion within clouded pyroxene chondrule fragment.

30;PL;16/.45
Same view in plane polarized light.

31;XN;40/.70
Same chondrule under higher magnification.

34;PL;2.5/.008
Wide angle view of specimen centered on fusion crust.

ALHA77232,16; H4

18;PL;2.5/.008
Pyroxene chondrule rimmed with iron oxides.

19;XN;2.5/.008
Same view in polarized light. Many different chondrule types can be identified in this view.

20;PL;16/.45
Higher magnification of chondrule rim showing oxides lining rim boarder, and in association with adjacent opaque phases. A smooth transition appears to be in progress from *in situ* alteration of opaque material to OPL oxides, to neoformation along nearby avenues of constituents in solution to NNL material.

21;XN;16/.45
Under polarized light, the transition boundary from NNL to OPL phases can be discerned. The OPL material is well crystallized and close to the opaque phases. By contrast, the NNL material is poorly crystallized and is found farther along the matrix/chondrule contact from the opaque iron source.

22;PL;16/.45
This appears to be brecciated pyroxene crystal fragments set within a devitrified glass groundmass.

23;XN;16/.45
Under crossed nicols, devitrification appears far less extensive.

24;PL;40/.70
Higher magnification reveals groundmass to exhibit clouding in parallel linear arrangement. This view is centered on a crystal fragment which appears to be in the process of alteration by chemical attack from selected sides.

25;XN;40/.70
Same view in polarized light. Parallel arrangements are clearly visible.

26;PL;40/.70
Another example in same area. Weathering "fronts" render crystal boundaries irregular and indistinct.

27;XN;40/.70
In polarized light, however, it becomes difficult to assert whether crystal boundaries are indeed being attacked, or are simply partially overlapped by NNL.

28;PL;16/.45
Pyroxene chondrule fragment appears to have suffered offset along fracture.

29;XN;16/.45
Same view in polarized light. Offset more clearly pronounced, but is brought into question by apparent continuations of platelets across fracture.

30;PL;16/.45
Example of amorphous oxide material surrounding void space.

31;XN;16/.45
The amorphous nature of the material is evident under crossed nicols.

32;PL;16/.45
Glass region exhibiting what appears to be devitrification followed by alteration in a striking pattern.

33;XN;16/.45
Pattern is more visible under crossed nicols.

34;PL;40/.70
Same region at greater magnification. Transverse patterns are parallel to subparallel.

35;XN;40/.70
Patterns are well pronounced in polarized light.

ALHA77233,21; H4

02;XN;6.3/.20
Olivine crystal-centered chondrule. Olivine crystal is clouded throughout a zone concentric with its perimeter.

03;PL;6.3/.20
Same view in plane polarized light. Transverse fractures crosscut chondrule, penetrating olivine crystal with little refraction.

04;XN;16/.45
Higher magnification reveals penetration of oxide phases into fractures. This process is apparently seen in an arrested state, as some fractures are only partly filled. Linear texture of clouded zone is evident.

05;PL;16/.45
Same view in plane polarized light. Olivine crystal is relatively stain-free, in contrast to highly stained surrounding area.

06;XN;16/.45
Microporphyritic olivine chondrule containing crystals which display features resembling etch pitting.

07;PL;16/.45
Plane polarized light view.

08;XN;40/.70
Magnified view of same chondrule centered on pitted grain. Features are linear and parallel. High relief of features suggests hollow pits.

09;PL;40/.70
Features are more discernible in plane polarized light than in polarized light.

10;XN;16/.45
Opaque grains in association with partially crystallized OPL material.

11;PL;16/.45
Plane polarized light view. Full extent of OPL material is visible.

12;PL;6.3/.20
Dark-zoned chondrule.

13;XN;6.3/.20
Dark-zoned chondrule in polarized light.

14;PL;16/.45
Mineral with 3 cleavage sets. Staining location is partially controlled by cleavage. Elongated features restricted to one select region and bounded by cleavage plane.

15;XN;16/.45
Same view in polarized light.

16;PL;100/1.32
Highly magnified view of crystal, centered on elongation patterns. Patterns are in subparallel linear arrangements, and exhibit bubble-like appearance.

17;XN;100/1.32
Same view in polarized light.

ALHA77182,36; H5

11;XN;2.5/.008
Wide field view of sample showing large excentroradial pyroxene chondrule with oxides occupying spaces between platelets.

12;PL;2.5/.008
Plane polarized light view of same field. Note that NNL is sparse in this sample.

13;XN;16/.45
Magnified view centered on chondrule. Clearly visible are linear deposits of red oxide which parallel pyroxene plates and terminate at a transverse zone.

14;PL;16/.45
Plane polarized light view of same field. Opaque phases can be found in association with the red trends, but it is difficult

to say with certainty whether these were the sole contributors or whether some alteration of the pyroxene itself might not have taken place.

15;XN;16/.45
Visible in these olivine chondrules are curious pits which line up in rows and interfere with light transmission, giving a cloudy appearance.

16;PL;16/.45
Plane polarized light view of same field. NNL fills cleavage planes or striations in one grain.

17;XN;16/.45
Barred olivine chondrule fragment with OPL invading former glass spaces.

18;PL;16/.45
Plane polarized light view of same field. OPL seems preferential for special conditions, not occupying all available spaces.

19;XN;16/.45
Another pyroxene chondrule with OPL taking advantage of crystal morphology, though to a lesser extent than with slides 11 through 14.

20;PL;16/.45
Plane polarized light view of same field. Visible in plane polarized light are void spaces which are partially filled with oxides of a botryoidal habit.

21;XN;16/.45
Another region of botryoidal void fillings. Not much is visible of these deposits under crossed polarizers.

22;PL;16/.45
Plane polarized light view of same field. Knobby, botryoidal deposits are visible in profusion.

23;XN;6.3/.20
Wide field view showing distribution of these deposits.

24;PL;6.3/.20
Plane polarized light view of same field.

25;XN;16/.45
Detail of previous slide set. Void space is rimmed with well crystallized phase, though apparently not associated with any nearby opaque grains, suggesting a three step process for the present appearance of these features: 1. OPL forms by in-situ alteration of opaque grain. 2. Grain to grain integrity is weakened by the softer oxide rim and the remaining opaque material is removed by plucking. 3. Additional residual growth of botryoidal phases occurs into new vacancy.

26;PL;16/.45
Plane polarized light view of same field.

27;XN;2.5/.008
Wide field view showing many large chondrules of various morphology.

28;PL;2.5/.008
Plane polarized light view of same field.

29;XN;16/.45
Barred olivine chondrule similar to that of slide pair 17/18. OPL can be seen entering vacancies between plates.

30;PL;16/.45
Plane polarized light view of same field. OPL has low mobility, but is clearly not immobile.

ALHA79025,16; H5

1b-4b;PL/XN;2.8/.008
Wide field views of devitrified glass.

5b-10b;PL/XN;6.3/.20
Medium power views of devitrified glass. Glass appears to be associated with (or part of) fusion crust.

11b;XN;16/.45
Devitrified glass appears moderately clouded.

12b;PL;16/.45
Same view in plane polarized light.

13b;PL;16/.45
Devitrified glass containing NNL stain.

14b;XN;16/.45
Same view in polarized light.

15b-18b;PL/XN;16/.45
Additional details of devitrified glass under high power. Sharp contact phases appear as coating superimposing glass in 17b and 18b.

19b;PL;40/.70
Very high power view of devitrified glass.

20b;XN;40/.70
Same view in polarized light.

21b;PL;16/.45
Partially recrystallized grain?

22b;XN;16/.45
Same view in polarized light.

23b;PL;16/.45
OPL in association with opaque grains.

24b;XN;16/.45
Same view in polarized light.

31;XN;6.3/.20
Microporphyritic olivine chondrule with one large olivine grain displaying linear clouding.

32;PL;6.3/.20
Same view in plane polarized light. Surrounding material stained.

33;XN;16/.45
High magnification of same chondrule centered on large grain. Clouding tends to avoid grain boundaries and inclusions. Could the chemistries of these areas have been altered by the presence of inclusions and other grains, sufficient to reduce susceptibility to attack by weathering agents?

34;PL;16/.45
Same image in plane polarized light.

35;XN;2.5/.008
Wide field view of meteorite. Visible are several chondrule types. One barred olivine chondrule exists within larger, opaque-centered granular chondrule.

36;PL;2.5/.008
Same field in plane polarized light. Notice distribution of opaque phases associated with OPL and NNL phases.

ALHA79029,21; H5

01;XN;6.3/.20
Unusual clouded pattern in pyroxene chondrule fragment.

02;PL;6.3/.20
Same view in plane polarized light. Chondrule fragment is almost totally free of staining, in contrast to surrounding regions.

03;XN;16/.45
Symmetry of clouded areas becomes clear at higher magnification. Area appears highly pitted, with pit features arranged in linear parallel and subparallel arrangements along intermittent transverse stripes across the fragment.

04;PL;16/.45
High relief of clouded verses non-clouded areas is more visible in plane polarized light than in polarized light.

05;XN;6.3/.20
Microporphyritic olivine chondrule.

06;PL;6.3/.20
Same view in plane polarized light.

07;XN;16/.45
Under higher magnification, some pit features can be discerned.

08;PL;16/.45
A variety of pit features are present, from random clouding to polygons in linear arrangements.

09;XN;6.3/.20
Clouded pyroxene chondrule fragment.

10;PL;6.3/.20
More features are visible in plane polarized light than in polarized light. Fragment contains linear zones of higher opaque grain concentration, which seem to be relatively cloud-free, in contrast to surrounding regions of high clouding.

11;XN;16/.45
Higher magnification shows features more clearly. Chondrule fragment is shot through with oxide-filled fractures.

12;PL;16/.45
Same view in plane polarized light.

13;XN;6.3/.20
Pyroxene chondrule with pit features.

14;PL;6.3/.20
Same view in plane polarized light.

15;XN;2.5/.008
Wide field view showing general rustiness of specimen.

16;PL;2.5/.008
Same view in plane polarized light.

17;XN;2.5/.008
Wide field view of less rusty area. The two slide sets are intended to illustrate the heterogeneity of rustiness encountered within specimens.

18;PL;2.5/.008
Same view in plane polarized light.

22;PL;16/.45
Microporphyritic pyroxene chondrule with polygonal pit features of varying size. Altered material (which could be glass) is visible.

23;XN;40/.20
Detail of above. Note hint of stairstep pattern to pit outlines.

24;PL;40/.20
Same view in plane polarized light.

25;XN;40/.70
Well pronounced pit features of polygonal outline.

26;PL;40/.70
Same view in plane polarized light. Some pits seem to have been filled with oxide phases.

27;XN;16/.45
Barred olivine chondrule.

28;PL;16/.45
Glassy zones appear to be partially weathered.

29;XN;40/.70
The cause for the "cloudy" appearances observed is revealed in this sequence of slides as a bubble or pit which occurs internally and not necessarily in association with a fracture. Focus changes in this sequence will show that these features are found at varying depths within a given crystal. Pit features in focus at southwest side of "cloud".

30;PL;40/.70
Same view in plane polarized light.

31;XN;40/.70
Pit features in focus toward the northeast side of "cloud".

32;PL;40/.70
Same view in plane polarized light.

33;XN;16/.45
Wider field of view showing surrounding cloudy regions.

34;PL;16/.45
Clouding is more visible in plane polarized light than in polarized light.

35;PL;6.3/.20
Still wider field of view.

36;XN;6.3/.20
Same view in polarized light.

ALHA84075,7; H5

02;XN;16/.45
Pyroxene crystal with rust-filled fractures and cleavage planes. Common illumination of these fractures will occur upon rotation of stage, visible in following slide pair.

03;PL;16/.45
Cleavage planes are visible in plane polarized light.

04;XN;16/.45
Same crystal rotated 40.5° clockwise. Cleavage plane fillings now transmit light, while fracture filling goes extinct.

05;PL;16/.45
Same view in plane polarized light.

06;XN;6.3/.20
Same area at lower magnification, centered on crystal.

07;PL;6.3/.20
Same view in plane polarized light.

08;XN;6.3/.20
Same view rotated 80°.

09;PL;6.3/.20
Same view in plane polarized light.

10;XN;6.3/.20
OPL apparently not in association with opaques.

11;PL;6.3/.20
Same view in plane polarized light.

12;XN;16/.45
Higher magnification view centered on OPL material.

13;PL;16/.45
Same view in plane polarized light.

14;XN;16/.45
Pyroxene grain with inclusions.

15;PL;16/.45
Same view in plane polarized light.

16;XN;16/.45
Same view rotated 43°.

17;PL;16/.45
Same view in plane polarized light.

18;XN;16/.45
Another example of possible transformation.

19;PL;16/.45
Same view in plane polarized light. OPL in association with opaque phases.

20;XN;16/.45
Same view rotated 43°. Cleavage and fracture zones both transmit.

21;PL;16/.45
Same view in plane polarized light.

22;XN;16/.45
Olivine grains show same phenomenon as pyroxene grains.

23;PL;16/.45
Same view in plane polarized light.

24;XN;16/.45
Same view after rotation.

25;PL;16/.45
Same view in plane polarized light.

ALHA85025,10; H5

05;XN;2.5/.08
Wide field view showing regional texture and a rust-filled fracture.

06;PL;2.5/.08
Same view in plane polarized light. Increased contrast reveals fracture fillings more clearly than in polarized view. Pleochroic minerals visible in corners of view.

07;XN;6.3/.20
Magnified view of same region, centered on fracture zone.

08;PL;6.3/.20
Same view in plane polarized light showing dispersion of colors from fracture zone.

09;XN;9/.20
Dendritic features in chondrule.

10;PL;9/.20
Same view in plane polarized light. Many rust features visible in this large field view.

11;XN;16/.45
Magnified view centered on dendritic features. Features are opaque and are apparently confined to single crystal.

12;PL;16/.45
Same view in plane polarized light. The dendrite-containing crystal is stained orange throughout, except for central region which remains clear.

13;XN;6.3/.20
Association between fusion crust and rust features.

14;PL;6.3/.20
Plane polarized light view showing fusion crust altered throughout its extremity. Interior fractured zone heavily inundated with rust features.

15;XN;6.3/.20
Example of crystal with rust-filled fractures.

16;XN;6.3/.20
Identical to above.

19;PL;6.3/.20
Wide field view showing overall rust intensity.

20;XN;2.5/.08
Wide field view showing fusion crust weathering.

21;PL;2.5/.08
Same view in plane polarized light showing thickness of fusion crust. Comparison with previous slide reveals locations of glassy material in crust.

22;XN;16/.45
Clouded or pitted crystal in association with iron oxide staining. Note that only a portion of the crystal has been effected.

23;PL;16/.45
Same view in plane polarized light. Association with oxides may be coincidental.

24;XN;16/.45
Well crystallized OPL in fractures.

25;PL;16/.45
Same view in plane polarized light. Texture is well integrated, suggesting that oxide location is dependent on avenue communication.

26;XN;16/.45
Partially clouded grain.

27;PL;16/.45
Same view in plane polarized light. Clouding is not extensive.

28;XN;16/.45
Same grain rotated to show internal optical property of clouded region. Region is seen to become transmissive at certain orientations between crossed polarizers.

29;PL;16/.45
Effect is not visible in plane polarized light.

30;XN;40/.70
Bubbles with irregular outlines are common throughout all samples examined. They concentrate along fracture planes and appear associated with NNL.

31;PL;40/.70
Same view in plane polarized light.

32;XN;40/.70
Elongated and subrectangular features in olivine crystal.

33;PL;40/.70
Same view in plane polarized light. Features do not appear to be associated with any rust phases.

34;XN;100/1.32
Highly magnified view of features.

35;PL;100/1.32
Same view in plane polarized light. Becke line visible.

ALHA77271,28; H6

02;PL;16/.45
Pronounced clouding in zone within olivine grain concentric with grain boundary.

03;XN;6.3/.20
Group of ≥ 7 clouded olivine grains of irregular outline.

04;PL;6.3/.20
Group of ≥ 7 clouded olivine grains of irregular outline. Clouding is more obvious in plane polarized light.

05;XN;16/.45
Group of clouded olivine grains of irregular outline (magnified view of same grouping). Clouding seems to concentrate within grain interiors.

06;PL;16/.45
Same view in plane light. Area is relatively free of rust staining, though some staining and red rust is visible in corner of frame.

07;XN;40/.70
Group of clouded olivine grains of irregular outline (highly magnified view of same grouping showing choice example). Clouding clearly concentrated along linear trends.

08;PL;40/.70
Linear trends are more easily discernible in plane polarized light.

09;XN;6.3/.20
Example of red rust in association with opaque grains, but removed some distance from them. Rust lines and partially fills void spaces.

10;PL;6.3/.20
Void spaces clearly defined in plane polarized light. Rust color variations from deep red to light orange.

11;XN;16/.45
Example of red rust in association with opaque grains (magnified view of same region). Details of red rust clearly defined.

12;PL;16/.45
Same view in plane light. High relief of void space perimeters apparent.

13;XN;6.3/.20
Rust deposits lining void spaces in botryoidal habit. Heterogeneity of chondrite grain size distribution obvious.

14;PL;6.3/.20
Plane polarized light view.

15;XN;16/.45
Rust deposits lining void spaces in botryoidal habit. Magnified view centered on void spaces.

16;PL;16/.45
Same view in plane light. Botryoidal product habit apparent. In focus verses out of focus areas along void perimeter show depth of field.

17;PL;40/.70
Highly magnified view of void space in plane polarized light showing knobby, bubble-like or botryoidal habit and bringing the idea of silicate replacement into question by virtue of irregular (attacked?) silicate void space perimeter. More likely the overlapping of product onto silicate material. View has relatively large depth of field.

18;XN;40/.70
Cross polarized view of highly magnified void space showing crystallinity of rust deposits.

19;XN;6.3/.20
Red rust in association with opaque phases, possibly replacing these phases.

20;PL;6.3/.20
Plane polarized light view of same area.

21;XN;16/.45
Magnified view of same region centered on red rust/opaque phase combination.

22;PL;16/.45
Same field in plane polarized light.

23;XN;40/.70
Highly magnified view showing eroded opaque boundaries and "seepage" of secondary phase overtop opaque primary. Notice silicate phases remain unaffected.

24;PL;40/.70
Plane polarized light view of same image.

25;XN;6.3/.20
Best example found of well crystallized alteration products, near fusion crust. Other, less impressive examples can be seen nearby.

26;PL;6.3/.20
Plane polarized light view of same area. Visible are areas of blackened fusion crust.

27;XN;16/.45
Magnified view centered on best crystallized product. Sweeping extinction evident. Vivid color and textural variations. Botryoidal habit. Seems to have completely or near completely replaced primary phases.

28;PL;16/.45
Other subtle features are revealed in this plane polarized light view of the same field. Silicates appear unaffected. Opaques in corner are being replaced. Alteration begins at the edges of opaque phase grains.

29;XN;40/.70
Highly magnified view centered on same association. "Weathering fronts" can be seen clearly and are concentric with respect to silicate and opaque grain boundaries. This image should be studied for clues as to phase origin and materialization.

30;PL;40/.70
Plane polarized light view of same field. Some remnant opaque material persists with highly sutured edges. Material appears from these remnants to have almost completely replaced a former opaque-occupied area with little or no net volume increase in the plane of the image. Ghost outlines (pseudomorphs?) can be discerned within the material.

31;PL;6.3/.20
Detail of weathering in fusion crust. Many color variations are present among similar mineralogies.

32;XN;6.3/.20
Same field of view under crossed polarizers. Variations in birefringence colors are striking.

33;XN;16/.45
Higher magnification centered on area of greatest alteration product concentration. Much dark material obscures details within OPL phases.

34;PL;16/.45
Same field under plane polarized light. Color variations change with thinning toward probe mount edge. Some botryoidal void filling is in progress near edge of field.

35;PL;40/.70
Highly magnified view centered on fusion crust alteration. Are these products of altered silicates, glass or metal?

36;XN;40/.70
Crossed polarized view of same field.

ALHA77288,34; H6

01;XN;2.5/.008
Wide field view showing cluster of clouded olivine crystals. Variations in birefringence due to thickness changes are apparent in one fractured grain.

02;PL;2.5/.008
Same view in plane polarized light.

03;XN;6.3/.20
Higher magnification of same area centered on clouded crystal group. Some linearity is visible at this scale in select grains.

04;PL;6.3/.20
Same view in plane polarized light.

05;XN;16/.45
Higher magnification shows rows of lenticular shapes which resemble etch pitting. Other clouding appears more random.

06;PL;16/.45
Same view in plane polarized light.

07;XN;16/.45
Pyroxene chondrule displaying striking color variations.

08;PL;16/.45
Plane polarized light view shows some pleochroism. Dark material between crystal plates does not seem to have been attacked preferentially by weathering reactions.

26;XN;6.3/.20
Extinct grain contains highlights which reflect crystal structure in NNL.

27;PL;6.3/.20
Concentric patterns suggestive of crystallinity are apparent in plane polarized light.

28;XN;16/.45
Higher magnification better defines crystal pattern.

29;PL;16/.45
Same view in plane polarized light.

30;XN;16/.45
Grain is rotated 47° to reveal effect of superimposed olivine crystal on birefringence coloration of NNL crystals. Crystallization appears incipient, in contrast to the sharply defined, well crystallized red and orange region to the lower right of the frame. Crystallization also appears to be occurring in optical continuity throughout specimen.

31;PL;16/.45
Same view in plane polarized light.

32;XN;6.3/.20
Chondrule containing platelets of opaque material.

33;PL;6.3/.20
Platelets do not seem to be attacked preferentially in plane polarized light.

34;XN;6.3/.20
Moderately metamorphosed barred olivine chondrule.

35;PL;6.3/.20
Plane polarized light examination shows that NNL material has entered the chondrule, but does not seem to have taken advantage of intergrain avenues.

36;PL;2.5/.008
Wide field view showing overall rust intensity.

37;XN;2.5/.008
Same view in polarized light.

ALHA84082,9; H6

01;XN;6.3/.20
Granular chondrule with clouded and rust-stained center.

02;PL;6.3/.20
Plane polarized light view of same region.

03;XN;16/.45
Enlarged image showing textural and mineralogical differences between chondrule center and outer rim.

04;PL;16/.45
Same view in plane polarized light showing preferential locations both of clouding and of oxide staining.

05;XN;6.3/.20
Olivine chondrule displays preferred oxide deposition along plate interstices. Wide field view.

06;PL;6.3/.20
Same view in plane polarized light.

07;XN;16/.45
Enlarged view centered on olivine grain. Plates can clearly be discerned.

08;PL;16/.45
Same view in plane polarized light. Avenues of oxide deposition can be identified.

09;XN;6.3/.20
NNL in fusion crust with OPL surrounding metal grains.

10;PL;6.3/.20
Same view in plane polarized light. NNL lines inside of void spaces. Possibly altered glassy material.

11;XN;16/.45
Magnified view centered on OPL-lined void spaces. Well cryptocrystallized.

13;PL;16/.45
NNL juxtaposed with OPL showing many interesting attributes of each.

14;XN;6.3/.20
Wider view of same area. Variations in OPL color may be due to density or thickness differences. Strong associative tendencies of OPL to opaque grains is evident here.

15;PL;6.3/.20
Plane polarized light view of same field.

LEW85332,11; H6

16;XN;6.3/.20
Void fillings with botryoidal growth habit.

17;PL;6.3/.20
Same view in plane polarized light. Broken fragment attests to pre-mount formation of fillings.

18;XN;16/.45
Higher magnification view centered on void spaces. High crystallinity is evident under crossed nicols.

19;PL;16/.45
Plane polarized light view of same field. Difficult to say whether isolated fragment is truly broken or simply a cross-section of a protrusion from the third dimension. Concentricity of growth "fronts" to outlines of silicate substrates evident.

20;XN;40/.70
High magnification view of pyroxene crystal with parallel rows of elongated or suborthogonal striations resembling etch pitting.

21;PL;40/.70
Same field in plane polarized light.

24;XN;16/.45
Granular chondrule surrounded by rust-lined void spaces.

25;PL;16/.45
Same view in plane polarized light.

26;XN;6.3/.20
NNL veins superimpose or cross-cut chondrule.

27;PL;6.3/.20
Same view in plane polarized light. Porosity of grain boundaries for fluid migration and chemical transport is evident in rust veins, which display a more tortuous or sutured formation

avenue than the often nearly straight formation habits of fracture fillings.

28;XN;16/.45
Enlarged view centered on chondrule.

29;PL;16/.45
Same view in plane polarized light.

30;XN;2.5/.08
Unusual fracture filling pattern near fusion crust.

31;PL;2.5/.08
Same view in plane polarized light.

32;XN;6.3/.20
Higher magnification. Fracture filling is well crystallized.

33;PL;6.3/.20
Plane polarized light view of same field. Fracture has moderate width.

34;XN;6.3/.20
Red rust grades to orange rust.

35;PL;6.3/.20
Plane polarized light view of same field.

36;XN;16/.45
Higher magnification of same field.

37;PL;16/.45
Plane polarized light field of same image.

01;XN;6.3/.20
Group of olivine crystals with clouding.

02;PL;6.3/.20
Plane polarized light view of same field.

03;XN;16/.45
Higher magnification centered on two large olivine grains. "Clouding" is actually parallel rows of something like etch pits.

04;PL;16/.45
Plane polarized light view of same field.

LEW86015,10; H6

01;XN;16/.45
OPL in fusion crust.

02;PL;16/.45
Same view in plane polarized light.

03;XN;6.3/.20
Another area of weathered fusion crust showing widespread crystallization in OPL phases.

04;PL;6.3/.20
Same view in plane polarized light.

05;XN;16/.45
Higher magnification of OPL zone. A well defined structure, paralleling outlines of associated opaque phases in intimate contact justify *in situ* formation and replacement conjecture.

06;PL;16/.45
Same view in plane polarized light.

07;XN;16/.45
Adjacent area at same magnification displaying similar features.

08;PL;16/.45
Same view in plane polarized light. Note black zones in crystal fractures near fusion crust.

09;XN;16/.45
Glass in a barred olivine chondrule fragment.

10;PL;16/.45
Same view in plane polarized light.

11;XN;2.5/.008
OPL material and associated fracture feed.

12;PL;2.5/.008
Same view in plane polarized light.

13;XN;6.3/.20
Same area under higher magnification, centered on opaque area.

14;PL;6.3/.20
Opaque area occupies void space in quasi-honeycomb pattern. Opaque material is amorphous oxide deposit.

15;XN;16/.45
Staining is visibly heterogeneous in this wide field view.

16;PL;16/.45
Heterogeneity is more visible in plane polarized light.

17;XN;6.3/.20
Close up view of arrested staining front.

18;PL;6.3/.20
Same view in polarized light.

19;XN;6.3/.20
Kink bands in olivine chondrule fragment.

20;PL;6.3/.20
Same view in plane polarized light.

21;XN;6.3/.20
There is very little glass in this fusion crust, possible due to weathering.

22;PL;6.3/.20
Same view in plane polarized light.

23;XN;16/.45
Unusual pattern of microvoid spaces in olivine chondrule, possibly a good example of pitting.

24;PL;16/.45
Same view in plane polarized light.

25;XN;6.3/.20
Stained boxwork cleavage in pyroxene chondrule. The stain distribution is cleavage controlled.

26;PL;6.3/.20
Stain control is more pronounced in plane polarized light.

27;XN;16/.45
Same crystal at higher magnification.

28;PL;16/.45
Same view in plane polarized light. Excellent example of NNL migration habits.

29;XN;2.5/.008
Rust vein and fracture filling extends to edge of meteorite, allowing direct avenue for fluid migration from surface to interior.

30;PL;2.5/.008
Same view in plane polarized light.

31;XN;6.3/.20
Higher magnification of oxide-filled fractures.

32;PL;6.3/.20
Same view in plane polarized light.

33;XN;16/.45
Very thin, well crystallized OPL material deposited along fusion crust surface.

34;PL;16/.45
Same view in plane polarized light.

35;XN;16/.45
Rectangular outline of well crystallized OPL as discrete zone surrounded on both sides by amorphous oxide material.

36;PL;16/.45
Same view in plane polarized light.

15B;XN;16/.45
Highly magnified view of amorphous oxides.

16B;PL;16/.45
Same view in plane polarized light.

17B;XN;2.5/.008
Zoom in sequence on blackening near fusion crust.

18B;PL;2.5/.008
Same view in plane polarized light. Blackened area more visible.

19B;XN;6.3/.20
Higher magnification of same area.

20B;PL;6.3/.20
Various zones within fusion crust are clear in plane polarized light.

21B;XN;6.3/.20
Iron oxide deposits near fusion crust.

22B;PL;6.3/.20
Same view in plane polarized light.

23B;XN;16/.45
Well crystallized to amorphous OPL material in association with opaque phases.

24B;PL;16/.45
Same view in plane polarized light.

25B;XN;16/.45
Another example of well crystallized and amorphous OPL material, some of which is growing into a void space.

26B;PL;16/.45
Same view in plane polarized light. Color variations are visible which are partially or entirely due to OPL phase thickness.

27B;XN;16/.45
Another example.

28B;PL;16/.45
Same view in plane polarized light.

29B;XN;16/.45
A wide variety of oxide details can be discerned in this view. Principal among these are thick NNL deposits, parallel fracture fillings, and well crystallized OPL material which has apparently consumed primary opaque material completely.

30B;PL;16/.45
Same view in plane polarized light.

31B;XN;16/.45
Another example opaque material in process of alteration.

32B;PL;16/.45
Same view in plane polarized light.

33B;XN;16/.45
Oblate massing of opaque particles.

34B;PL;16/.45
Opaque particles are more easily visible in plane polarized light.

35B;XN;40/.70
Amorphous oxide material in void space.

36B;PL;40/.70
Same view in plane polarized light. Repetition of LEW86015,10/15B and LEW86015,10/16B.

CARICHIC; H5

1;PL;2.5/.008
Wide field view showing weathering intensity plus attacked chondrules and chondrule fragments.

2;XN;2.5/.008
Same view in polarized light.

3;PL;6.3/.20
Close up of chondrule fragment in same orientation. Note opacity of NNL staining.

4;XN;6.3/.20
Same view in polarized light.

5;PL;6.3/.20
Another example at same magnification.

6;XN;6.3/.20
Same view in polarized light.

7;PL;6.3/.20
Another chondrule and portions of surrounding chondrules. Chondrules show considerable clouding.

8;XL;6.3/.20
Same view in polarized light.

9;PL;2.5/.008
Another set of chondrules.

10;XN;2.5/.008
Same view in polarized light.

11;PL;6.3/.20
Closeup of one chondrule.

12;XN;6.3/.20
Same view in polarized light. Color difference is due to sweeping extinction.

13;PL;6.3/.20
Microporphyritic chondrule.

14;XN;6.3/.20
Same view in polarized light.

15;PL;16/.45
This chondrules appears to have been either (1) attacked in a stair-step fashion, or (2) fractured along cleavage planes to produce a stair-step appearance which later became filled with rust.

16;XN;16/.45
Same view in polarized light.

17;PL;2.5/.008
Large chondrule containing what appears to be weathered, devitrified glass.

18;XN;2.5/.008
Same view in polarized light.

19;PL;6.3/.20
Devitrified glass under higher magnification. While crystals appear relatively untouched by weathering attack, some areas of clouding occur as ribbon-like stripes which transect the grains. Note opacity of fracture fillings.

20;XN;6.3/.20
Same view in polarized light.

21;PL;6.3/.20
Microporphyritic chondrule with very large euhedral olivine crystals.

22;XN;6.3/.20
Same view in polarized light.

23;PL;6.3/.20
Completely clouded pyroxene chondrule.

24;XN;6.3/.20
Same view in polarized light.

25;PL;6.3/.20
Another example with classic pyroxene cleavage. Cleavage planes are filled with rust.

26;XN;6.3/.20
Same view in polarized light.

APPENDIX C

X-RAY DIFFRACTION DATA

Diffractogram A Carichic		Diffractogram B Carichic		Diffractogram C Carichic		Diffractogram D Carichic		Diffractogram E Carichic		Diffractogram O Carichic		Diffractogram P Carichic		Akaganéite JCPDS 13-157	
d (Å)	I*	d (Å)	I	d (Å)	I	d (Å)	I	d (Å)	I	d (Å)	I	d (Å)	I	d (Å)	I
														7.40	100
														5.25	40
3.72	32	3.72	27	3.72	28	3.69	58	3.68	14	3.70	43			3.70	10
				3.30	24	3.33	30			3.33	45			3.31	100
												2.60	24	2.616	40
2.51	100	2.51	100	2.51	100			2.53	100	2.51	100	2.54	100	2.543	80
										2.34	23			2.343	20
2.27	32	2.26	27	2.26	24	2.27	49	2.28	29	2.25	46	2.27	31	2.285	40
2.087	21			2.09	25	2.08	34	2.11	19			2.11	24	2.097	20
				2.03	18									2.064	20
						1.91	100			1.913	46			1.944	60
		1.88	20									1.84	15	1.854	10
1.750	45	1.74	33	1.752	35	1.75	45	1.759	41	1.749	35	1.73	33	1.746	40
1.720	32									1.719	31			1.719	10
						1.63	63			1.633	65			1.635	100
												1.51	28	1.515	40
1.486	35	1.484	27	1.484	27			1.489	29			1.490	36	1.497	20
						1.480	30							1.480	20
														1.459	10
														1.438	80

*Intensity (I) normalized to 100 for the most intense peak

Diffractogram F ALHA84075,7		Diffractogram G ALHA84075,7		Diffractogram H ALHA84075,7		Diffractogram I ALHA77271,27		Diffractogram J ALHA77271,27		Akaganéite JCPDS 13-157	
d (Å)	I*	d (Å)	I	d (Å)	I	d (Å)	I	d (Å)	I	d (Å)	I
				7.23	43					7.40	100
										5.25	40
3.71	29	3.71	26	3.67	100	3.71	42	3.72	50	3.70	10
		3.28	19	3.29	57	3.30	32			3.31	100
				2.64	36	2.64	32			2.616	40
2.51	100	2.51	100	2.54	57	2.51	100	2.51	100	2.543	80
2.34	15	2.34	15							2.343	20
2.26	34	2.27	37	2.27	70	2.27	37			2.285	40
2.087	37	2.086	32	2.09	57	2.08	45			2.097	20
				2.08	43					2.064	20
		1.940	11			1.92	22			1.944	60
										1.854	10
1.750	58	1.747	44	1.746	70	1.75	45	1.75	42	1.746	40
1.720	13	1.713	15			1.716	26			1.719	10
1.640	11	1.637	19	1.616	43					1.635	100
1.510	15									1.515	40
1.500	18	1.497	22							1.497	20
1.480	35	1.482	33	1.480	70	1.481	37			1.480	20
										1.459	10
						1.440	21			1.438	80

*Intensity (I) normalized to 100 for the most intense peak

Diffractogram K ALHA77271,27		Diffractogram L ALHA77271,27		Diffractogram M ALHA77182,21		Diffractogram N ALHA77182,21		Diffractogram Q ALHA77182,21		Akaganéite JCPDS 13-157	
d (Å)	I*	d (Å)	I	d (Å)	I	d (Å)	I	d (Å)	I	d (Å)	I
				7.30	41	7.31	68			7.40	100
				5.26	48					5.25	40
3.70	45	3.71	75	3.68	41	3.70	45	3.73	31	3.70	10
								3.28	36	3.31	100
2.64	30			2.64	48	2.64	34	2.64	35	2.616	40
2.51	100	2.51	100	2.51	100	2.51	100	2.51	100	2.543	80
						2.34	23			2.343	20
2.26	28			2.26	47	2.28	34	2.27	37	2.285	40
2.085	38			2.085	55	2.08	34	2.085	37	2.097	20
										2.064	20
				1.953	37					1.944	60
										1.854	10
1.749	41			1.746	52	1.741	39	1.748	70	1.746	40
						1.720	45	1.716	43	1.719	10
										1.635	100
										1.515	40
										1.497	20
1.482	35									1.480	20
										1.459	10
										1.438	80

*Intensity (I) normalized to 100 for the most intense peak

Diffractogram A Carichic		Diffractogram B Carichic		Diffractogram C Carichic		Diffractogram D Carichic		Diffractogram E Carichic		Diffractogram O Carichic		Diffractogram P Carichic		Goethite JCPDS 17-536	
d (Å)	I*	d (Å)	I	d (Å)	I	d (Å)	I	d (Å)	I	d (Å)	I	d (Å)	I	d (Å)	I
														4.98	10
4.18	100	4.17	100	4.16	100	4.13	100	4.23	100	4.15	100			4.18	100
				3.36	44							3.40	61	3.38	10
		2.70	60	2.69	58	2.69	36	2.72	53	2.68	47			2.69	30
		2.58	40	2.57	36									2.58	8
														2.50	4
														2.49	16
														2.45	25
2.25	63	2.26	40	2.25	48	2.27	36	2.27	44	2.25	54	2.27	100	2.252	10
2.19	27	2.19	30	2.18	36			2.17	25			2.18	76	2.192	20
														2.009	2
						1.91	73							1.920	6
														1.799	8
														1.770	2
1.720	54													1.721	20
														1.694	10
														1.661	4
		1.60	16											1.606	6
														1.564	16
										1.510	16	1.51	88	1.509	10
														1.467	4

*Intensity (I) normalized to 100 for the most intense peak

Diffractogram F ALHA84075,7		Diffractogram G ALHA84075,7		Diffractogram H ALHA84075,7		Diffractogram I ALHA77271,27		Diffractogram J ALHA77271,27		Goethite JCPDS 17-536	
d (Å)	I*	d (Å)	I	d (Å)	I	d (Å)	I	d (Å)	I	d (Å)	I
										4.98	10
4.17	55	4.16	63	4.17	64	4.18	65	4.19	100	4.18	100
						3.36	65			3.38	10
2.69	35	2.65	63	3.67	100	2.64	86			2.69	30
2.57	32					2.56	86	2.58	91	2.58	8
				3.52	49					2.50	4
										2.49	16
										2.45	25
2.26	100	2.25	100	2.24	70	2.27	100	2.24	73	2.252	10
2.19	32	2.16	50							2.192	20
						2.01	78			2.009	2
		1.910	50			1.92	59			1.920	6
										1.799	8
								1.75	76	1.770	2
1.720	39					1.716	70			1.721	20
										1.694	10
										1.661	4
										1.606	6
										1.564	16
										1.509	10
1.470	55									1.467	4

*Intensity (I) normalized to 100 for the most intense peak

Diffractogram K ALHA77271,27		Diffractogram L ALHA77271,27		Diffractogram M ALHA77182,21		Diffractogram N ALHA77182,21		Diffractogram Q ALHA77182,21		Goethite JCPDS 17-536	
d (Å)	I*	d (Å)	I	d (Å)	I	d (Å)	I	d (Å)	I	d (Å)	I
						5.06	100	5.10	100	4.98	10
		4.17	100			4.17	47	4.13	100	4.18	100
3.36	61									3.38	10
2.64	73	2.65	42	2.64	92	2.64	29	2.64	81	2.69	30
						2.58	20			2.58	8
										2.50	4
										2.49	16
										2.45	25
2.25	68			2.26	90	2.24	47	2.25	65	2.252	10
										2.192	20
										2.009	2
								1.918	51	1.920	6
										1.799	8
										1.770	2
1.749	100			1.746	100	1.722	33	1.716	100	1.721	20
										1.694	10
1.670	61									1.661	4
										1.606	6
										1.564	16
										1.509	10
										1.467	4

*Intensity (I) normalized to 100 for the most intense peak

Diffractogram A Carichic		Diffractogram B Carichic		Diffractogram C Carichic		Diffractogram D Carichic		Diffractogram E Carichic		Diffractogram O Carichic		Diffractogram P Carichic		Hypersthene JCPDS 19-606	
d (Å)	I*	d (Å)	I	d (Å)	I	d (Å)	I	d (Å)	I	d (Å)	I	d (Å)	I	d (Å)	I
														6.38	2
														4.57	16
4.02	30			4.02	29	4.00	39	4.07	29	4.00	63			4.03	20
3.64	16													3.62	2
3.36	21			3.36	22	3.33	23			3.33	45			3.33	16
3.18	73	3.16	87	3.20	53	3.16	74	3.20	81	3.19	92	3.21	79	3.18	100
2.98	38	2.99	37	2.98	35	2.98	37	2.96	43	2.97	39			2.960	35
2.87	54	2.87	53			2.86	74	2.89	43	2.86	60			2.883	50
		2.83	27					2.85	21			2.81	44	2.835	20
2.71	31	2.70	40	2.69	29	2.69	37					2.73	30	2.721	25
		2.58	27	2.57	18			2.53	100			2.54	100	2.555	40
2.51	98	2.51	100	2.51	100	2.50	100			2.51	100			2.510	30
2.46	100	2.46	90	2.49	76	2.45	91	2.47	86	2.45	94	2.49	95	2.484	30
														2.399	16
2.25	36	2.26	27	2.25	24	2.27	37	2.27	24	2.25	46	2.27	31	2.256	6
2.19	16	2.19	20	2.18	18			2.17	14			2.18	24	2.194	2
						2.11	30	2.11	19			2.11	24	2.122	20
2.087	21			2.09	25	2.08	26							2.109	20
														2.065	16
				2.03	18									2.034	16
1.990	18													2.000	16
														1.969	20
		1.88	20			1.91	75							1.895	4
												1.84	15	1.846	8
														1.810	4
														1.790	6
1.750	44	1.74	33	1.752	35	1.75	34	1.759	41	1.749	35	1.76	38	1.749	8
										1.719	31			1.708	6
														1.688	4
														1.662	2
						1.63	47			1.633	65			1.644	2
		1.60	11											1.619	16
														1.596	16
												1.51	28	1.539	6
														1.526	6
												1.490	36	1.496	20
1.486	34	1.484	27	1.484	27	1.480	23	1.489	29					1.484	16
														1.431	6
														1.400	16

*Intensity (I) normalized to 100 for the most intense peak

Diffractogram F ALHA84075,7		Diffractogram G ALHA84075,7		Diffractogram H ALHA84075,7		Diffractogram I ALHA77271,27		Diffractogram J ALHA77271,27		Hypersthene JCPDS 19-606	
d (Å)	I*	d (Å)	I	d (Å)	I	d (Å)	I	d (Å)	I	d (Å)	I
		6.33	11							6.38	2
										4.57	16
4.00	17	4.00	30			4.02	40	4.01	70	4.03	20
				3.64	29	3.62	21			3.62	2
						3.36	24			3.33	16
3.16	70	3.19	56	3.16	80	3.19	100	3.19	90	3.18	100
2.96	41	2.97	46	2.97	53	2.98	42	2.98	45	2.960	35
2.86	53	2.86	56	2.86	40	2.86	42			2.883	50
						2.83	32			2.835	20
2.69	11									2.721	25
2.57	10			2.54	27	2.56	32			2.555	40
2.51	92	2.51	100	2.51	100	2.51	100	2.51	100	2.510	30
2.46	100	2.46	96	2.45	83	2.46	79	2.46	80	2.484	30
										2.399	16
2.26	31	2.25	30	2.24	33	2.27	37	2.24	40	2.256	6
		2.16	15							2.194	2
2.24	31									2.122	20
		2.086	32			2.08	45			2.109	20
2.087	34			2.09	27					2.065	16
										2.034	16
1.990	10	1.980	11			2.01	29			2.000	16
		1.940	11							1.969	20
						1.92	22			1.895	4
										1.846	8
										1.810	4
										1.790	6
1.750	53	1.747	44	1.746	33	1.75	45	1.75	42	1.749	8
										1.706	6
1.670	10									1.688	4
										1.662	2
1.640	10									1.644	2
1.621	21	1.620	19	1.616	20					1.619	16
										1.596	16
										1.539	6
1.510	14									1.526	6
1.496	21	1.497	22							1.496	20
1.480	32	1.482	33	1.480	33	1.481	37			1.484	16
						1.440	21			1.431	6
										1.400	16

*Intensity (I) normalized to 100 for the most intense peak

Diffractogram K ALHA77271,27		Diffractogram L ALHA77271,27		Diffractogram M ALHA77182,21		Diffractogram N ALHA77182,21		Diffractogram Q ALHA77182,21		Hypersthene JCPDS 19-606	
d (Å)	I*	d (Å)	I	d (Å)	I	d (Å)	I	d (Å)	I	d (Å)	I
										6.38	2
						4.55	22			4.57	16
4.00	40			4.02	38			4.00	40	4.03	20
						3.61	19			3.62	2
3.36	25									3.33	16
3.19	90	3.16	93	3.21	76	3.16	100	3.19	82	3.18	100
2.96	40					2.93	47			2.960	35
2.86	30					2.86	38	2.86	43	2.883	50
						2.82	19	2.82	25	2.835	20
										2.721	25
						2.58	13			2.555	40
2.51	100	2.51	100	2.51	92	2.51	56	2.51	99	2.510	30
2.45	85	2.45	100	2.45	100	2.45	44	2.46	100	2.484	30
						2.41	16			2.399	16
2.25	28			2.26	43	2.24	31	2.25	28	2.256	6
										2.194	2
										2.122	20
2.085	38									2.109	20
						2.08	19	2.085	37	2.065	16
										2.034	16
										2.000	16
				1.953	34					1.969	20
								1.918	22	1.895	4
										1.846	8
										1.810	4
										1.790	6
1.749	41			1.746	48	1.741	22	1.748	69	1.749	8
										1.708	6
1.670	25									1.688	4
										1.662	2
										1.644	2
										1.619	16
										1.598	16
										1.539	6
										1.526	6
										1.496	20
1.482	35									1.484	16
										1.431	6
										1.400	16

*Intensity (I) normalized to 100 for the most intense peak

Diffractogram A Carichic		Diffractogram B Carichic		Diffractogram C Carichic		Diffractogram D Carichic		Diffractogram E Carichic		Diffractogram O Carichic		Diffractogram P Carichic		Lepidocrocite JCPDS 8-98	
d (Å)	I*	d (Å)	I	d (Å)	I	d (Å)	I	d (Å)	I	d (Å)	I	d (Å)	I	d (Å)	I
														6.26	100
				3.30	32									3.29	90
2.77	57	2.77	67	2.78	54	2.76	58	2.79	56	2.76	66	2.81	46	2.79	10
2.46	100	2.46	100	2.49	100	2.45	100	2.47	100	2.45	100	2.49	100	2.47	80
														2.36	20
				2.09	33	2.08	28	2.11	22					2.09	20
														1.937	70
														1.848	20
		1.74	37	1.752	46	1.75	38	1.759	48	1.749	37	1.73	35	1.732	40
		1.60	12											1.566	20
														1.535	20
												1.51	29	1.524	40
		1.484	30	1.484	36	1.480	25	1.489	34			1.490	38	1.496	10
														1.449	10
														1.433	20
														1.418	10

*Intensity (I) normalized to 100 for the most intense peak

Diffractogram F ALHA84075,7		Diffractogram G ALHA84075,7		Diffractogram H ALHA84075,7		Diffractogram I ALHA77271,27		Diffractogram J ALHA77271,27		Lepidocrocite JCPDS 8-98	
d (Å)	I*	d (Å)	I	d (Å)	I	d (Å)	I	d (Å)	I	d (Å)	I
		6.33	11							6.26	100
3.27	12	3.28	20	3.29	33	3.30	41			3.29	90
2.76	79	2.76	85	2.76	81	2.76	67	2.76	63	2.79	10
2.46	100	2.46	100	2.45	100	2.46	100	2.46	100	2.47	80
2.34	14	2.34	16							2.36	20
2.087	34	2.086	33	2.09	33	2.08	57			2.09	20
		1.940	11							1.937	70
										1.848	20
1.720	12									1.732	40
1.570	7									1.566	20
										1.535	20
										1.524	40
1.495	21	1.497	23							1.496	10
										1.449	10
										1.433	20
										1.418	10

*Intensity (I) normalized to 100 for the most intense peak

Diffractogram K ALHA77271,27		Diffractogram L ALHA77271,27		Diffractogram M ALHA77182,21		Diffractogram N ALHA77182,21		Diffractogram Q ALHA77182,21		Lepidocrocite JCPDS 8-98	
d (Å)	I*	d (Å)	I	d (Å)	I	d (Å)	I	d (Å)	I	d (Å)	I
								6.25	31	6.26	100
								3.28	36	3.29	90
2.76	59			2.76	43	2.77	57	2.76	43	2.79	10
2.45	100	2.45	100	2.45	100	2.45	100	2.46	100	2.47	80
						2.34	30			2.36	20
2.085	45			2.085	51	2.08	43	2.085	37	2.09	20
										1.937	70
										1.848	20
						1.722	50			1.732	40
										1.566	20
										1.535	20
										1.524	40
1.482	41									1.496	10
										1.449	10
										1.433	20
										1.418	10

*Intensity (I) normalized to 100 for the most intense peak

Diffractogram A Carichic		Diffractogram B Carichic		Diffractogram C Carichic		Diffractogram D Carichic		Diffractogram E Carichic		Diffractogram O Carichic		Diffractogram P Carichic		Maghemite JCPDS 15-615	
d (Å)	I*	d (Å)	I	d (Å)	I	d (Å)	I	d (Å)	I	d (Å)	I	d (Å)	I	d (Å)	I
														7.04	18
														6.35	8
														5.95	60
														5.75	4
														5.37	8
														5.00	8
														4.84	40
														4.32	25
														4.13	2
3.88	32	3.88	40	3.88	31	3.90	45			3.87	46			3.86	12
3.72	32	3.72	27	3.72	28							3.79	24	3.75	100
3.51	23	3.48	40	3.48	24			3.50	24	3.48	43	3.54	19	3.50	12
														3.42	65
				3.20	53			3.20	81	3.19	92	3.21	79	3.216	25
														3.077	2
2.94	43	2.94	40	2.94	41			2.96	43	2.97	39	2.91	48	2.95	100
2.87	55	2.87	53			2.86	74	2.85	21	2.86	60			2.871	1
2.77	58	2.77	60	2.78	41			2.79	48	2.76	62			2.799	18
														2.642	25
2.51	100	2.51	100	2.51	100	2.50	100	2.53	100	2.51	100	2.54	100	2.521	100
														2.451	1
														2.414	8
														2.318	8
2.25	37	2.26	27	2.26	24					2.25	46			2.234	4
2.19	16	2.19	20	2.18	18			2.17	14			2.18	24	2.208	4
2.087	21			2.09	25	2.08	26					2.11	24	2.089	100
				2.03	18									2.026	1
1.990	18													1.994	1
														1.967	1
														1.863	2
														1.836	1
														1.822	16
														1.778	1
1.750	45	1.74	33	1.752	35	1.75	34			1.749	35			1.749	1
														1.702	100
														1.669	8
						1.63	47			1.633	65			1.638	4
		1.60	11											1.608	100

*Intensity (I) normalized to 100 for the most intense peak

Diffractogram F ALHA84075,7		Diffractogram G ALHA84075,7		Diffractogram H ALHA84075,7		Diffractogram I ALHA77271,27		Diffractogram J ALHA77271,27		Maghemite JCPDS 15-615	
d (Å)	I*	d (Å)	I	d (Å)	I	d (Å)	I	d (Å)	I	d (Å)	I
				6.91	20					7.04	18
		6.33	11	6.31	23					6.35	8
										5.95	60
										5.75	4
										5.37	8
										5.00	8
										4.84	40
										4.32	25
				4.12	43			4.15	65	4.13	2
3.87	48	3.87	52	3.83	67	3.87	32	3.87	60	3.86	12
								3.72	50	3.75	100
3.48	29			3.47	37	3.48	21			3.50	12
										3.42	65
		3.19	56					3.19	90	3.216	25
										3.077	2
2.96	45	2.97	46	2.97	53	2.98	42			2.95	100
2.86	58	2.86	56	2.86	40	2.86	42			2.871	1
2.76	86	2.76	82	2.76	67	2.76	53	2.76	50	2.799	18
2.65	23	2.65	19	2.64	17	2.64	32			2.642	25
2.51	100	2.51	100	2.51	100	2.51	100	2.51	100	2.521	100
										2.451	1
										2.414	8
		2.34	15							2.318	8
2.24	34	2.25	30					2.24	40	2.234	4
2.19	11									2.208	4
2.087	37	2.086	32	2.09	27	2.08	45			2.089	100
						2.01	29			2.026	1
1.990	11	1.980	11							1.994	1
										1.967	1
										1.863	2
										1.836	1
										1.822	16
										1.778	1
1.750	58	1.747	44	1.746	33	1.75	45	1.75	42	1.749	1
										1.702	100
		1.670	11							1.669	8
1.640	11	1.637	19							1.638	4
										1.608	100

*Intensity (I) normalized to 100 for the most intense peak

Diffractogram K ALHA77271,27		Diffractogram L ALHA77271,27		Diffractogram M ALHA77182,21		Diffractogram N ALHA77182,21		Diffractogram Q ALHA77182,21		Maghemite JCPDS 15-615	
d (Å)	I*	d (Å)	I	d (Å)	I	d (Å)	I	d (Å)	I	d (Å)	I
										7.04	18
										6.35	8
										5.95	60
								5.75	27	5.75	4
										5.37	8
										5.00	8
										4.84	40
						4.33	34			4.32	25
								4.13	43	4.13	2
3.87	50	3.87	67			3.87	45	3.87	43	3.86	12
		3.71	67					3.73	31	3.75	100
		3.49	56	3.50	41	3.48	34	3.48	25	3.50	12
										3.42	65
3.19	90	3.20	100	3.21	83	3.19	100	3.19	83	3.216	25
										3.077	2
2.96	40			2.98	46	2.93	84			2.95	100
2.86	30					2.86	68	2.86	43	2.871	1
2.76	50	2.76	56	2.76	47	2.77	45	2.76	43	2.799	18
2.64	30	2.65	33	2.64	48	2.64	34	2.64	35	2.642	25
2.51	100	2.51	89	2.51	100	2.51	100	2.51	100	2.521	100
										2.451	1
						2.41	29			2.414	8
						2.34	23			2.318	8
				2.26	47	2.24	55	2.25	28	2.234	4
										2.208	4
2.085	38			2.085	55	2.08	34	2.085	37	2.089	100
										2.026	1
										1.994	1
										1.967	1
										1.863	2
										1.836	1
										1.822	16
										1.778	1
1.749	41			1.746	52	1.741	39	1.748	70	1.749	1
										1.702	100
1.670	25									1.669	8
										1.638	4
										1.608	100

*Intensity (I) normalized to 100 for the most intense peak

Diffractogram A Carichic		Diffractogram B Carichic		Diffractogram C Carichic		Diffractogram D Carichic		Diffractogram E Carichic		Diffractogram O Carichic		Diffractogram P Carichic		Olivine JCPDS 7-77	
d (Å)	I*	d (Å)	I	d (Å)	I	d (Å)	I	d (Å)	I	d (Å)	I	d (Å)	I	d (Å)	I
5.11	22	5.08	30	5.10	18	5.10	36							5.10	50
														4.30	10
3.88	31	3.88	40	3.88	31	3.90	45			3.87	46			3.88	70
3.72	31	3.72	27	3.72	28					3.70	43			3.72	10
3.51	23	3.48	40	3.48	24	3.47	37	3.50	24	3.48	43			3.50	20
								3.01	38			3.00	45	3.00	10
2.98	38	2.99	37	2.98	35	2.98	37	2.96	43	2.97	39			2.992	10
2.77	57	2.77	60	2.76	49	2.76	53	2.79	48	2.76	62	2.73	30	2.768	60
2.51	98	2.51	100	2.51	100	2.50	100	2.53	100	2.51	100	2.54	100	2.512	70
2.46	100	2.46	90			2.45	91	2.47	86	2.45	94			2.458	100
														2.383	5
										2.34	23			2.347	20
														2.316	10
2.27	31	2.26	27	2.26	24	2.27	37	2.27	24			2.27	31	2.269	40
2.25	36			2.25	24					2.25	46			2.250	30
2.19	16	2.19	20	2.18	18			2.17	14			2.18	24	2.161	10
				2.03	18									2.032	5
		1.88	20									1.84	15	1.876	20
														1.785	5
1.750	44			1.752	35	1.75	34	1.759	41			1.76	38	1.750	40
		1.74	33							1.749	35			1.740	10
												1.73	33	1.731	10
														1.671	10
														1.636	10
						1.63	47			1.633	65			1.634	10
														1.619	20
		1.60	11											1.590	5
								1.489	29			1.490	36	1.497	20
1.476	31					1.480	23							1.479	20
														1.397	10

*Intensity (I) normalized to 100 for the most intense peak

Diffractogram F ALHA84075,7		Diffractogram G ALHA84075,7		Diffractogram H ALHA84075,7		Diffractogram I ALHA77271,27		Diffractogram J ALHA77271,27		Olivine JCPDS 7-77	
d (Å)	I*	d (Å)	I	d (Å)	I	d (Å)	I	d (Å)	I	d (Å)	I
5.07	32	5.08	33	5.08	33	5.07	21			5.10	50
										4.30	10
3.87	44	3.87	52			3.87	32	3.87	60	3.88	70
3.71	27	3.71	26			3.71	42	3.72	50	3.72	10
3.48	27	3.48	26	3.52	23	3.48	21			3.50	20
										3.00	10
2.96	41	2.97	46	2.97	53	2.98	42	2.98	45	2.992	10
2.76	79	2.76	82	2.76	67	2.76	53	2.76	50	2.768	60
2.51	92	2.51	100	2.51	100	2.51	100	2.51	100	2.512	70
2.46	100	2.46	96	2.45	83	2.46	79	2.46	80	2.458	100
										2.383	5
2.34	14	2.34	15							2.347	20
										2.316	10
2.26	31	2.27	37	2.27	33	2.27	37			2.269	40
2.24	31	2.25	30	2.24	33			2.24	40	2.250	30
2.16	14	2.16	15							2.161	10
										2.032	5
1.990	10									1.876	20
										1.785	5
1.750	53			1.746	33	1.75	45	1.75	42	1.750	40
		1.747	44							1.740	10
										1.731	10
1.670	10	1.670	11							1.671	10
1.640	10	1.637	19							1.636	10
										1.634	10
1.621	21	1.620	19	1.616	20					1.619	20
										1.590	5
1.495	21	1.497	22							1.497	20
1.480	32			1.480	33	1.481	37			1.479	20
						1.440	21			1.397	10

*Intensity (I) normalized to 100 for the most intense peak

Diffractogram K ALHA77271,27		Diffractogram L ALHA77271,27		Diffractogram M ALHA77182,21		Diffractogram N ALHA77182,21		Diffractogram Q ALHA77182,21		Olivine JCPDS 7-77	
d (Å)	I*	d (Å)	I	d (Å)	I	d (Å)	I	d (Å)	I	d (Å)	I
5.05	35					5.06	100	5.10	43	5.10	50
						4.33	29			4.30	10
3.87	50	3.87	75			3.87	38	3.87	43	3.88	70
3.70	45	3.71	75			3.70	38	3.73	31	3.72	10
3.48	20	3.49	63	3.50	38	3.48	29	3.48	25	3.50	20
										3.00	10
2.96	40			2.98	42					2.992	10
2.76	50	2.76	63	2.76	43	2.77	38	2.76	43	2.768	60
2.51	100	2.51	100	2.51	92	2.51	85	2.51	99	2.512	70
2.45	85	2.45	100	2.45	100	2.45	67	2.46	100	2.458	100
										2.383	5
						2.34	20			2.347	20
						2.30	20			2.316	10
2.26	28			2.26	43	2.28	29	2.27	37	2.269	40
2.25	28					2.24	47	2.25	28	2.250	30
										2.161	10
										2.032	5
										1.876	20
										1.785	5
1.749	41							1.748	69	1.750	40
				1.746	48	1.741	33			1.740	10
										1.731	10
1.670	25									1.671	10
										1.636	10
										1.634	10
										1.619	20
										1.590	5
										1.497	20
										1.479	20
										1.397	10

*Intensity (I) normalized to 100 for the most intense peak

Diffractogram A Carichic		Diffractogram B Carichic		Diffractogram C Carichic		Diffractogram D Carichic		Diffractogram E Carichic		Diffractogram O Carichic		Diffractogram P Carichic		Plagioclase JCPDS 10-393	
d (Å)	I*	d (Å)	I	d (Å)	I	d (Å)	I	d (Å)	I	d (Å)	I	d (Å)	I	d (Å)	I
														6.43	8
														6.36	10
														5.84	2
														5.67	2
														4.69	2
4.02	30			4.02	29			4.07	29					4.04	16
3.88	31	3.88	40	3.88	31	3.90	45			3.87	46			3.88	12
3.72	31	3.72	27	3.72	28			3.76	29					3.75	30
3.64	16													3.64	12
3.48	43	3.48	40	3.48	24	3.47	37	3.50	24	3.48	43			3.48	6
3.36	21			3.36	22									3.37	8
										3.19	92	3.21	79	3.21	30
3.18	73	3.16	87	3.20	53	3.16	74	3.20	81	3.16	115			3.18	100
						3.15	90							3.13	12
								3.01	38			3.03	38	3.02	8
2.94	42	2.94	40	2.94	41	2.98	37	2.96	43	2.97	39			2.950	10
														2.927	12
												2.91	48	2.917	2
		2.83	27			2.86	74	2.85	21	2.86	60	2.81	44	2.830	12
										2.68	40			2.654	4
2.51	98	2.51	100					2.53	100	2.51	100	2.54	100	2.518	8
				2.51	100	2.50	100					2.49	95	2.506	8
2.46	100	2.46	90			2.45	91	2.47	86	2.45	94			2.450	2
										2.34	23			2.369	4
														2.301	2
2.27	31					2.27	37	2.28	29			2.27	31	2.281	2
		2.26	27	2.26	24			2.27	24					2.266	2
2.25	36			2.25	24					2.25	46			2.245	2
2.19	16	2.19	20	2.18	18			2.17	14			2.18	24	2.182	2
												2.11	24	2.140	8
						2.11	30	2.11	19					2.120	6

*Intensity (I) normalized to 100 for the most intense peak

Diffractogram F ALHA84075,7		Diffractogram G ALHA84075,7		Diffractogram H ALHA84075,7		Diffractogram I ALHA77271,27		Diffractogram J ALHA77271,27		Plagioclase JCPDS 10-393	
d (Å)	I*	d (Å)	I	d (Å)	I	d (Å)	I	d (Å)	I	d (Å)	I
										6.43	8
		6.33	11	6.31	23					6.36	10
										5.84	2
										5.67	2
						4.72	21			4.69	2
						4.02	40	4.01	70	4.04	16
3.87	44	3.87	52			3.87	32	3.87	60	3.88	12
								3.72	50	3.75	30
		3.67	7	3.64	29	3.62	21			3.64	12
3.48	27	3.48	26	3.47	37	3.48	21			3.48	6
						3.36	24			3.37	8
		3.19	56							3.21	30
3.16	70	3.16	78	3.16	80	3.19	100	3.19	90	3.18	100
						3.16	95	3.16	90	3.13	12
										3.02	8
2.96	41	2.97	46	2.97	53	2.98	42			2.950	10
2.93	38	2.93	33			2.93	37			2.927	12
										2.917	2
2.86	53	2.86	56	2.86	40	2.83	32			2.830	12
2.65	21	2.65	19	2.64	17	2.64	32			2.654	4
2.51	92	2.51	100	2.51	100	2.51	100	2.51	100	2.518	8
										2.506	8
2.46	100	2.46	96	2.45	83	2.46	79	2.46	80	2.450	2
2.34	14	2.34	15							2.369	4
										2.301	2
		2.27	37	2.27	33	2.27	37			2.281	2
2.26	31			2.24	33					2.266	2
2.24	31	2.25	30					2.24	40	2.245	2
2.19	10									2.182	2
2.16	14	2.16	15							2.140	8
										2.120	6

*Intensity (I) normalized to 100 for the most intense peak

Diffractogram K ALHA77271,27		Diffractogram L ALHA77271,27		Diffractogram M ALHA77182,21		Diffractogram N ALHA77182,21		Diffractogram Q ALHA77182,21		Plagioclase JCPDS 10-393	
d (Å)	I*	d (Å)	I	d (Å)	I	d (Å)	I	d (Å)	I	d (Å)	I
										6.43	8
										6.36	10
5.81	20									5.84	2
										5.67	2
										4.69	2
				4.02	38					4.04	16
3.87	50	3.87	67			3.87	25	3.87	43	3.88	12
								3.73	31	3.75	30
						3.61	19			3.64	12
3.48	20	3.49	56	3.50	38	3.48	19	3.48	25	3.48	6
3.36	25									3.37	8
3.19	90	3.20	100	3.21	76					3.21	30
3.16	90	3.16	83	3.17	76	3.19	56	3.19	82	3.18	100
						3.16	100	3.16	77	3.13	12
										3.02	8
				2.98	42					2.950	10
2.93	30					2.93	47	2.92	31	2.927	12
										2.917	2
2.86	30					2.82	19	2.82	25	2.830	12
2.64	30	2.65	33	2.64	44	2.64	19	2.64	35	2.654	4
2.51	100	2.51	89	2.51	92	2.51	56	2.51	99	2.518	8
										2.506	8
2.45	85	2.45	89	2.45	100	2.45	44	2.46	100	2.450	2
						2.34	13			2.369	4
						2.30	13			2.301	2
						2.28	19	2.27	37	2.281	2
2.26	28			2.26	43			2.25	28	2.266	2
2.25	28			2.085	51	2.24	31			2.245	2
				1.953	34					2.182	2
				1.746	48					2.140	8
										2.120	6

*Intensity (I) normalized to 100 for the most intense peak

LIST OF REFERENCES

LIST OF REFERENCES

Alexander C. M. O'D, Barber D. J. and Hutchison R. (1989) The microsctructure of Semarkona and Bishunpur. Geochim. Cosmochim. Acta. 53, 3045-3057.

Annexstad J., Schultz L., and Wänke H., eds. (1986) Workshop on Antarctic Meteorites; LPI Tech. Rept. 86-01. Lunar and Planetary Institute, Houston.

Bain D. C. and Russell J. D. (1980) Swelling minerals in a basalt and its weathering products from Morvern, Scotland: 1. Interstratified montmorillonite-vermiculite-illite. Clay Minerals. 15, 445-451.

Barber D. J. (1981) Matrix phyllosilicates and associated minerals in C2M carbonaceous chondrites. Geochim. Cosmochim. Acta 45, 945-970.

Barber D. J. (1985) Phyllosilicates and other layer-structured materials in stony meteorites. Clay Minerals. 20, 415-454.

Berner R. A., Sjöberg E. L., Velbel M. A. and Krom M. D. (1979) Dissolution of pyroxenes and amphiboles during weathering. Science 207, 1205-1206.

Bevan A. W. R. and Binns R. A. (1989) Further meteorite recoveries from the Nullarbor Region, Western Australia. Abstract. Meteoritics 24, 251.

Best M. G. (1982) Igneous and metamorphic petrology. W. H. Freeman and Co. 630 pp.

Biswas S., Walsh T. M., Ngo H. T., and Lipschutz M. E. (1980) Trace element contents of selected Antarctic meteorites--I. Weathering effects and ALHA77005, A77257, A77278 and A77299. Z. Naturforsch. 35a, 191-196.

Boeckl R. (1972) Terrestrial age of nineteen stony meteorites derived from their radiocarbon content. Nature 236, 25-26.

Brearley A. J., Scott E. R. D., Keil K., Clayton R. N., Mayeda T. K., Boynton W. V. and Hill D. H. (1989) Chemical, isotopic and mineralogical evidence for the origin of matrix in ordinary chondrites. Geochim. Cosmochim. Acta. 53, 2081-2093.

Buchwald V.F. (1990) On the difference between weathering products on Antarctic and non-Antarctic meteorites. In Workshop on Differences between Antarctic and non-Antarctic meteorites (eds. C. Koeberl and W. A. Cassidy); LPI Tech. Rept. 90-01, pp. 24-26. Lunar and Planetary Institute, Houston.

Buchwald V. F. and Clarke R. S., Jr. (1989) Corrosion of Fe-Ni alloys by Cl- containing akaganéite (ß-FeOOH): The Antarctic meteorite case. Amer. Mineral. 74, 656-667.

Bull C. and Lipschutz M. E. (1982) Workshop on Antarctic Glaciology and Meteorites; LPI Tech. Rept. 82-03. Lunar and Planetary Institute, Houston.

Burns R. G. (1993) The MSATT workshop on chemical weathering on Mars. Geochim. Cosmochim. Acta. 57, 4551-4554.

Carr, R. H., Grady, M. M., Wright, I. P., and Pillinger, C. T., (1985) Martian atmospheric carbon dioxide and weathering products in SNC meteorites. Nature. 314, pp. 248-250.

Cashore J., McKinney M. L., and McSween H. Y., Jr. (1988) No evidence for different parent bodies of Antarctic and non-Antarctic H chondrites. Lunar Planet. Sci. XIX, 168-169.

Cassidy W. A. (1990) Are there real differences between Antarctic meteorites and modern falls? In Workshop on Differences between Antarctic and non-Antarctic meteorites (C. Koeberl and W. A. Cassidy eds.); LPI Tech Rept. 90-01, pp. 27-29. Lunar and Planetary Institute, Houston.

Cassidy W. A. and Harvey R. P. (1991) Are there real differences between Antarctic finds and modern falls meteorites? Geochim. Cosmochim. Acta 55, 99-104.

Campbell I. B. and Claridge G. G. C. (1987) Antarctica: soils,weathering processes and environment. Developments in soil science 16, Elsevier Science Publishers B. V., Amsterdam, 368 pp.

Chesworth W. (1973) The residua system of chemical weathering: a model for the chemical breakdown of silicate rocks at the surface of the Earth. Jour. Soil Science 24, 69-81.

Claridge G. G. C. (1963) The clay mineralogy and chemistry of some soils from the Ross Dependency, Antarctica. N.Z. J. Geol. Geophys. 8, 186-220.

Claridge G. G. C. and Campbell I. B. (1984) Mineral transformation during the weathering of dolerite under cold air conditions in Antarctica. N. Z. J. Geol. Geophys. 27, 537-545.

Clarke, Roy S. Jr. (1993) personal communication, Smithsonian Institution, National Museum of Natural History, Department of Meteorites, Washignton, D.C.

Curtin D. and Smillie G. W. (1981) Composition and origin of smectite in soils derived from basalt in Northern Ireland. Clays and Clay Minerals. 29, 277-284.

Delisle G. and Sievers J. (1989) Meteorites, concentration mechanisms at the Allan Hills, Victoria Land, Antarctica. Abstract. Meteoritics 24, 261.

Dennison J. E. and Lipschutz M. E. (1987) Chemical studies of H chondrites. II: weathering effects in Victoria Land, Antarctic population and comparison of two Antarctic populations with non-Antarctic falls. Geochim. Cosmochim. Acta 51, 741-754.

Dennison J. E., Lingner D. W. and Lipschutz M. E. (1986) Antarctic and non-Antarctic meteorites from different populations. Nature 319, 390-393.

Dixon J. B. and Weed S. B. (1982) Minerals in soil environments. Soil Science Society of America, Madison, Wisconsin, 948 pp.

Dodd R. T. (1981) Meteorites: A petrologic-chemical synthesis. Cambridge University Press, Cambridge, 368 pp.

Dodd R.T. (1986) Thunderstones and shooting stars. Harvard University Press, Cambridge, 196 pp.

Dodd R. T. (1989) H chondrite clusters and streams. Meteoritics 24, 262-263.

Dreibus G., Wänke H., and Schultz L. (1986) Mysterious iodine-overabundance in Antarctic meteorites. In Workshop on Antarctic Meteorites (J. Annexstad et al. eds.); LPI Tech Rept. 86-01, pp. 34-36. Lunar and Planetary Institute, Houston.

Englert P. A. J. (1990) Cosmogenic radionuclides for historical studies of Antarctic meteorites. In Workshop on Antarctic Meteorite Stranding Surfaces (W. A. Cassidy and I. M. Whillans eds.); LPI Tech Rept. 90-03, pp. 44-48. Lunar and Planetary Institute, Houston.

Evans L. J. and Chesworth W. (1985) The weathering of basalt in an arctic environment. in Volcanic Soils Catena Suppliment 7 (Fernandez Caldas and Dan H. Yaalon eds.), 77-85.

Freundel M., Schultz L., and Reedy R. C. (1986) Terrestrial ^{81}Kr-Kr ages of Antarctic meteorites. Geochim. Cosmochim. Acta 50, 2663-2873.

Fushs, L. H., Olsen E., and Jensen K. J. (1973) Mineralogy, mineral-chemistry, and composition of the Murchison (C2) meteorite. Smithsonian Contrib. Earth Sci. 10.

Gibson E. K. and Bogard D. D. (1978) Chemical alterations of the Holbrook chondrite resulting from terrestrial weathering. Meteoritics 13, 277-289.

Gibson E. K., Wentworth S. J. and McKay D. S. (1983) Chemical weathering and diagenesis of a cold desert soil from Wright Valley, Antarctica: An analogy of Martian weathering processes. Journal of Geophysical Research 88, A912-A928.

Gooding J. L. (1981) Chemical weathering on Mars. Icarus. 33.3 pp. 0001-0031.

Gooding J. L. (1981) Mineralogical aspects of terrestrial weathering effects in chondrites from Allan Hills, Antarctica. Proc. Lunar Planet. Sci. 12B, 1105-1122.

Gooding J. L. (1985) Clay minerals in meteorites: Preliminary identification by analysis of goodness-to-fit to calculated structural formulas. Lunar Planet. Sci. XVI: 278-279 (Abstract).

Gooding J. L. (1986a) Clay-mineraloid weathering products in Antarctic meteorites. Geochim. Cosmochim. Acta. 50, 2215-2223.

Gooding J. L. (1986b) Weathering of stony meteorites in Antarctica. in International Workshop on Antarctic Meteorites (J Annexstad, L. Schultz and H. Wanke eds.). LPI Tech. Rpt. 86-01 Lunar and Planetary Institute, Houston, TX.

Gooding J. L. (1989) Significance of terrestrial weathering effects in Antarctic meteorites. Smithsonian Contributions to the Earth Sciences, Number 28, Smithsonian Institution Press, Washington, DC.

Gooding J. L. (1990) Differential scanning calorimetry (DSC) of meteorites: Overview of possible applications. Papers presented to the 53rd Ann. Mtg. Met. Soc., Perth.

Gow A. J. and Cassidy W. A. (1989) The emerging meteorite: Crystalline structure of the enclosing ice. Smithsonian Contrib. Earth Sci. 28, 87-91.

Grady M. M., Wright I. P., and Pillinger C. T. (1989a) A preliminary investigation into the nature of carbonaceous material in ordinary chondrites. Meteoritics 24, 147-154.

Grady M. M., Wright I. P., and Pillinger C. T. (1991) Comparisons between Antarctic and non-Antarctic meteorites based on carbon isotope geochemistry. Geochim. Cosmochim. Acta 55, 49-58.

Grac

Grah

Gros

Hart

Harv

Huss

Huss

Huss

Hutch

Hutch

Grady M. M., Gibson E. K., Jr., Wright I. P., and Pillinger C.T. (1989b) The formation of weathering products on the LEW85320 ordinary chondrite: Evidence from carbon and oxygen stable isotope compositions and implications for carbonates in SNC meteorites. Meteoritics 24, 1-7.

Graham A. L., Bevan A. W. R., and Hutchison R. (1985) Catalogue of Meteorites. 4th Ed. University of Arizona Press, Tucson, 460 pp.

Grossman J. N. (1994) The meteoritical bulletin, No. 76, 1994 January: the U.S. Antarctic meteorite collection. Meteoritics 29, 100-143.

Hartmetz C. P., Gibson E. K., and Socki R. A. (1989) Total carbon and sulfur abundances in Antarctic carbonaceous chondrites, ordinary chondrites, and eucrites. Meteoritics 24, 274-275.

Harvey R. P. and Cassidy W. A. (1989) A statistical comparison of Antarctic finds and modern falls: Mass frequency distributions and relative abundance by type. Meteoritics 24, 9-14.

Huss G. R. (1990) Meteorite infall as a function of mass: Implications for the accumulation of meteorites on Antarctic ice. Meteoritics 25, 41-56.

Huss G. R. (1991) Meteorite mass distributions and differences between Antarctic and non-Antarctic meteorites. Geochim. Cosmochim. Acta 55, 105-111.

Huss G. R., Keil K. and Taylor G. J. (1981) The matrices of unequilibrated ordinary chondrites: implications for the origin and history of chondrites. Geochim. Cosmochim. Acta. 45, 33-51.

Hutchison R., Alexander C. M. O'D. and Barber D. (1987) The Semarkona meteorite: first occurrence of smectite in an ordinary chondrite, and its implications. Geochim Cosmochim. Acta. 51, 1875-1882.

Hutchison R. (1983) The search for our beginning. Oxford University Press, Oxford; and The British Museum of Natural History, London, 164 pp.

Jackso
Jarose
Jarose
Jarose
Johnso
Jull
Kaczar
Kaneok
Karlss

Jackson M. L. (1967) Soil chemical analysis. Department of Soil Science, University of Wisconsin, Madison, 894 pp.

Jarosewich E. (1993) personal communication, Smithsonian Institution, National Museum of Natural History, Department of Meteorites, Washington, D.C.

Jarosewich E. (1990a) Chemical composition of Antarctic and non-Antarctic chondrites: A comparison. In Workshop on Differences between Antarctic and non-Antarctic Meteorites (C. Koeberl and W. A. Cassidy eds.); LPI Tech Rept. 90-01, pp. 54-56. Lunar and Planetary Institute, Houston.

Jarosewich E. (1990b) Chemical analyses of meteorites: A compilation of stony and iron meteorite analyses. Meteoritics 25, 323-337.

Jarosewich E., and Dodd R. T. (1985) Chemical variations among L-chondrites — IV. Analyses with petrologic notes of 13 L-group and 3 LL-group chondrites. Meteoritics 20, 23-36.

Johnson C. A. and Prinz M. (1992) Carbonate compositions in CM and CI chondrites, and implications for aqueous alteration. Geochim. Cosmochim. Acta. 57, 2843-2852.

Jull A. J. T., Cheng S., Gooding J. L., and Velbel M. A. (1988) Rapid growth of magnesium-carbonate weathering products in a stony meteorite from Antarctica. Science 242, 417-419.

Kaczaral P. W., Dodd R. T., and Lipschutz M. E. (1989) Chemical studies of L chondrites: IV. Antarctic/non-Antarctic comparisons. Geochim. Cosmochim. Acta 53, 491-501.

Kaneoka, I. (1983) Anomalously old ^{39}Ar-^{40}Ar ages of Antarctic meteorites due to weathering. Nature 304, pp. 146-148.

Karlsson H. R., Socki R. A., Gibson E. K., and Balafas J. S. (1990) Stable isotopic compositions of carbonates in Antarctic ordinary chondrites: Indicators of terrestrial weathering? Papers presented to the 53rd Ann. Mtg. Met. Soc., Perth, 73.

Kelly

Koebe

Laul

Linds

Lipsc

Lipsc

Lipsc

Lipsc

Lipsc

Lipsc

Kelly W. C. and Zumberge J. H. (1960) Weathering of a quartz diorite at marble point, McMurdo Sound, Antarctica. Journal of Geology 69, 433-446.

Koeberl C. and Cassidy W. A. (1991) Differences between Antarctic and non-Antarctic meteorites: An assessment. Geochim. Cosmochim. Acta. 55, 3-18.

Laul J.C. (1986) The Shergotty consortium and SNC meteorites: An overview. Geochim. Cosmochim. Acta. 50, 875-887.

Lindstrom M. M. (1989) Lunar meteorites: Newly discovered moon rocks which have been here all along. Abstract. Geo. Soc. Am. meeting. Vol. 21, No. 6.

Lipschutz M. E. (1980) Weathering effects in Antarctic meteorites. in Catalog of Meteorites from Victoria Land, Antarctica; 1978-1980. (U. B. Marvin and B. Mason eds.). Smithsonian Contributions to the Earth Sciences 24, 67-69.

Lipschutz M. E. (1986) Trace elements in Antarctic meteorites: Weathering and genetic information. In Workshop on Antarctic Meteorites (J. Annexstad et al. eds.); LPI Tech. Rept. 86-01, pp.

Lipschutz M. E. (1990a) Chemical compositional comparison of Antarctic and non-Antarctic meteorite populations. In Workshop on Differences between Antarctic and non-Antarctic Meteorites (C. Koeberl and W. A. Cassidy eds.); LPI Tech. Rept. 90-01, pp. 57-58. Lunar and Planetary Institute, Houston.

Lipschutz M. E. (1990b) Differences between Antarctic and non-Antarctic meteorite populations. In Workshop on Differences between Antarctic and non-Antarctic Meteorites (C. Koeberl and W. A. Cassidy eds.); LPI Tech. Rept. 90-01, pp. 59-60. Lunar and Planetary Institute, Houston.

Lipschutz M. E. and Cassidy W. A. (1986) Antarctic Meteorites: A progress report. Eos 67, 1339-1341.

Lipschutz M. E. and Samuels S. M. (1991) Ordinary chondrites: Multivariate statistical analysis of trace element contents. Geochim. Cosmochim. Acta 55, 19-34.

Lipschutz M. E., Gaffey M. J., and Pellas P. (1989) Meteorite parent bodies: nature, number, size and relation to present-day asteroids. Asteroids II. (eds. R. P. Binzel, T. Gehrels, and M. S. Matthews); The University of Arizona Press, 1258 pp.

Macdougall J. D., Lugmair G. W. and Kerridge J. F. (1984) Early solar system aqueous activity: Sr isotope evidence from the Orgueil CI meteorite. Nature 307 pp. 249-250.

Mackinnon I. D. R. and Zolensky M. E. (1984) Proposed structures for poorly characterized phases in C2M carbonaceous chondrite meteorites. Nature 309 pp. 240-242.

Marvin U. B. (1980) Magnesium carbonate and magnesium sulfate deposits on Antarctic meteorites. Antarct. Jour. U.S. 15, pp. 54-55.

Marvin U. B. and Macpherson eds. (1992) Field and laboratory investigations of Antarctic meteorites collected by United States expeditions, 1985-1987. Smithsonian Contributions to the Earth Sciences, No. 30. Smithsonian Institution Press, Washington D. C.

McSween H. Y. (1979) Alteration in CM carbonaceous chondrites inferred from modal and chemical variations in matrix. Geochim. Cosmochim. Acta 43, pp. 1761-1770.

McSween H. Y. (1979) Are carbonaceous chondrites primitive or processed? A review Rev. Geophys. Space Phys. 17, 1059-1078.

McSween H. Y. (1987) Meteorites and their parent planets. Cambridge University Press, Cambridge, 237 pp.

McSween H. Y. and Weissman X. X. (1989) Cosmochemical implications of the physical processing of cometary nuclei. Geochim. Cosmochim. Acta 53, pp. 3263.

Mittlefehldt D. W. and Lindstrom M. M. (1991) Generation of abnormal trace element abundances in Antarctic eucrites by weathering processes. Geochim. Cosmochim. Acta 55, 77-87.

Miyamo
w
n
r
8

Nishi
C
C
S
T
I

Nishi
T
A
W
A
e
H

Nishi
T
A
A
4

Nishi
C
R

Oberst
B
s
M

Olsen
i
C

Olsen
M

Olsen
m
2

Miyamoto M. (1991) Differences in the degree of weathering between Antarctic and non-Antarctic meteorites inferred from infrared diffuse reflectance spectra. Geochim. Cosmochim. Acta. 55, 89-98.

Nishiizumi K. (1986) Terrestrial and exposure histories of Antarctic meteorites. in International Workshop on Antarctic Meteorites (J. O. Annexstad, L. Schultz, and H. Wanke eds.), Lunar Planet Inst. Tech. Rpt. 86-01, 71-73. Lunar and Planetary Institute, Houston, TX.

Nishiizumi K. (1990) Weathering effects on and terrestrial ages from cosmogenic radionuclides in Antarctic and non-Antarctic meteorites. In Workshop on Differences between Antarctic and non-Antarctic Meteorites (C. Koeberl and W. A. Cassidy eds.); LPI Tech. Rept. 90-01, pp. 72-73. Lunar and Planetary Institute, Houston.

Nishiizumi K., Arnold J. R., Elmore D., Ma X., Newman D., and Gove H. E. (1983) ^{36}Cl and ^{53}Mn in Antarctic meteorites and ^{10}Be-^{36}Cl dating of Antarctic ice. Earth Planet. Sci. Lett. 62, 407-417.

Nishiizumi K., Elmore D., and Kubik P. W. (1989) Update on terrestrial ages of Antarctic meteorites. Earth Planet. Sci. Lett. 93, 299-313.

Oberst J. (1989) Possible relationship between the Farmington meteorite and a seismically detected swarm of meteoroids impacting the Moon. Meteoritics. 24, 1.

Olsen E. and Grossman L. (1978) On the origin of isolated olivine grains in type 2 carbonaceous chondrites. Earth Planet. Sci. Lett. 41, 111-127.

Olsen E. (1981) Vugs in Ordinary Chondrites. Meteoritics. 16, 1.

Olsen E. (1981) Estimates of total quantity of meteorites in the East Antarctic ice cap. Nature. 292, pp. 516-518.

Paul

Paul

Paul

Reid

Samu

Samue

Scho

Schul

Schul

Schul-

Paul R. L. and Lipscutz M. E. (1987) Volatile/mobile trace elements in eucrites--I. Antarctic/non-Antarctic comparisons. Lunar Planet. Sci. XVIII, 768-769.

Paul R. L. and Lipschutz M. E. (1989) Labile trace elements in some Antarctic carbonaceous chondrites: Antarctic and non-Antarctic meteorite comparisons. Z. Naturforsch. 44a, 979-987.

Paul R. L. and Lipschutz M. E. (1990) Chemical studies of diffentiated meteorites: I. Labile trace elements in Antarctic and non-Antarctic eucrites. Geochim. Cosmochim. Acta 54, 3185-3196.

Reid A. M. and Bunch T. E. (1975) The Nakhlites part II: Where, when and how. Meteoritics. 10, 317-323.

Samuels S. M. (1990) Applications of statistic to Antarctic, non-Antarctic differences. In Workshop on Differences between Antarctic and non-Antarctic Meteorites (C. Koeberl and W. A. Cassidy eds.); LPI Tech. Rept. 90-01, pp. 74-80. Lunar and Planetary Institute, Houston.

Samuels S. M. and Lipschutz M. E. (1988) Antarctic and non-Antarctic meteorites: Different populations. Meteoritics 23, 299.

Schott J., Berner R. A. and Sjoberg L (1981) Mechanism of pyroxene and amphibole weathering-1. Experimental studies of iron-free minerals. Geochim. Cosmochim. Acta. 45, 2123-2135.

Schultz L. (1986b) Allende in Antarctica: Temperatures in Antarctic meteorites. Abst. Meteoritics 21, 505.

Schultz L. (1990) Terrestrial ages and weathering of Antarctic meteorites. In Workshop on Antarctic Meteorite Stranding Surfaces (W. A. Cassidy and I. M. Whillins eds.); LPI Tech. Rept. 90-03, pp. 56-59. Lunar and Planetary Institute, Houston.

Schultz L., Weber H. W., and Begemann F. (1991) Noble gases in H-chondrites and potential differences between Antarctic and non-Antarctic meteorites. Geochim. Cosmochim. Acta 55, 59-66.

Sc

Sc

Se

Se

Si

Si

Si

Sm

So

So

Ta

Scott E. R. D. (1984) Pairing of meteorites found in Victoria Land, Antarctica. Mem. Natl. Polar Res., Spec. Issue 35, 102-125.

Scott E. R. D. (1989) Pairing of meteorites from Victoria Land and the Theil Mountains, Antarctica. Smithsonian Contrib. Earth Sci. 28, 103-111.

Sears D. W. G. (1990) A comparison of the induced thermoluminescence properties of Antarctic and non-Antarctic H chondrites. In Workshop on Differences between Antarctic and non-Antarctic Meteorites (C. Koeberl and W. A. Cassidy eds.); LPI Tech Rept. 90-01, pp. 83-85. Lunar and Planetary Institute, Houston.

Sears D. W. G. and Dodd R. T. (1988) Overview and classification of meteorites. In Meteorites and the Early Solar System (J. F. Kerridge and M. S. Matthews eds.); University of Arizona Press. 1269 pp.

Siever R. and Woodford N. (1979) Dissolution kinetics and the weathering of mafic minerals. Geochim. Cosmochim. Acta. 43, 717-724.

Singer A. (1966) The mineralogy of the clay fraction from basaltic soils in the Galilee, Israel. Jour. Soil Science 17, 136-147.

Singer A. (1977) The nature of basalt weathering in Israel. Soil Science. 125, 217-225.

Smith J. (1957) A mineralogical study of weathering and soil formation from olivine basalt in Northern Ireland. Jour. Soil Science 8, 226-239.

Sokolov I. A. and Gradusov B. P. (1978) Soil formation and weathering on basic rocks in a cold humid climate. Pochvovedeniye, 2:5-17, 11-22.

Solberg, T. C. and Burns, R. G. (1988) Iron oxidation state and weathering studies of SNC and other Antarctic meteorites. Abst. Lunar Planet. Sci. Conf. 18th, pp. 936-937.

Takeda H. (1991) Comparisons of Antarctic and non-Antarctic achondrites and possible origin of the differences. Geochim. Cosmochim. Acta 55, 35-47.

Tazak

Tazak

Tomec

Tomec

Tomec

Van S

Velbe

Velbe

Velbe

Tazaki K. (1986) Observation of primitive clay precursors during microcline weathering. Contrib. Mineral Petrol. 92, 86-88.

Tazaki K., Fyfe W. S. and van der Gaast S. J. (1989) Growth of clay minerals in natural and synthetic glasses. Clays and Clay Minerals. 37, 348-354.

Tomeoka K. and Buseck P. R. (1982) Intergrown mica and montmorillonite in the Allende carbonaceous chondrite. Nature. 299, 326-327.

Tomeoka K. and Kojima H. (1990) Yamato-82162 and -86720: New kinds of carbonaceous chondrites: Mineralogical and petrographic comparison. In Workshop on Differences between Antarctic and non-Antarctic Meteorites (C. Koeberl and W. a. Cassidy eds.); LPI Tech. Rept. 90-01, pp. 91-93. Lunar and Planetary Institute, Houston.

Tomeoka K., Kojima H., and Yanai K. (1989b) Yamato-86720: A CM carbonaceous chondrite having experienced extensive aqueous alteration and thermal metamorphism. Proc. NIPR Symp. Antarctic Meteorites 2, 55-74.

Van Schmus W. R. and Wood J. A. (1967) A chemical-petrological classification for the chondritic meteorites. Geochim. Cosmochim. Acta 31, pp. 747-765.

Velbel M. A. (1988) The distribution and significance of evaporitic weathering products on Antarctic meteorites. Meteoritics. 23, 151-159.

Velbel M. A. (1989) Paragenesis and metastability of Mg-carbonates on weathered equilibrated ordinary chondrites from Antarctica. Abst. Eos 70, 15, p. 379.

Velbel M. A. and Gooding J. L. (1990) Terrestrial weathering of Antarctic stony meteorites--Developments 1985-1989. In Workshop on Differences between Antarctic and non-Antarctic Meteorites (C. Koeberl and W. A. Cassidy eds.); LPI Tech. Rept. 90-01 pp. 94-98. Lunar and Planetary Institute, Houston.

Vel

Vel

Was

Whi

Wri

Yat

Yat

Yat

Zo

Zo

Velbel M. A., Long D. T., and Gooding J. L. (1991) Terrestrial weathering of Antarctic stone meteorites: Formation of Mg-carbonates on ordinary chondrites. Geochim. Cosmochim. Acta 55, 67-76.

Velbel M. A. (1993) Formation of protective surface layers during silicate-mineral weathering under well-leached, oxidizing conditions. American Mineralogist 78, 405-414.

Wasson J. (1972) Formation of ordinary chondrites. Review of Geophysics and Space Physics 10, 3, pp. 711-759.

Whillans I. M. and Cassidy W. A. (1983) Catch a falling star: Meteorites from old ice. Science 222, 55-57.

Wright I. P. and Grady M. M. (1989) Antarctic differences of opinion. Nature 341, 691.

Yates A. M. (1988) Two methods for determining weathering in equilibrated chondrites. Meteoritics 23, 313.

Yates A. M. (1989) Weathering in ordinary chondrites as evidenced by chemical analysis (old and new). Meteoritics 24, 343.

Yatsu, Eiju (1988) The nature of weathering: an introduction. SOZOSHA publishers, Tokyo, Japan, 624 pp.

Zolensky M. and McSween, Jr. H. Y. (1988) Aqueous alteration. in Meteorites and the Early Solar System (J. F. Kerridge and M. S. Matthews eds.); University of Arizona Press, pp. 114-143.

Zolensky M., Barrett R., and Browning L. (1993) Mineralogy and composition of matrix and chondrite rims in carbonaceous chondrites. Geochim. Cosmochim. Acta. 57, 3123-3148.

MICHIGAN STATE UNIV. LIBRARIES
31293013992247